Theoretical studies of the optical properties of photonic crystal and microcavity-based structures

IORSH, IVAN

Abstract

The work reported in this thesis is dedicated to the theoretical study of the certain properties of several types of resonant and nonresonant photonic nanostructures.

Negative refraction at the side edge of a Bragg reflector is studied. Analytical theory supported by numerical modelling using finite-difference time-domain (FDTD) simulations shows that the negative refraction in this case is equivalent to -1 order diffraction. Moreover, it is shown that a new effect, spatial oscillation of the Poynting vector of the transmitted radiation, can be observed under certain circumstances. In a separate study the design of a spectral filter for the terahertz frequency range based on a metallic photonic crystal prism has been developed and refined. The theory makes use of the complex band structure method together with FDTD simulations and shows that large angle separation of certain frequency component can be achieved with a prism due to the negative refraction effect. Experimental measurements on a device fabricated with a proposed design are also presented and confirm the theoretical predictions.

An optical eigenmode analysis of two organic microcavities separated by a thin metal layer has been carried out, both numerically and analytically. The analytical theory shows that the sharp reflections features observed in experimental reflectivity measurements are caused by the strong coupling of the Tamm plasmon modes present on both sides of the metal film.

Analytical theory is developed explaining the experimentally measured reflectivity spectra of a one-dimensional photonic crystal with quantum wells embedded in its layers. The dispersion properties of the eigenmodes of the structure, originating from the strong coupling of quantum well excitons and photonic crystal modes are calculated. It is shown, that a new type of exciton-polariton, defined by the negative group velocity and effective mass can be observed in the structures.

A theoretical formalism and corresponding software code have been developed to model the kinetics of polariton lasers. The model is based on a Boltzmann equation approach and accounts for electrical or optical pumping, polariton decay, and polariton-acoustic phonon, polariton-free electron and polariton-polariton scattering. The software code has been used to model the main characteristics of the specific GaN-based polariton lasers using parameters provided by experimental collaborators. It is predicted that the design of electrically driven polariton laser considered would have a threshold current density of 50 Acm^{-2} at room temperature.

DURHAM UNIVERSITY

Theoretical studies of the optical properties of photonic crystal and microcavity-based structures

by

Ivan Iorsh

A thesis submitted in partial fulfillment for the degree of Doctor of Philosophy

in the

Centre of Material Physics

Department of Physics

May 2013

Table of contents

List of Figures

List of Tables

Declaration of Authorship

I, Ivan Iorsh, declare that this thesis titled, 'Theoretical studies of the optical properties of photonic crystal and microcavity-based structures' and the work presented in it are my own. I confirm that:

- This work was done wholly or mainly while in candidature for a research degree at this University.
- Where any part of this thesis has previously been submitted for a degree or any other qualification at this University or any other institution, this has been clearly stated.
- Where I have consulted the published work of others, this is always clearly attributed.
- Where I have quoted from the work of others, the source is always given. With the exception of such quotations, this thesis is entirely my own work.
- I have acknowledged all main sources of help.
- Where the thesis is based on work done by myself jointly with others, I have made clear exactly what was done by others and what I have contributed myself.

Signed: _____

Date: _____

Statement of Copyright

List of Publications

1. I.V. Iorsh, M.A. Kaliteevski, S. Brand, R.A. Abram, N.A. Kaliteevskaya. An electromagnetic wiggler originating from refraction of waves at the side edge of a Bragg reflector. Journal of Modern Optics 58, 8, 683-693 (2011).

2. G. P. Swift, A. J. Gallant, N. Kaliteevskaya, M. A. Kaliteevski, S. Brand, D. Dai, A. J. Baragwanath, I. Iorsh, R. A. Abram, and J. M. Chamberlain. Negative refraction and the spectral filtering of terahertz radiation by a photonic crystal prism, Optics Letters 36, 9, 1641-1643 (2011).

3. A. Askitopoulos, L. Mouchliadis, I. Iorsh, G. Christmann, J.J. Baumberg, M.A. Kaliteevski, J. Hatzopoulos, P.G. Savvidis. Bragg polaritons: strong coupling and amplification in an unfolded microcavity, Physical Review Letters 18, 107, 076401 (2011).

4. R. Bruckner, M. Sudzius, S. I. Hintschich, H. Frob, V. G. Lyssenko, M. A. Kaliteevski, I. Iorsh, R. A. Abram, A. V. Kavokin, and K. Leo. Parabolic polarization splitting of Tamm states in a metal-organic microcavity, Applied Physics Letters, 100, 062101 (2012).

5. I. Iorsh, M. Glauser, G. Rossbach, J. Levrat, M. Cobet, R. Butté, N. Grandjean, M. A. Kaliteevski, R. A. Abram, and A. V. Kavokin. Generic picture of the emission properties of III-nitride polariton laser diodes: Steady state and current modulation response, Physical Review B, 86, 125308 (2012).

Acknowledgements

I would like to express my deepest appreciation to my supervisors, Professor Richard Abram and Doctor Stuart Brand. Without their persistent guidance and help this dissertation would not have been possible.

I would like to thank Professor Alexey Kavokin, who is a coordinator of Clermont4 project, which provided financial support of my research.

In addition it gives me pleasure in acknowledging the support of Professor Mikhail Kaliteevski, who continually and convincingly conveyed a spirit of adventure in regard to research and scholarship.

I share a credit of my work with our collaborators from University of Dresden, Cambridge University, University of Crete, and École Politechnique Fédérale de Lausanne.

Finally, I am indebted to my wife, my parents, and friends for their help and encouragement.

Chapter 1

Introduction

A key trend in information technology over the last fifty years has been miniaturisation. The characteristic size of devices has been decreasing constantly as recognized by the famous empirical Moore's law, which states that the number of transistors on integrated circuits doubles approximately every two years, and which has been valid with only minor variations for the last forty years. However, it is quite evident, that the characteristic sizes of the elements of conventional electronic integrated circuits have almost reached their physical limit, and that further reduction is precluded not by fabrication technology but rather by fundamental physical limitations. In order to continue the speed of growth of computational power of modern computers, new concepts of the computation must be employed. Such concepts include quantum computers, biological computers and, most relevant to this thesis, optical information processing. For the physicist, the main challenge posed by this trend is how best to describe systems and model devices operating at the boundary of classical and quantum domains. It is in this context that this thesis addresses some topical problems in optical structures and devices that are concerned with the control of light and light-matter interaction.

We begin by describing in rather general terms some concepts in the electromagnetic theory of optical structures and in the physics of the light-matter interaction that are relevant to the research reported in the thesis. We also give a very brief introduction to the research problems that have been addressed and describe how the thesis is structured. A more detailed introduction to each research topic is given in the appropriate chapter.

Electromagnetic radiation obeys Maxwell equations:

$$\begin{aligned} \nabla \cdot \mathbf{D} &= 4\pi\rho, \\ \nabla \cdot \mathbf{B} &= 0, \\ \nabla \times \mathbf{E} &= -\frac{1}{c}\frac{\partial \mathbf{B}}{\partial t}, \\ \nabla \times \mathbf{H} &= \frac{1}{c}\frac{\partial \mathbf{D}}{\partial t} + \frac{4\pi}{c}\mathbf{J}, \end{aligned} \tag{1.1}$$

where respectively $\mathbf{E}$ and $\mathbf{H}$ are the electric and magnetic fields; $\mathbf{D}$ and $\mathbf{B}$ are the electric displacement field and magnetic inductance; ρ and $\mathbf{J}$ are the charge and current densities, and c is the speed of light.

There are no external charges or currents in the optical structures considered in the thesis and it is assumed that the structures do not have any magnetic response. Consequently, Maxwell equations can be reduced to

$$\nabla \times \nabla \times \mathbf{E} = -\frac{1}{c^2}\frac{\partial^2 \mathbf{D}}{\partial t^2}, \tag{1.2}$$

which governs the optical properties of all the structures considered in the thesis. However, depending on the behaviour of $\mathbf{D}$, two general types of structure can be distinguished in the work reported. In one type of structure the electric displacement is defined only by a spatially-varying, frequency-independent dielectric permittivity through the relation $\mathbf{D}(\mathbf{r}, t) = \varepsilon(\mathbf{r})\mathbf{E}(\mathbf{r}, t)$. In this case we can look for solutions in the form $E \sim e^{-i\omega t}$ and equation (1.2) can be written as

$$\nabla \times \nabla \times \mathbf{E}(\mathbf{r}) = \frac{\omega^2}{c^2}\varepsilon(\mathbf{r})\mathbf{E}(\mathbf{r}). \tag{1.3}$$

The solutions of this equation obey a simple scaling law: if we decrease all the dimensions of the system by a factor of α then to get the same distribution of the fields we must increase the frequency ω by a factor of α.

The idea that periodic modulation of the dielectric permittivity can determine certain optical properties of a structure was recognized by Bragg [1] when he explained the resonant peaks in the X-ray reflection spectra of crystalline solids. In this work Bragg modelled the crystal as a set of parallel planes separated by a distance d and explained the reflection peaks by the constructive interference of X-rays reflected from those planes. The condition for constructive interference is the well known Bragg's law

$$n\lambda = 2d\sin\theta, \tag{1.4}$$

where λ is the wavelength, θ is the incidence angle and n is an integer. In such Bragg diffraction, the X-ray wavelength λ is comparable with the crystal interplane distance d.

The scaling of Maxwell's equations discussed earlier suggests that in order to obtain Bragg diffraction in the optical and infra-red frequency range, the period of the structure should be of the order of 100 nm. Although such structures have been studied in one form or another since 1887 [2], the term *photonic crystal* was only used for the first time some 100 years later, when Eli Yablonovitch and Sajeev John published two milestone papers on periodic dielectric structures in 1987 [3, 4]. The long delay between the initial work and the advent of the rapid emergence of the new field of solid state physics dedicated to photonic crystals can be explained by the fact that the fabrication of a wide range of suitable structures only became possible in the 1980s following substantial progress in semiconductor technology. Moreover, the development of semiconductor optoelectronic devices such as light-emitting diodes (LEDs) and lasers, and a growing interest in integrated optics led to the need for new ways to control light on a microscopic scale, and photonic crystals provided such a possibility. The principal property of photonic crystals is their ability to modify the propagation of light. The propagating modes in photonic crystal can be described in reciprocal space in much the same way as the electronic Bloch states of a semiconductor. The frequency dispersion of the modes can be substantially different from a homogeneous dielectric. Furthermore, there can be frequency gaps in the band structure for which light propagation is not possible. Photonic crystals are now used in a wide range of optoelectronic applications from the anti-reflection coatings for solar-cells to increasing the efficiency LEDs [5].

Chapter 2 of the thesis is dedicated to studies of the scattering of light at the interfaces of one- and two-dimensional photonic crystals. A new effect of Poynting vector beating of the light refracted at the side edge of one-dimensional photonic crystal is presented and also a design for a spectral filter for the terahertz frequency range based on a two-dimensional metallic photonic crystal prism is developed.

In deriving of equation (1.3) and the corresponding scaling laws from equation (1.2) it was assumed that the dielectric permittivity is frequency-independent. However, if we now introduce an additional polarization $\mathbf{P}(\mathbf{r},t)$ for which this assumption does not hold, equation (1.2) becomes

$$\nabla\times\nabla\times\mathbf{E}(\mathbf{r},t)+\frac{\varepsilon(\mathbf{r})}{c^2}\frac{\partial^2\mathbf{E}(\mathbf{r},t)}{\partial t^2}=-\frac{1}{c^2}\frac{\partial^2\mathbf{P}(\mathbf{r},t)}{\partial t^2}. \tag{1.5}$$

It is clear that we cannot solve equation (1.5) without additional information on the

behaviour of the polarization **P**. In the thesis only one special type of additional polarization is considered, namely that of a quantum well exciton. Excitons are Coulomb-correlated electron - hole pairs that can take different forms depending on the properties of the host medium. A broad distinction can be made based on spatial size and binding energy, and here we consider Wannier-Mott excitons, characteristic of the common semiconductors and having relatively large size (several nanometers) and relatively small binding energy (a few tens of meV) [6]. Excitons can be observed experimentally by sharp peaks in the absorption spectrum of the semiconductors close to the fundamental absorption edge. The energy spectrum of excitons in bulk semiconductors is like that of a hydrogen atom with the following renormalization: $m_0 \to \mu$, and $e^2 \to e^2/\varepsilon$, where m_0 is the free electron mass, and μ is the reduced exciton mass. As a result of spatial confinement, excitons in quantum wells, wires and dots have properties rather different from bulk excitons, including qualitatively different energy spectra, larger binding energies and smaller effective localization lengths. The polarization induced by a quantum well exciton can be written in the frequency domain as [7]:

$$\mathbf{P}(\omega, z) = \int_{-\infty}^{\infty} \chi(\omega, z, z')\mathbf{E}(\omega, z')dz'. \tag{1.6}$$

Here z is the direction perpendicular to the quantum well plane, and $\chi(\omega, z, z')$ is the nonlocal susceptibility given by:

$$\chi = \frac{Q}{\omega_0 - \omega - i\gamma}\Phi(z)\Phi(z') \tag{1.7}$$

where Φ is the exciton wavefunction in the case when the electron and hole are at the same position in the well plane, Q is a quantity defined by the material properties of the quantum well, ω_0 is the exciton frequency, and γ is the exciton line broadening. Substitution of the polarization into equation (1.5) shows that the eigenfrequencies of the structures are no longer only defined by the geometry and dimensions of the photonic structures but also by the exciton resonance frequency ω_0, precluding the simple scaling relation described earlier for 'non-resonant' photonic crystals.

Placing the quantum well in the centre of an optical cavity and tuning a cavity resonant mode to the exciton resonant frequency can lead to the formation of a new type of eigenmode, an *exciton-polariton*, which in some circumstances can be considered to be a composite light-matter quasiparticle with bosonic properties [8].

The fabrication of the structures where the exciton-polaritons can be excited is an extremely technologically challenging process, since it requires both very high quality Bragg mirrors, providing long cavity photon lifetimes, and high quality quantum

wells with small exciton broadening. As a result, exciton-polaritons have hitherto been experimentally studied by only a quite limited number of scientific groups, despite their fascinating fundamental properties and possible applications. A particular attraction of exciton-polaritons is their bosonic nature combined with an extremely small effective mass, which makes possible their condensation at relatively high temperatures, and the observation of related phenomena such as superfluidity. A condensate of exciton-polaritons also emits coherent light and there are intensive efforts to develop an electrically pumped 'polariton laser' [9] based on the effect. However there are other potential applications based on the relatively strong nonlinear effects resulting from the strong interactions of the excitonic component which lead to the possibility of new types of photonic devices such as parametric amplifiers [10] and optical integrated circuits [11]. Also as a result of their composite light-matter nature, exciton-polaritons facilitate the efficient control of quantum processes in semiconductor structures with light, including the recently proposed possibility of light-mediated room-temperature superconductivity [12] and quantum information processing [13].

Chapters 3 and 4 of the thesis are dedicated to the study of some optical properties of exciton-polaritons. Chapter 3 considers the eigenmode structure and parametric amplification of exciton-polaritons in a one-dimensional photonic crystal with the quantum wells embedded into its layers. The theory and calculations support the reflectivity measurements and pump-probe experiments on these structures that have been performed by collaborators. Moreover, it is shown that a slight change in the design of the structures can lead to the formation of a new type of exciton-polariton, defined by a negative effective mass and group velocity.

The work reported in chapter 4 was largely motivated by our experimental collaborators at the École Polytechnique Fédérale de Lausanne, who are working on the realization of the first room-temperature electrically-driven polariton laser. Such a laser is expected to have a much lower threshold compared to the current conventional vertical cavity surface emitting laser diodes (VCSELs). Numerical modelling of the kinetics of prototype polariton lasers has been performed and predictions have been made of designs providing the best operational characteristics and of parameters such as such as threshold current density and current modulation frequency.

Currently the study of photonic crystals and exciton-polariton physics is largely driven by the technologists and experimentalists and most of the work reported in the thesis has been done in collaboration with experimental groups. Where appropriate, experimental details have been given in the relevant chapters and further information can be obtained in the references provided. It is hoped, that the close link with experiment will give the theory described in the thesis a good chance to benefit future technology.

Chapter 2

Negative refraction of light at the edges of one and two-dimensional photonic crystals.

This chapter is dedicated to the study of certain aspects of negative refraction at the edge of photonic crystals. It begins with a general review of the negative refraction effect and specifically negative refraction in photonic crystals. The first investigation reported concerns the study of the scattering of light at the side edge of an infinite Bragg reflector and is presented in section 2. A semi-analytical approach based on the method of moments is used to calculate the scattering. It is shown that the results of the semi-analytical model predict two new effects: spatial oscillations of the Poynting vector for the light refracted into the photonic crystal for the case of low-contrast refractive index and normal propagation of the refracted beam for the case of high-contrast refractive index. The results of numerical finite-difference-time-domain (FDTD) modelling which have been performed to verify the semi-analytical model are also presented [1].

The third section of this chapter considers the refraction of terahertz radiation by a prism made from a metallic photonic crystal and has been published in [15]. It has been shown that due to the negative refraction effect, this structure can be used as an effective terahertz low-pass or high-pass filter. The theoretical results based on band structure calculation and (FDTD) modelling have been verified experimentally [2].

[1] The work described in section 2 has been published in [14] in co-authorship with a number of colleagues. My contribution to the publication was in applying an established theory and in obtaining the results from the semi-analytical and numerical modelling.

[2] The work was carried out in collaboration with colleagues working on microfabrication and terahertz technology who made the photonic crystal prisms and performed all the experiments. My contribution to the work was in performing the numerical FDTD modelling in order to obtain the optimal photonic crystal prism design.

2.1 Review of negative refraction.

The systematic study of the optical properties of media with simultaneously negative dielectric permittivity and magnetic permeability was first reported in [16]. In this paper Veselago proposed the term *left-handed medium* for such materials. This is because if we substitute the plane wave solution $\mathbf{E}, \mathbf{H} \sim \exp[i\mathbf{kr} - i\omega t]$ into Maxwell's curl equations, we get:

$$\mathbf{k} \times \mathbf{E} = \mu \frac{\omega}{c} \mathbf{H}, \tag{2.1}$$

$$\mathbf{k} \times \mathbf{H} = -\varepsilon \frac{\omega}{c} \mathbf{E}. \tag{2.2}$$

In the case of positive ε and μ, the vectors $\mathbf{E}, \mathbf{H}$, and $\mathbf{k}$ form a right-handed basis, and a left-handed basis in the case of negative ε and μ. However, Poynting's vector $\mathbf{S} = \mathbf{E} \times \mathbf{H}$ always forms a right-handed basis with the vectors $\mathbf{E}$ and $\mathbf{H}$; the group velocity is always collinear with Poynting's vector and the phase velocity is always collinear with the wavevector. Thus, in the case of isotropic media, the group and phase velocities are oppositely directed if ε and μ are negative. Such media are also usually characterized by a negative refractive index $n = -\sqrt{\varepsilon\mu}$, and as a consequence, with negative phase velocity. It should be noted, however that Maxwell equations do not contain the refractive index *per se*, and thus the right choice of the sign of the refractive index could be subject to some discussion [17]. Pendry [18] presents the following argument in favour of choosing the negative sign: in realistic physical media losses are always present, which means that both the dielectric permittivity and magnetic permeability have finite imaginary parts: $\varepsilon = \varepsilon' + i\varepsilon''$; $\mu = \mu' + i\mu''$. The refractive index in this case is given by: $n = \pm\sqrt{(\varepsilon'\mu' - \varepsilon''\mu'') - i|\varepsilon''\mu' + \varepsilon'\mu''|}$. However, in order to comply with the causality principle, the imaginary part of the refractive index should be positive, and this condition corresponds to the negative sign of the real part of the refractive index. Thus, the presence of losses is a necessary condition for the right choice of the sign of the refractive index [19]. However, we should note that the arguments provided by Pendry are only valid if we define the refractive index as $n^2 = \varepsilon\mu$, and there are several alternative methods of introducing the refractive index, such as utilizing Snell's law $n = \sin\phi_0 / \sin\phi$, where ϕ_0 are ϕ are the angles between the wavevector and the normal to the interface in vacuum and in the medium respectively. We should also be careful substituting negative refractive index into known optical relations, since many of them have been derived within the assumption of a non-magnetic medium [20]. For example, in the well known expression for the Brewster angle, $\tan\phi = n_2/n_1$, the magnetic permeability of both media is set to unity by default.

Frequency dispersion of the dielectric permittivity and magnetic permeability is a necessary condition for a negative refractive index [21]. Indeed, if the dielectric permittivity and magnetic permeability were frequency-independent, the electromagnetic field energy density $W = (\varepsilon E^2 + \mu H^2)/2$ would be negative. However, in the presence of frequency dispersion, W is given by [22]:

$$W = \left(\frac{\partial(\varepsilon\omega)}{\partial\omega} E^2 + \frac{\partial(\mu\omega)}{\partial\omega} H^2 \right) /2, \tag{2.3}$$

and for certain type of frequency dispersion, W can be positive even for negative dielectric permittivity and magnetic permeability. For example, the dielectric permittivity of a metal within the simplified Drude model is given by:

$$\varepsilon = 1 - \frac{\omega_p^2}{\omega^2}, \tag{2.4}$$

where ω_p is the metal plasma frequency, and

$$\frac{\partial(\omega\varepsilon)}{\partial\omega} = 1 + \frac{\omega_p^2}{\omega^2}, \tag{2.5}$$

which is always positive.

The above arguments are based on the presence of both losses and frequency dispersion of the dielectric permittivity and permeability to obtain a negative refractive index. However, we should remember that the Kramers-Kronig relations show that the presence of losses implies frequency dispersion of the permittivity and vice versa.

Media with negative dielectric permittivity and magnetic permeability have been achieved in *metamaterials*. A metamaterial is an ordered array of identical metallic elements, essentially *artificial atoms*. Just as in a conventional material where the dielectric permittivity and magnetic permeability are an averaged electromagnetic response is determined by both the optical properties of the individual atoms and by the geometrical properties of the lattice, ε and μ of a metamaterial are defined by the electromagnetic properties of the individual elements and by their spatial arrangement. A key difference is that in the case of a metamaterial we can engineer the electromagnetic properties of the constitutive elements by changing their internal structure. In particular, the metamaterial where both negative ε and μ were achieved for the first time [23, 24] was a three dimensional cubic lattice of metallic split rings. The electric response of this medium was controlled by tailoring the filling factor of the metal and as a consequence changing the effective plasma frequency [25]. The magnetic response was engineered by using

a resonant LC circuit in each element. In the vicinity of the resonance frequency, the magnetic permeability of the medium was negative.

Negative refraction is the term used to describe the effect when an electromagnetic wave, refracted at the interface between two media is transmitted on the same side of the normal as the incident one and will occur when the refractive indices are of opposite sign. However, a sufficient condition for negative refraction is that the Poynting's vector and wavevector are in opposite directions in one plane of one of the media and negative ε and μ are not essential for negative refraction. In fact, negative refraction has been predicted and observed in a wide variety of systems, including photonic crystals, metamaterials and plasmonic structures [23, 24, 26–29]. It leads to, for example, the possibility of realizing a *superlens*, which could overcome the diffraction limit [30], the possibility of electromagnetic cloaking [31] and the formation of non-diffracting beams [32]. However, negative refraction will only lead to any of the above-mentioned effects if it is present for a wide range of angles of incidence at the relevant frequency.

As noted, negative refraction has been predicted and observed in photonic crystals [33], but there are certain differences between negative refraction in metamaterials and photonic crystals. First of all, photonic crystals are usually strongly anisotropic media, where it is difficult to introduce the concept of effective refractive index. This also means that the vectors of the phase and group velocities are usually not parallel as in the case of isotropic metamaterials. Moreover, even when a photonic crystal can be treated as an isotropic medium (as to a good approximation in the case of a hexagonal photonic crystal for the frequency ranges close to band edges), negative refraction is realized not because of a negative refractive index, and thus a negative phase velocity, but because of a negative group velocity as, for example , in the second band of a two-dimensional photonic crystal. On the other hand, it is clear that the effect of negative group velocity cannot be the result of simple folding of the photonic bands in the first Brillouin zone since negative group velocity could then be observed even in a photonic crystal with an empty elementary cell, i.e. in a homogeneous dielectric or even in vacuum. Thus, negative group velocity and negative refraction require the existence of a photonic band gap. Finally we note that another mechanism for negative refraction is the diffraction of light at a crystal interface.

2.2 Scattering of light at the side-edge of a Bragg reflector.

Experiments demonstrating negative refraction at the side-edge of one-dimensional photonic crystals have been reported in [34] and the concept of a superlens [30] consisting of two photonic crystals has been proposed in [35].

In this section, we provide a detailed theoretical study of negative refraction at the side edge of a one-dimensional photonic crystal and consider whether such structures are capable of providing useful optical effects.

2.2.1 Calculation method

The geometry of the problem under consideration is depicted in Fig. 2.1. A plane wave in vacuum with wavevector of magnitude k_0 is incident at angle ϕ on the side-edge of a photonic crystal.

A good method of calculating the reflected and transmitted electromagnetic waves for this geometry has been presented in [36] and here we just describe the key steps of the approach before applying it to the specific systems of interest.

We consider the TE polarisation case, for which electric field vector is orthogonal to the plane of incidence.

In order to obtain the field distribution of the reflected and refracted waves, we decompose the tangential components of the electric and magnetic fields into series of modes both in vacuum and in the crystal and then apply the continuity conditions at the interface.

Electric and magnetic fields in vacuum

The $y-$component of the electric field in vacuum can be decomposed into the incident plane wave and a series of reflected plane waves:

$$E_y(x,z) = \sum_{p=-\infty}^{p=\infty} \left[\exp(-i\chi_0 x)\delta_{p0} + R_p \exp(i\chi_p x)\right] \exp(iK_p z), \tag{2.6}$$

where $K_0 = k_0 \sin\phi$, $K_p = K_0 + 2\pi p/D$, $\chi_p = \sqrt{k_0^2 - K_p^2}$, the R_p are the amplitudes of the reflected waves, and δ_{p0} is a Kronecker delta. We can obtain the magnetic field

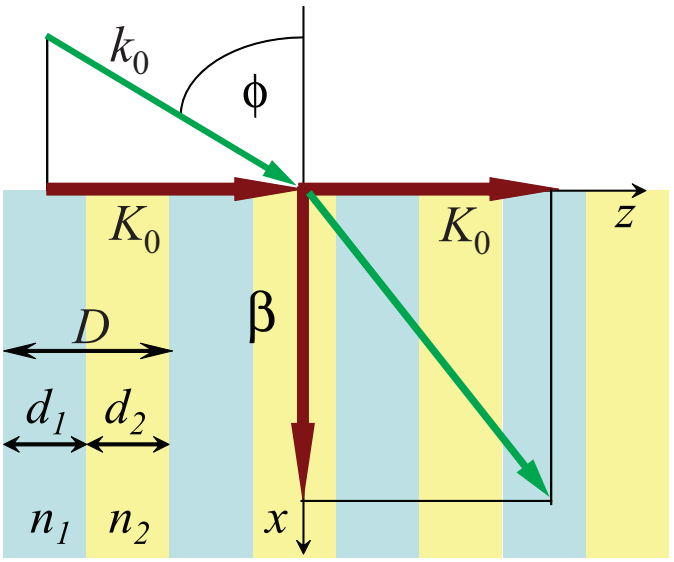

FIG. 2.1: A schematic diagram of the refraction of light at the side edge of a Bragg reflector and the Cartesian coordinate system used in the theory. The structure has alternate layers with thicknesses d_1 and d_2 and respective refractive indices n_1 and n_2. Light is shown incident from vacuum at angle ϕ with wavevector K_0 parallel to the interface. Also shown is a refracted wave with wavevector components K_0 and β, respectively, parallel and normal to the interface.

component $H_z(x,z)$ from the Maxwell equation $\nabla \times \mathbf{E} = -(\partial \mathbf{H}/\partial t)/c = ik_0\mathbf{H}$:

$$H_z(x,z) = \frac{1}{ik_0}\frac{\partial E_y}{\partial x} = \sum_{p=-\infty}^{p=\infty} \frac{\chi_p}{k_0}\left[-\exp(-i\chi_0 x)\delta_{p0} + R_p \exp(i\chi_p x)\right]\exp(iK_p z). \quad (2.7)$$

Electric and magnetic fields in the photonic crystal

The electric field inside the photonic crystal can be written as the series:

$$E_y(x,z) = \sum_m C_m u_m(z)\exp(i\beta_m x), \quad (2.8)$$

where the u_m satisfy the continuity condition at the interfaces of the layers of the photonic crystals and the Bloch theorem: $u_m(z+D) = \exp[iK_0 D]u_m(z)$. Substitution of $E_y(x,z)$ into wave equation shows that the $u_m(z)$ are solutions of the equation

$$\frac{d^2u_m(z)}{dz^2} + k_0^2 n^2(z) = \beta_m^2 u_m(z), \quad (2.9)$$

where $n(z)$ is the refractive index. β_m can then be obtained from the well known dispersion equation for the eigenmodes of a photonic crystal:

$$\cos k_{z1}d_1 \cos k_{z2}d_2 - \frac{1}{2}\left(\frac{k_{z1}}{k_{z2}} + \frac{k_{z2}}{k_{z1}}\right)\sin k_{z1}d_1 \sin k_{z2}d_2 = \cos(K_0 D), \quad (2.10)$$

where $k_{z1} = \sqrt{\varepsilon_1 k_0^2 - \beta^2}$, $k_{z2} = \sqrt{\varepsilon_2 k_0^2 - \beta^2}$. It has been shown that these equation has an infinite number of real solutions β^2, but only a finite number are positive and thus correspond to the propagating solutions (real β [36]). The corresponding u can be written as:

$$u = \frac{\psi(d_1)}{\exp(iK_0D) - \theta(d_1)}\theta(x) + \psi(x), \tag{2.11}$$

where the functions $\theta(z), \psi(z)$ are given by

$$\theta = \begin{cases} \cos(k_{z1}z), 0 \le z \le d_1 \\ \cos(k_{z1}d_1)\cos(k_{z2}(z-d_1)) - \frac{k_{z1}}{k_{z2}}\sin(k_{z1}d_1)\sin(k_{z2}(z-d_1)), d_1 \le z \le D \end{cases} \tag{2.12}$$

$$\psi = \begin{cases} \frac{1}{k_{z1}}\sin(k_{z1}z), 0 \le z \le d_1 \\ \frac{1}{k_{z1}}\sin(k_{z1}d_1)\cos(k_{z2}(z-d_1)) + \frac{1}{k_{z2}}\sin(k_{z1}d_1)\sin(k_{z2}(z-d_1)), d_1 \le z \le D \end{cases} \tag{2.13}$$

Applying the continuity conditions at the interface

The continuity of the electric field at the side edge of the structure ($x = 0$) requires

$$\sum_{p=-\infty}^{p=\infty} [\delta_{p0} + R_p] \exp iK_p z = \sum_m C_m u_m(z). \tag{2.14}$$

Multiplying this equation by u_n^* and integrating over the period of the structure, and using the orthogonality of the u_m we get:

$$C_n = \sum_{p=-\infty}^{p=\infty} [\delta_{p0} + R_p] J_{pn}^*, \tag{2.15}$$

where

$$J_{pn} = \frac{1}{\sqrt{D}} \int_0^D \exp(-iK_p z) u_n(z). \tag{2.16}$$

The proof of the orthogonality of the set u_m is presented in [36] and is based on the fact that the differential operator governing the set u_m is Hermitian. Equation (2.15) can be rewritten in the matrix form:

$$C = \mathrm{J}^H(\mathrm{R} + \mathrm{F}), \tag{2.17}$$

where C = $[C_n]$, J = $[J_{pn}]$, R = $[R_p]$ and F = δ_{p0}, and the superscript H denotes the Hermitian conjugate. The continuity equation for the magnetic field is

$$\sum_{p=-\infty}^{p=\infty} \chi_p \left[-\delta_{p0} + R_p\right] \exp(iK_p z) = \sum_m \beta_m C_m u_m(z). \tag{2.18}$$

Multiplying this equation by $1/\sqrt{D}\exp(-iK_q z)$ and integrating over the period gives:

$$\chi_q[R_q - \delta_{q0}] = \sum_m \beta_m C_m u_m(z) J_{qm}, \tag{2.19}$$

which can be written in matrix notation as

$$\mathrm{R} = \mathrm{F} - \chi^{-1}\mathrm{J}\beta C_m, \tag{2.20}$$

where $\chi = diag[\chi_q]$, $\beta = diag[\beta_m]$. Then substituting R into (2.17),then gives

$$\left(\mathrm{I} + \mathrm{J}^H \chi^{-1} \mathrm{J}\beta\right) \mathrm{C} = 2\mathrm{J}^H \mathrm{F}, \tag{2.21}$$

where I - is the unit matrix. The resulting system of equations can be solved to obtain the amplitudes of the transmitted eigenmodes. The derivation for the TM polarization is carried out in a similar way.

The matrix equation (2.21) is an infinite system of linear equations and a numerical solution can only be obtained by truncating it. To define the number of equations n to be included, we first introduce the sum $s_n = \sum_{i=1}^{n} |C_i|^2$. The C_i set is ordered such that C_1 corresponds to the eigenmode with the largest value of β^2. We assume that s_n converges to a constant value $\tilde{s}$, as $n \to \infty$. The demonstration of the convergence of s_n is shown in Fig.2.2, where it can be seen that as the number of equations n is increased, s_n rapidly approaches some constant value. Assuming the convergence of s_n, it is justified to define the truncation error in the following way: if C_i is the vector of solutions for n eigenmodes, and $\tilde{C}_i$ is the vector for $n+1$ eigenmodes, then the truncation error ε_n can be defined as $\varepsilon_n = \sum_{i=1}^{n+1} |\tilde{C}_i|^2 - \sum_{i=1}^{n} |C_i|^2$. We then define the maximum allowed truncation error, which in our calculations has been set to 10^{-6}. It has been shown that decreasing the maximum truncation error by an order of magnitude changes the results in an essentially negligible way. The number of equations $\tilde{n}$ to be considered was then defined as $\tilde{n} = \min_n(n : \varepsilon_n < 10^{-6})$. The same condition has been applied to the truncation of the reflected amplitudes R.

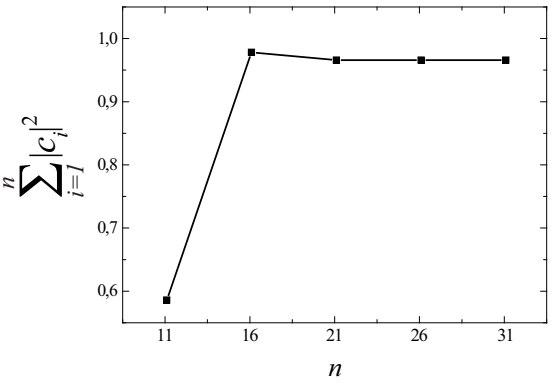

FIG. 2.2: Dependence of the norm of the transmitted amplitudes vector on the number of equations.

In the numerical calculations we have considered quarter-wavelength Bragg reflectors with a stop-band frequency centre tuned to 1 eV. The values of $|C_n|^2$ of some of the eigenmodes for a Bragg reflector with the refractive indices of the layers equal to 1.7 and 1.5 are shown in Fig. 2.3.

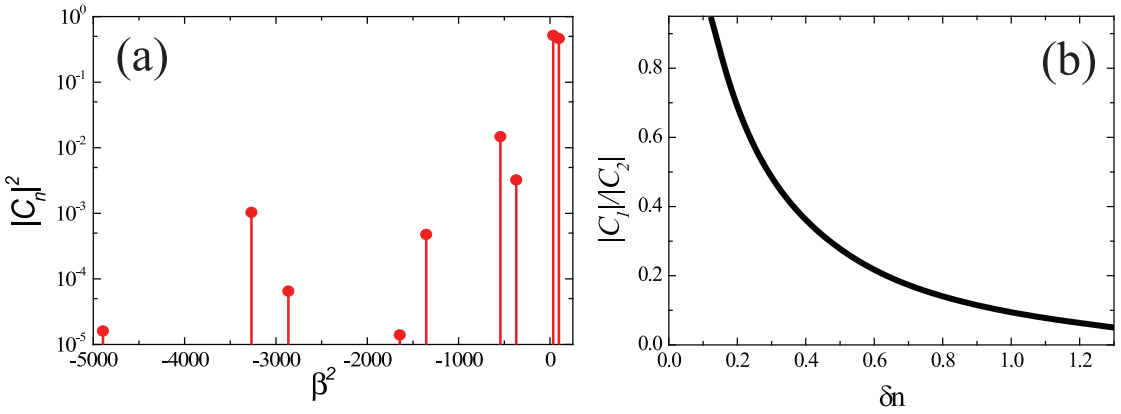

FIG. 2.3: (a) Amplitudes of the eigenmodes for the case of a photonic crystal with refractive indices 1.5 and 1.7. The incident light frequency is 1.5 eV, and the angle of incidence is 60 degrees. (b) C_1/C_2 ratio vs relative contrast of the photonic crystal.

The frequency of the incident light is 1.5 eV which corresponds to the second photonic band of the crystal, and the angle of incidence ϕ is 60 degrees. In Fig.2.3(a) we can see that there are two solutions which correspond to bulk waves propagating inside the crystal ($\beta^2 > 0$) and other solutions corresponding to surface waves, which decay exponentially in the direction normal to the interface ($\beta^2 < 0$). Note that the ratio

$$s = \Big(\sum_{i:\beta_i^2<0} |C_i|^2\Big)/\Big(\sum_{i:\beta_i^2>0} |C_i|^2\Big) \ll 1, \tag{2.22}$$

which means that the contribution of the surface waves to the total energy of the transmitted electromagnetic field is negligibly small. The number of the bulk waves is determined by the number of photonic band N_B, which the frequency of the incident light corresponds to and by the angle of incidence. Depending on the angle of incidence, the number of bulk waves is either exactly equal to the number of photonic bands N_B, or to $N_B - 1$.

It is also considering the dependence of the ratio of amplitudes of the bulk modes on the relative contrast δn of the photonic crystal defined as $|n_1 - n_2|/(n_1 + n_2)$, which is illustrated in Fig. 2.3(b). As the relative contrast is increased, one of the mode coefficients becomes dominant, so most of the energy of the electromagnetic field is transferred to a single eigenmode. We should note, that this property depends on the choice of the basis of the photonic crystal eigenmodes. For example, instead of using the basis u_n discussed above, we could describe the field in a plane wave basis:

$$E(x,z) = \sum_{p=-\infty}^{\infty} C_p' \exp[iK_p z + i\sqrt{k_0^2 - K_p^2}x], \tag{2.23}$$

where $K_p = K_0 + 2\pi p/D$. However, in this case, as the relative contrast of the photonic crystal is increased, the C_p' becomes less convergent, which means that the electromagnetic energy exists in a large number of eigenmodes. In contrast, for the basis u_n most of the electromagnetic energy is transferred into a single eigenmode as the relative refractive index contrast is increased, which facilitates the analytical study of the system. For example, if we include only the zero-order diffraction of the reflected waves, i.e. set $R_{p\neq 0}$ to zero, we can analytically derive an expression for the ratio of bulk mode amplitudes (see Fig.2.3(b)):

$$\frac{|C_1|^2}{|C_2|^2} = \frac{|J_{01}|^2}{|J_{02}|^2}, \tag{2.24}$$

which by the definition of the matrix J is the ratio of the overlap integrals of the incident light and each of the two bulk modes.

To define the direction of propagation of the transmitted light, we calculate the component of the Poynting vector tangential to the Bragg reflector side edge averaged over the crystal period:

$$S_z = -\frac{1}{2D}\int_0^D \mathrm{Re}\left[E_y H_x^*\right] dz = -\frac{1}{2k_0 D}\int_0^D \mathrm{Im}\left[E_y \left(\frac{\partial E_y}{\partial z}\right)^*\right] dz. \tag{2.25}$$

In the case of high refractive index contrast, it is a good approximation to retain only one mode in the series, and using the expression (2.11), we can evaluate the integral

(2.25) analytically to obtain:

$$S_z = \frac{1}{2k_0 D}|C_m|^2 \frac{\sin K_0 D}{k_{z1}\cos k_{z2}d_2 \sin k_{z1}d_1 + k_{z2}\cos k_{z1}d_1 \sin k_{z2}d_2}. \tag{2.26}$$

The z-component of the group velocity and energy flow of the incident light has the same sign as K_0. Therefore if we multiply Eq. (2.26) by K_0, we will get a value that is negative if the $z-$components of the Poynting vectors in the crystal and in the vacuum are antiparallel, which manifests itself physically as negative refraction. In the case of the low contrast photonic crystal we include both bulk modes in the Poynting vector calculation. Then the final expression for the Poynting vector tangential components will contain two terms. corresponding to (2.26) for each of the bulk modes and an additional 'interference' term:

$$-\frac{1}{2k_0 D}\mathrm{Im}\left[\exp(i(\beta_m - \beta_n)x)\int_0^D dz\left(C_m C_n^* u_m \frac{\partial u_n^*}{\partial z} - C_n C_m^* u_n \frac{\partial u_m^*}{\partial z}\right)\right]. \tag{2.27}$$

We note that this additional term contains a factor, which oscillates in the direction perpendicular to the interface.

In order to illustrate the transmission through the photonic crystal interface and the connection between negative refraction and the diffraction of modes, it is instructive to consider the isofrequency contours of the bands of the photonic crystal. We consider waves incident on the photonic crystal with a given frequency but varying angle of incidence and hence tangential wavevector K_0. The transmitted wave must have the same frequency and a tangential wavevector that is either K_0 or differs from it by a reciprocal lattice vector ($2\pi n/D$, where n is an integer). In the example shown in Fig. 2.4 the blue lines correspond to the isofrequency branches, for which the product $S_z K_0$ is negative, and the red lines to the branches for which $S_z K_0$ is positive. The group velocity of each mode is normal to the isofrequency contour and is shown with a green arrow. Since the directions of the group velocities for the points 1 and 2 are parallel, a negatively refracted beam corresponding to arrow 1 is indistinguishable from the -1 diffracted beam shown with arrow 2. The same arguments are valid for the directions 3 and 4. In the case of low contrast (Fig.2.4(a)) the wavevector is almost collinear with the group velocity. However, in the high contrast case (Fig.2.4(b)) the wavevector and group velocity are in markedly different directions, which is a consequence of strong anisotropy of photonic crystal, which increases with increasing relative refractive index contrast. However, even in the case of high contrast regime, the diffracted beams 2 and 4 are indistinguishable from the refracted beams 1 and 3, since their group velocities are parallel. Physically this means, that there is no way to distinguish the negatively refracted beam from the diffracted one.

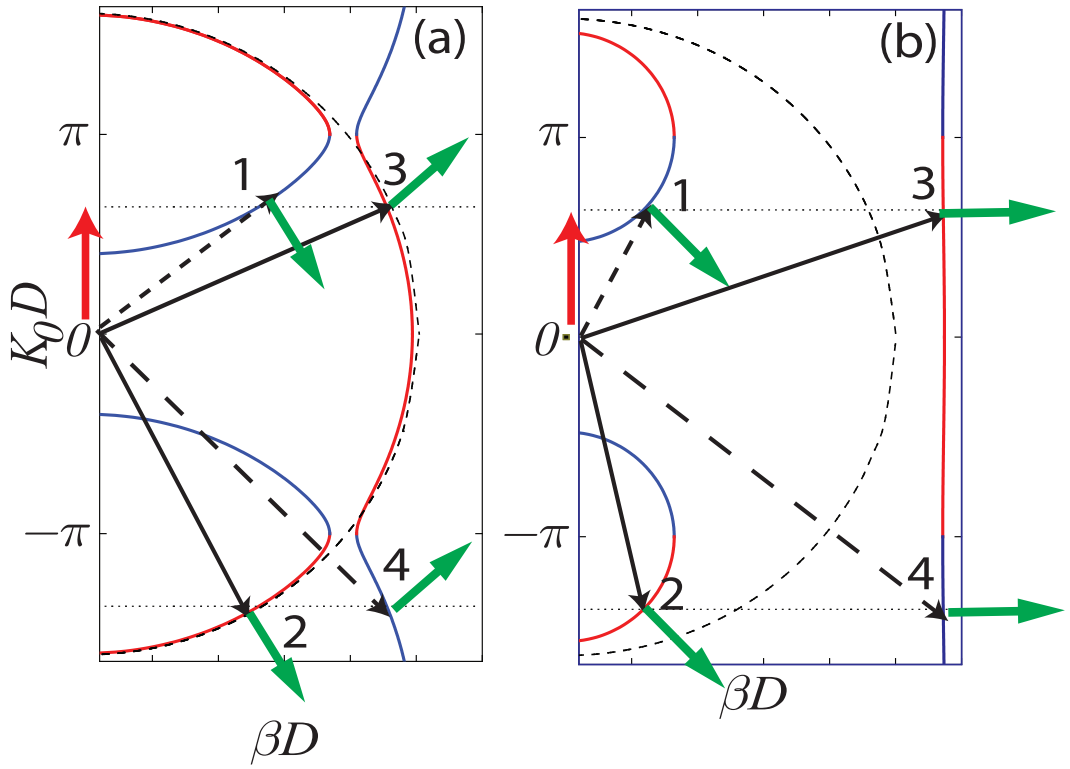

FIG. 2.4: (a) Isofrequency contours for the photonic crystal with refractive indices 1.5 and 1.7 for a frequency of 1.6 eV. Branches which correspond to negative values of $S_z K_0$ are depicted by blue lines and to positive values by red lines. Dashed arrows show the directions of the negatively refracted modes, and solid arrows the directions of the diffracted modes. (b) Isofrequency contours for the photonic crystal with refractive indices 1.1 and 2.1 at a frequency 1.6 eV. In each case isofrequency contours for isotropic media with the effective refractive indices of the photonic crystal are depicted by dashed semicircles. The direction and absolute of the tangential component of the wavevector for the incident wave is shown with red arrow for all the cases. The directions of group velocity and energy flow are shown with green arrows for all the cases. For all the cases the dotted lines show the value of the in-plane component of the incident wave (upper line) and the value of the in-plane wavevector of the diffracted wave (lower line).

It is interesting to consider whether superlensing could be realized in a suitable structure. The electromagnetic field produced by a point source placed close to the edge of the structure can be represented as an integral of plane waves with components of wavevector parallel to the edge of the structure varying continuously from minus infinity to plus infinity. Each of these plane wave components will be refracted by the structure in a distinct way. If we consider the isofrequency contours shown in Figs.2.4(a),(b) we can see that there is always a range of incident tangential wavevectors K_0 for which negative refraction will not occur. As a result, some of the radiation from a point source will always be refracted positively and only some will be refracted negatively, which means that effective subwavelength imaging can not be achieved.

2.2.2 Comparison of the analytical theory and numerical modelling results

The analytical theory and associated results presented in the previous subsection have been verified by numerical modelling using the finite difference-time-domain-technique (FDTD). Figures 2.5(a) and 2.5(b) show the distribution of the square of electric field for waves scattered at the interface of the high contrast photonic crystal ($n_1 = 2.1, n_2 = 1.1$). Figure 2.5(a) shows negative refraction with the frequency of the incident wave lying in the second photonic band of the photonic crystal. Figure 2.5(b) corresponds to the case when $\sin(K_0 D) = 0$, resulting in the tangential component of the Poynting vector being equal to zero and the propagation of the wave being normal to the interface.

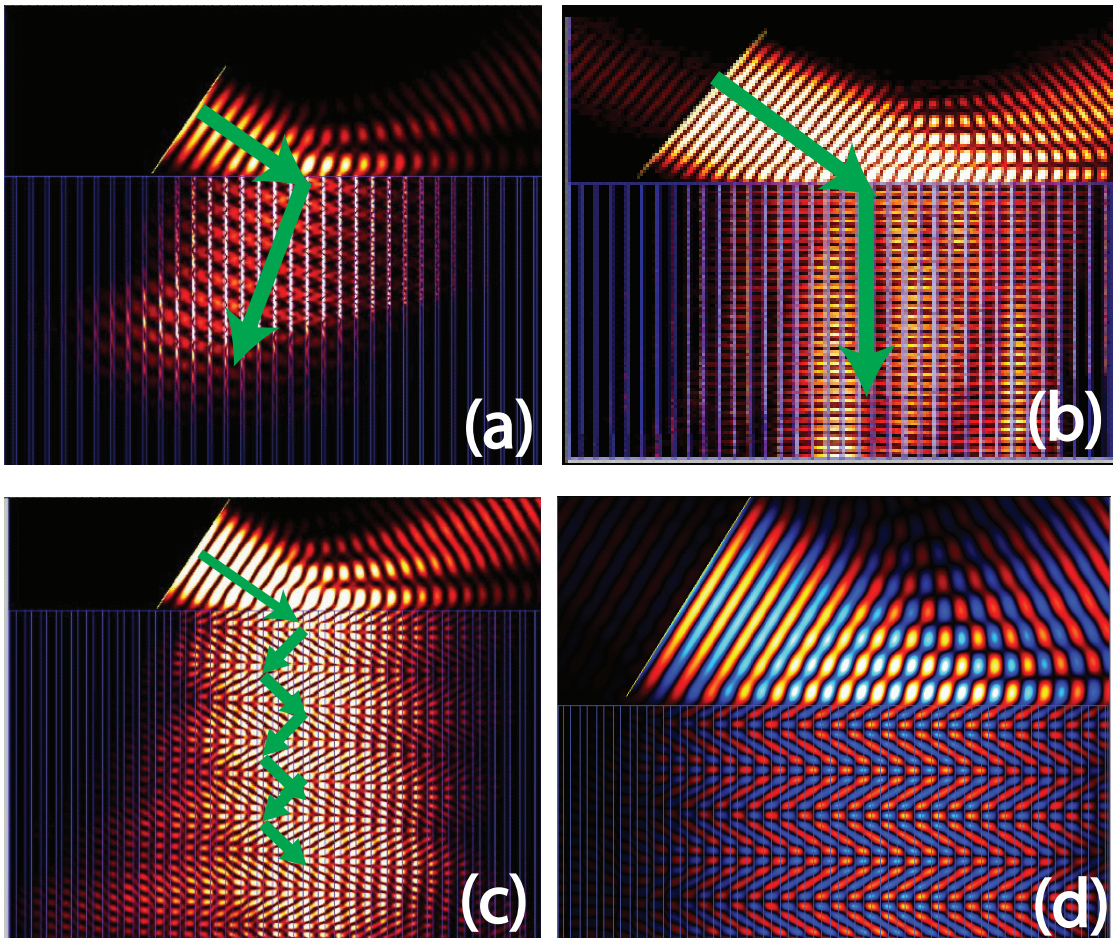

FIG. 2.5: FDTD simulation results for waves scattered at the interface of high ($n_1 = 2.1, n_2 = 1.1$) (a,b) and low ($n_1 = 1.4, n_2 = 1.8$) (c,d) contrast photonic crystal. (a) - Spatial distribution of the square of electric field for the case of negative refraction ($\hbar\omega = 1.6$eV, angle of incidence $\phi = 55$ degrees);(b) Spatial distribution of the square of electric field for the case of normal propagation ($\hbar\omega = 2.0$ eV, $\phi = 55$ degrees); (c) Spatial distribution of the absolute value of the square of electric field for the case of spatial oscillations of the Poynting vector ($\hbar\omega = 2.0$ eV, $\phi = 55$ degrees); (d) Spatial distribution of the real part of the electric field for the case described in (c).

Figure 2.5(c) shows the spatial distribution of the square of the electric field in a low contrast photonic crystal($n_1 = 1.8, n_2 = 1.4$), when the frequency is again chosen to make $\sin(K_0 D) = 0$. In this case, in the analytical expression for the tangential component of the Poynting vector, only the oscillating term in Eq. (2.27) is non-zero. As predicted by the analytical theory, the numerical results show spatial oscillations of the electromagnetic field in the direction normal to the interface. Figure 2.5(d) shows the distribution of the real part of electric field for the same case as in Fig. 2.5(c). For the low contrast photonic crystal, in the case when $\sin(K_0 D) \neq 0$, which is not shown here, we observe a splitting of the incident beam into positively and negatively refracted beams as also predicted by the analytical theory.

2.2.3 Results and conclusions

It should be noted that the analytical model presented assumes an incident plane-wave with an infinite wave front. In an experiment, however, we would be using a light beam of finite size. The numerical calculations show that there exists a critical source size above which the refraction of wave at the interface can be described by the analytical theory. We have derived an estimate of the critical source diameter which is given by $d_{thr} \approx D/\delta n$, where δn is the relative contrast of the photonic crystal. That formula is similar to the expression obtained in [37], which defines the minimum size of the Bragg reflector for the formation of a photonic stop-band suggesting that the origin of the critical source size is the existence of a minimum photonic crystal size for the formation of the photonic band structure. When the source size is significantly less than the critical value, the refraction of the wave at the side edge of the photonic crystal is determined by the effective refractive index $n_{eff} = (n_1 d_1 + n_2 d_2)/(n_1 + n_2)$.

The propagation of the refracted beam normal to the interface can be considered to be the result of an excitation of an array of coupled waveguide modes, where the high refractive index layers play the role of the waveguide core and coupling is achieved via evanescent waves inside the lower refractive index layers that play the role of a waveguide cladding. However, the case of normal propagation is not entirely equivalent to the excitation of waveguide modes since in general it can occur even in the case when the light propagates in both the high and low refractive index layers.

The spatial oscillations of the Poynting vector resemble the Bloch oscillations which have been predicted and observed both in superlattices, for electrons in an external electric field, and for the electromagnetic field in wedge-shaped photonic crystals[38]. In the latter case the gradient of the photonic crystal slab leads to a gradient of the quantized lateral photon momentum which can be considered as an effective potential

or force acting on the photon propagating in the structure. Bloch oscillations occurs when an electron (or photon) propagates in a periodic potential with an external force applied. The wavevector of the particle is changed by an external force, and when it reaches the edge of the Brillouin zone, it changes its wavevector by $\pm 2\pi/D$, where D is the period of the structure. The main difference of the oscillations in our case is the that the oscillations take place in the absence of an external field. However, the wavevector lies exactly at the edge of the Brilloin zone since the condition $\sin(K_0 D) = 0$ applies. Also, the oscillations are only observed in the case of a quarter wavelength Bragg reflector, for which the second band gap of the photonic crystal becomes degenerate. The observed effect of the Poynting vector oscillations can thus be regarded as a result of the interference of two degenerate Bloch modes existing at a photonic crystal band edge.

To conclude, in this section we have developed a theoretical model, which facilitates the description of refraction of electromagnetic wave at the side edge of a one-dimensional photonic crystal. Using the model we have predicted and verified two new effects: normal propagation of the electromagnetic wave and spatial oscillations of the Poynting vector inside the photonic crystal.

2.3 Negative refraction of THz radiation by a prism made of a two-dimensional metallic photonic crystal

In the last few years, terahertz (THz) technology [39] has been applied to a large variety of areas including art conservation [40], medicine [41] and security systems. As a consequence, the demand for new waveguides, filters and other components for the terahertz frequency range has emerged. In this section, the concept of a new filter for the terahertz range is presented. The filter is a prism made from a two-dimensional hexagonal metallic photonic crystal and operates on the basis of obtaining both positive and negative refraction, which can lead to a large directional dispersion for incident light of different frequencies.

2.3.1 Calculational method

We consider a two-dimensional hexagonal photonic crystal formed by a periodic array of metallic nanorods. To calculate the eigenmodes and band structure of such a photonic crystal, we cannot use the conventional plane-wave band structure method since the dielectric permittivity of the metal depends on frequency. However a complex band structure method [42] provides a suitable approach. The method has poor convergence at frequencies close to the metal plasma frequency, but here we use it for the terahertz frequency range, which is three orders of magnitudes less then the plasma frequencies of the noble metals.

We consider the metallic rods to be aligned parallel to the z-axis and begin by studying the TM modes for which the electric field is parallel to the rods. The wave equation for the electric field is then

$$\nabla^2 E_z(\mathbf{r}) = \frac{\omega^2}{c^2}\varepsilon(\mathbf{r})E_z(\mathbf{r}), \tag{2.28}$$

where $\mathbf{r} = (x, y)$. The electric field can be written as the series:

$$E_z(\mathbf{r}) = \sum_{\mathbf{g}} E_{\mathbf{g}} e^{i(\mathbf{k}+\mathbf{g})\cdot\mathbf{r}}, \tag{2.29}$$

which substituted into Eq. 2.28 gives:

$$\sum_{\mathbf{g}} E_{\mathbf{g}}(\mathbf{k}+\mathbf{g})^2 e^{i(\mathbf{k}+\mathbf{g})\cdot\mathbf{r}} = \frac{\omega^2}{c^2}\varepsilon(\mathbf{r})\sum_{\mathbf{g}} E_{\mathbf{g}} e^{i(\mathbf{k}+\mathbf{g})\cdot\mathbf{r}}. \tag{2.30}$$

The spatially-dependent dielectric permittivity $\varepsilon(\mathbf{r})$ of the structure can be written as

$$\varepsilon(\mathbf{r}) = \varepsilon_b + [\varepsilon(\omega) - \varepsilon_b]\, S(\mathbf{r}), \tag{2.31}$$

where ε_b is the background dielectric permittivity, $\varepsilon(\omega)$ is the permittivity of the metal, and $S(\mathbf{r})$ is equal to unity inside the metallic elements and zero outside. We can write $S(\mathbf{r})$ as a series: $S(\mathbf{r}) = \sum_{\mathbf{g}'} S_{\mathbf{g}'} e^{i(\mathbf{k}+\mathbf{g}')\cdot\mathbf{r}}$ and if we substitute this expression into 2.30, we get

$$\sum_{\mathbf{g}} E_{\mathbf{g}} \left[(\mathbf{k}+\mathbf{g})^2 - \frac{\omega^2 \varepsilon_b}{c^2} \right] e^{i(\mathbf{k}+\mathbf{g})\cdot\mathbf{r}} = \frac{\omega^2(\varepsilon(\omega)-\varepsilon_b)}{c^2} \sum_{\mathbf{g},\mathbf{g}'} E_{\mathbf{g}} S_{\mathbf{g}'} e^{i(\mathbf{k}+\mathbf{g}+\mathbf{g}')\cdot\mathbf{r}}. \tag{2.32}$$

Multiplying this by $e^{-i(\mathbf{k}+\mathbf{g})\cdot\mathbf{r}}$, where $\mathbf{g}$ is a reciprocal lattice vector, and integrating over the photonic crystal unit cell gives

$$E_{\mathbf{g}} \left[(\mathbf{k}+\mathbf{g})^2 - \frac{\omega^2 \varepsilon_b}{c^2} \right] = \frac{\omega^2(\varepsilon(\omega)-\varepsilon_b)}{c^2} \sum_{\mathbf{g}} S_{\mathbf{g}-\mathbf{g}} E_{\mathbf{g}}. \tag{2.33}$$

Writing the wavevector $\mathbf{k}$ as $k\hat{\mathbf{u}}$, where $\hat{\mathbf{u}}$ is a unit vector that defines the direction of $\mathbf{k}$, equation (2.33) can be rewritten as

$$k^2 \mathrm{I}\mathbf{E} + k\mathrm{A}\mathbf{E} = (\mathrm{C} - \mathrm{B})\mathbf{E} = \mathrm{D}\mathbf{E}, \tag{2.34}$$

where I is the identity matrix, A is a diagonal matrix with elements: $\mathrm{A}_{\mathbf{g},\mathbf{g}} = 2\mathbf{g}\hat{u}$, C is a matrix with elements $\mathrm{C}_{\mathbf{g},\mathbf{g}} == (\omega^2(\varepsilon(\omega)-\varepsilon_b))/c^2 S_{\mathbf{g}-\mathbf{g}}$, and B is a diagonal matrix with elements: $\mathrm{B}_{\mathbf{g},\mathbf{g}} = g^2 - \omega^2\varepsilon_b/c^2$. Equation 2.34 can be reformulated as the eigenvalue problem

$$\begin{bmatrix} 0 & \mathrm{I} \\ \mathrm{D} & -\mathrm{A} \end{bmatrix} \begin{pmatrix} \mathbf{E} \\ k\mathbf{E} \end{pmatrix} = k \begin{pmatrix} \mathbf{E} \\ k\mathbf{E} \end{pmatrix}, \tag{2.35}$$

from which, after choosing the frequency ω and direction $\hat{\mathbf{u}}$, we can calculate k, which is generally complex. Real k corresponds to propagating solutions, and complex k to decaying solutions.

In the case of the TE polarisation for which the magnetic field is parallel to the rods, the wave equation is

$$\nabla \times \left[\frac{1}{\varepsilon(\mathbf{r})} \nabla \times \mathbf{H}(\mathbf{r},t) \right] = \frac{\omega^2}{c^2} \mathbf{H}(\mathbf{r},t), \tag{2.36}$$

and the inverse dielectric permittivity can be written as:

$$\frac{1}{\varepsilon(\mathbf{r})} = \frac{1}{\varepsilon_b}\left(1 - \frac{\varepsilon(\omega)-\varepsilon_b}{\varepsilon(\omega)} S(\mathbf{r})\right). \tag{2.37}$$

If we then substitute (2.37) into (2.36) and take the Fourier transform of $S(\mathbf{r})$, we get

$$\sum_{\mathbf{g}} H_{\mathbf{g}}(\mathbf{k}+\mathbf{g})^2 e^{i(\mathbf{k}+\mathbf{g})\cdot\mathbf{r}} - \frac{\varepsilon(\omega)-\varepsilon_b}{\varepsilon(\omega)} \sum_{\mathbf{g},\mathbf{g}'} S_{\mathbf{g},\mathbf{g}'} H_{\mathbf{g}}(\mathbf{k}+\mathbf{g}+\mathbf{g}') e^{i(\mathbf{k}+\mathbf{g}+\mathbf{g}')\cdot\mathbf{r}} = \tag{2.38}$$
$$= \frac{\omega^2 \varepsilon_b}{c^2} \sum_{\mathbf{g}} H_{\mathbf{g}} S_{\mathbf{g}} e^{i(\mathbf{k}+\mathbf{g})\cdot\mathbf{r}}.$$

Multiplying (2.38) by $e^{-(\mathbf{k}+\mathbf{g})\cdot\mathbf{r}}$ and integrating over the unit cell gives:

$$H_{\mathbf{g}}(\mathbf{k}+\mathbf{g})^2 - \frac{\omega^2\varepsilon_b}{c^2} H_{\mathbf{g}} = \frac{\varepsilon(\omega)-\varepsilon_b}{\varepsilon(\omega)} \sum_{\mathbf{g}} S_{\mathbf{g}-\mathbf{g}} H_{\mathbf{g}}(\mathbf{k}+\mathbf{g})(\mathbf{k}+\mathbf{g}.), \tag{2.39}$$

which can be rewritten as

$$\mathbf{k}^2(\mathrm{I}-\mathrm{P})\mathbf{H} + \mathbf{k}(\mathrm{A}-\mathrm{Q})\mathbf{H} = (\mathrm{R}-\mathrm{B})\mathbf{H}, \tag{2.40}$$

where the matrices $\mathrm{A}, \mathrm{B}, \mathrm{I}$ are defined in the same way as in the TE case, and matrices P, Q, and R are given by

$$P_{\mathbf{g},\mathbf{g}} = \frac{\varepsilon(\omega)-\varepsilon_b}{\varepsilon(\omega)} S_{\mathbf{g}-\mathbf{g}}, \tag{2.41}$$

$$Q_{\mathbf{g},\mathbf{g}} = \frac{\varepsilon(\omega)-\varepsilon_b}{\varepsilon(\omega)} S_{\mathbf{g}-\mathbf{g}} \hat{\vec{u}}(\mathbf{g}+\mathbf{g}), \tag{2.42}$$

$$R_{\mathbf{g},\mathbf{g}} = \frac{\varepsilon(\omega)-\varepsilon_b}{\varepsilon(\omega)} S_{\mathbf{g}-\mathbf{g}} \mathbf{g}\mathbf{g}. \tag{2.43}$$

Multiplying (2.40) by $(\mathrm{I}-\mathrm{P})^{-1}$, gives

$$\mathbf{k}^2 \mathrm{I}\mathbf{H} + \mathbf{k}\mathrm{A}'\mathbf{H} = \mathrm{D}'\mathbf{H}, \tag{2.44}$$

where $\mathrm{A}' = (\mathrm{I}-\mathrm{P})^{-1}(\mathrm{A}-\mathrm{Q})$ and $\mathrm{D}' = (\mathrm{I}-\mathrm{P})^{-1}(\mathrm{R}-\mathrm{B})$. Equation (2.44) has the same structure as (2.34), and can also be rewritten as a similar eigenvalue equation:

$$\begin{bmatrix} 0 & \mathrm{I} \\ \mathrm{D}' & -\mathrm{A}' \end{bmatrix} \begin{pmatrix} \mathbf{H} \\ k\mathbf{H} \end{pmatrix} = k \begin{pmatrix} \mathbf{H} \\ k\mathbf{H} \end{pmatrix}. \tag{2.45}$$

The theory presented above has been used to calculate the band structure of a hexagonal photonic crystal with a unit cell consisting of a gold cylinder with radius equal to 80 μm and a period of 200 μm. The structure of the first two photonic bands of the

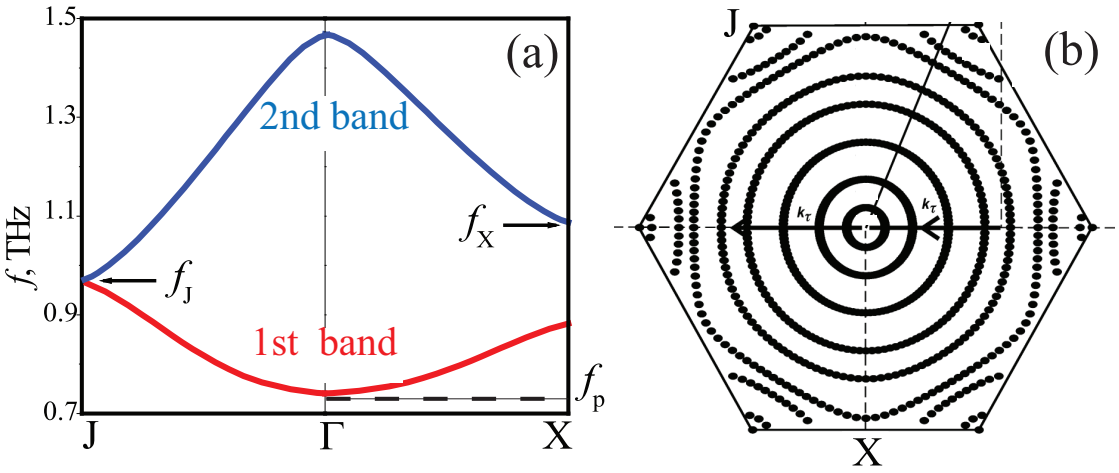

FIG. 2.6: (a) Band diagram of a hexagonal photonic crystal formed by gold cylindrical rods with diameter 80 μm. Period of the structure is 200μm. f_p is an effective plasma frequency, which is a cut-off frequency for the propagating solutions. The group velocity is collinear with the wavevector in the first band (red), which corresponds to positive refraction. The second band (blue), where the group velocity has opposite direction to the wavevector is the source of negative refraction. (b) Isofrequency contours for the frequencies close to high frequency edge of the second band.

crystal is shown in Fig.2.6(a). The cut-off frequency f_p, below which no propagating solutions exist, is equal to 0.76 THz and corresponds to the effective plasma frequency of the photonic crystal. The first photonic band is characterized by a positive group velocity and its upper bound is equal to $f_J = 0.96$ THz. The second photonic band, lying in the frequency range from f_J to 1.45 THz, is characterized by a negative group velocity. The isofrequency contours near the top of the second band are shown inS Fig.2.6(b). They are essentially circular over a wide frequency range, which means an effective dielectric permittivity ε can be introduced. The refractive index is then defined as $n_{eff} = (d\omega/dk)\sqrt{\varepsilon}$, where ε is the effective dielectric permittivity. Therefore, the structure is characterized by a positive refractive index for the frequencies in the first photonic band and by a negative effective refractive index for the frequencies in the second photonic band. Due to the fact that the refracted wave should propagate away from the interface, a wave incident on the crystal from a homogeneous medium with frequency lying in the first photonic band will refract positively, while a wave with frequency lying in the second band will refract negatively.

2.3.2 Numerical modelling results

Figure 2.7 shows numerical results from the-finite-difference-time-domain modelling of the refraction of a plane wave by a prism made of the photonic crystal having facets of length of 5 mm. The angle of incidence is 15 degrees with respect to the normal to the surface of the prism. Figure 2.7(a) corresponds to a frequency $f = 0.8$ THz lying in the first photonic band and positive refraction is clearly observed. Figure 2.7(b) corresponds to a frequency $f = 1.2$ THz lying in the second band and shows a distinct negative refraction effect.

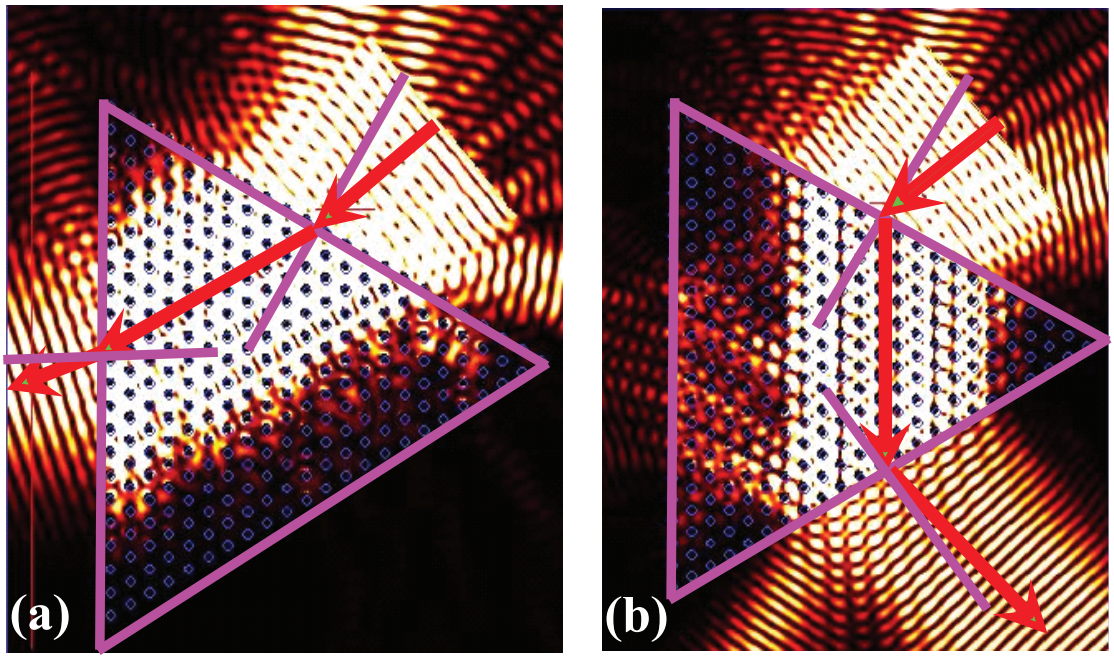

FIG. 2.7: Squared electric field for waves refracted on a photonic crystal prism. (a) Wave frequency $f = 0.8$ THz, positive refraction. (b) $f = 1.2$ THz, negative refraction.

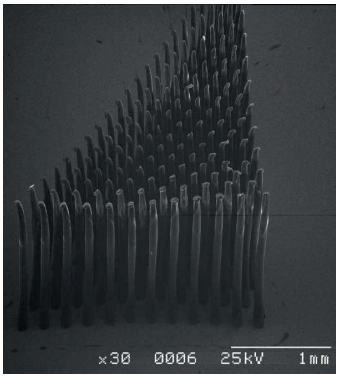

FIG. 2.8: The initial design of the photonic crystal prism. The separation of the rods on the right-hand facet is different from that in the bulk.

The prism shown in Fig.2.7 has the shape of an equilateral triangle. Initially, a prism in the form of a right-angled triangle (see Fig.2.8) was used but the experiments were unsuccessful because no refracted beam was detected in the direction predicted by the theory. However, during the numerical modelling it was realized that a facet of the photonic crystal which does not coincide with one of the main crystallographic axes, acts as an effective diffraction grating for the incident light, destroying the negative refraction effect through additional diffraction at the interface. As a result, most of the radiation has been diffracted from this effective diffraction grating and did not reach the receivers.

2.3.3 Comparison of theory and experiment

Experiments were performed by collaborators guided by the results of the numerical modelling and a micrograph of the sample used is shown on Fig.2.9.

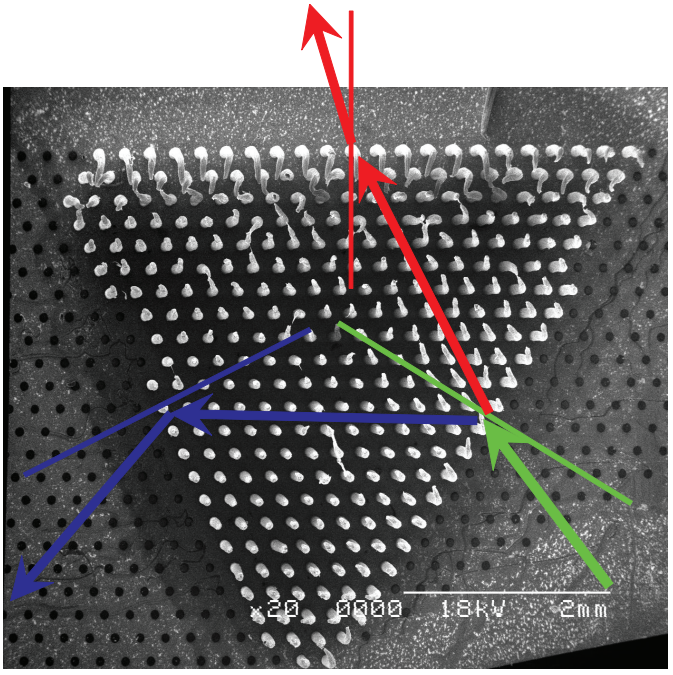

FIG. 2.9: Micrograph of the photonic crystal prism studied in the experiment. Arrows have been added to show the directions of the negatively (blue) and positively (red) refracted beams.

The details of the prism fabrication methods employed can be found in [43]. Briefly, high-aspect-ratio polymer pillars were formed by backside UV exposure of SU-8 50 on a glass substrate, before being sputtered with gold. Because the gold thickness is greater than the electromagnetic radiation skin depth, the pillars behave in effect like solid metallic rods.

The refraction of the THz light by a photonic crystal can be experimentally measured using a broadband spectrometer. The THz radiation was generated using a photoconductive switch, fabricated on low-temperature-grown GaAs and was detected electro-optically. After generation, the THz radiation was collected and focused onto the sample by a pair of parabolic mirrors. For both the cases of negative and positive refraction, a plane mirror placed at the THz beam focus allowed reference measurements to be undertaken to check the system alignment and performance. Another pair of parabolic mirrors, placed in an appropriate angular position, collected the radiation from the sample, which was then focused onto the detector. It should be noted that the parabolic mirrors focused the broadband THz beam onto, and collected the narrowband refracted beam from, the sample over an angular range of approximately 10 degrees which is much smaller than the measured angular separation of the refracted beams.

Figure 2.10(a) shows the typical temporal dependence of the reference signal obtained from the spectrometer. The Fourier transform, which is shown in the inset, indicates a usable bandwidth of approximately 3 THz with maximum power being output around 1 THz, which corresponds to the operating frequency of the device. Figure 2.10(b) shows the pulse that emerges from the negative refraction facet.

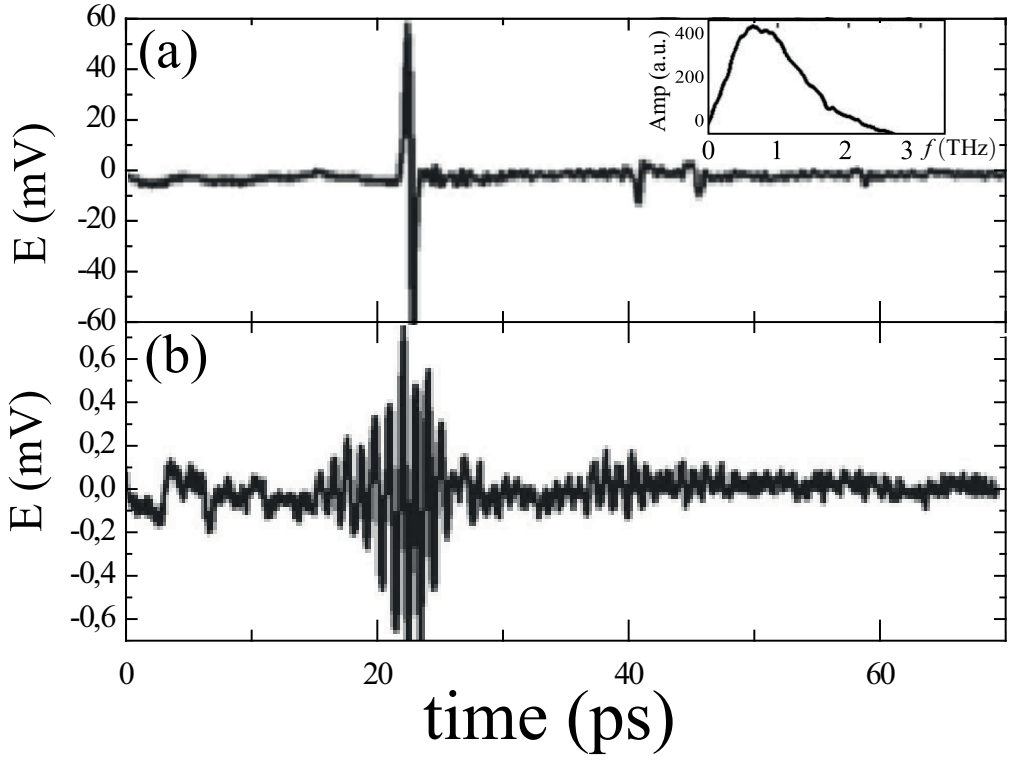

FIG. 2.10: (a) Temporal dependence of the reference signal. Inset shows the Fourier transform. (b) Temporal dependence of the negatively refracted beam.

Even though the amplitude is much reduced in the time domain, the negatively refracted pulse contains numerous oscillations. This pulse ringing is clear initial evidence that only a limited range of frequency components are steered by the device to emerge from the negative refraction facet. The THz beam emerging from the positive refraction facet is of a similar structure. The Fourier transforms of the pulses (Fig.2.11) show the spectral content contained in both the negatively and positively refracted components of the original, incident THz beam, the rest being filtered away by the device.

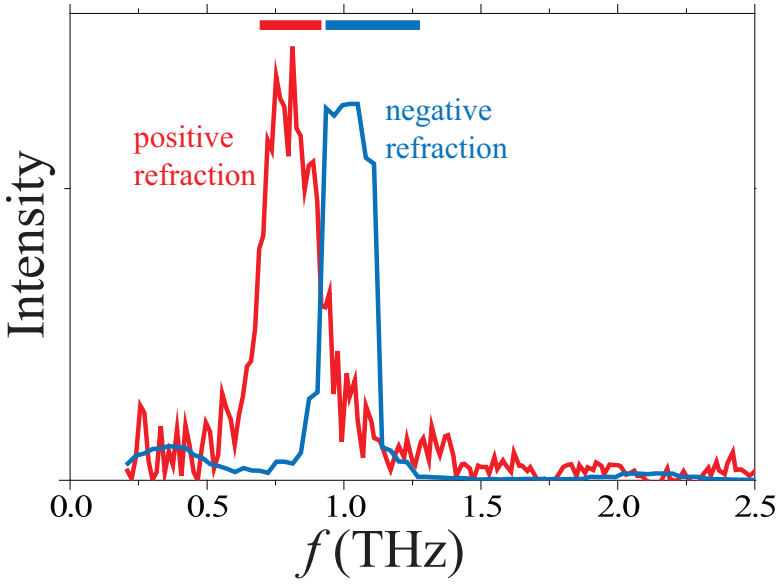

FIG. 2.11: (a) Fourier transforms of the refracted signals. Horizontal lines show the widths of the first and second bands, calculated by the complex band structure method.

It is clear that while there is some overlap of the tails of the spectral peaks, there are distinct pass-bands for the positively and negatively refracted waves, which correspond to the photonic bands having a positive and negative group velocities respectively. The positive refraction band extends from 0.73 to 0.91 THz, while the negatively refracted band covers the spectral range of 0.91 to 1.24 THz, when defined by their FWHM. In both bands, approximately 10 % of the incident beam power is refracted. The general form of these results is consistent with our theoretical band structure analysis, which should be recognized as being for a system consisting of an infinite array of pillars using a finite number of plane waves, whereas in the experiment a focused beam is incident on a finite structure. When losses are included, the value of f_P is no longer clear-cut and losses also reduce the value of f_J, and both these trends are consistent with the experimental observations. Also, limitations on the micromachining processes used to construct the prism mean that the pillar diameters are somewhat more narrow toward their tops, and this will further reduce the predicted frequencies.

In summary, we have demonstrated, for the first time to our knowledge, the ability of a metallic photonic crystal prism to filter a broadband THz beam in such a way that two angularly resolved beams at different frequencies emerge. Essentially, the device works in the way predicted by our theory: by positively refracting the frequency components in one interval and negatively refracting the frequency components in an adjacent interval by making use of the properties of the two lowest photonic bands of the crystal. It should also be noted that the top-hat shape of the transmission spectrum for the negatively refracted wave makes such a device attractive for use as a spectral filter.

We believe the proposed filter is useful advance in THz technology, particularly as currently there is a lack in practical realizations of interference or absorbing terahertz spectral filters - the approaches most commonly used in the optical range. Most of the existing terahertz spectral filters are based on periodic or quasiperiodic metal dielectric structures [44, 45] exhibiting resonant transmission (or absorption) due to the excitation of surface plasmon polariton modes at metal-dielectric interfaces. Our approach however is advantageous due to the fact that the field does not penetrate in the metal significantly, thus reducing the losses as compared to the metamaterial-based filters.

2.4 Summary of key original results

Main results obtained in Chapter 2.

- Making use of an established theoretical method to describe the scattering of plane wave from the side edge of one-dimensional photonic crystal, two new optical effects have been predicted analytically and also observed in numerical simulations - propagation normal to the interface of the transmitted electromagnetic field and spatial oscillations of the Poynting vector.
- A new type of spectral filter for the terahertz frequency range has been proposed. The design of the filter has been developed and refined using numerical modelling and the results compared with experimental measurements on a prototype structure.

Chapter 3

Eigenmode analysis of resonant photonic nanostructures

This chapter is dedicated to the study of eigenmode structure and nonlinear effects in certain resonant photonic nanostructures.

One investigation concerns the analysis of the eigenmode structure of a microcavity on organic cavity layer adjacent to a metal film. This work was done in collaboration with an experimental group from the University of Dresden [46]. An experimental sample was fabricated by our collaborators and a series of the reflectivity measurement experiments were made[1]

Another study is of the eigenmode structure of a periodic array of semiconductor quantum wells buried in the layers of a distributed Bragg reflector [47]. This work was done in collaboration with experimental groups from the University of Crete and the University of Cambridge. The sample was fabricated by the Crete group and a series of the reflectivity spectra measurements were performed. The Cambridge group performed the pump probe experiments revealing parametric amplification occurring in the structure[2]

The last section of the chapter presents unpublished results on the modelling of the parametric amplification that has been experimentally observed in the structure described above [3]

[1] I performed the numerical modelling of the reflectivity spectra and derived analytical expressions for the eigenfrequencies of the structure.

[2] I performed the numerical modelling of the reflectivity spectra and derived the approximate analytical expressions for the structure eigenfrequencies.

[3] I implemented a three-level formalism, which had been developed in [48], for the periodic quantum well structure and show that the simulation results agree well with the experimental data obtained by the Cambridge group.

However, before describing the three studies in details we present some relevant theoretical background material starting with a short overview of the transfer matrix method which is extensively used throughout the chapter. It is followed by the calculation of the eigenfrequency of a specific type of surface optical mode occurring at the interface of a metal film and a distributed Bragg reflector, a Tamm plasmon polariton. Finally, the derivation of the expression for the reflection coefficient from a semiconductor quantum well is presented.

3.1 Background theory

3.1.1 Transfer matrix method

A detailed description of the transfer matrix method can be found in [49] and we present only the key features that are relevant to our work here. We consider an arbitrary multilayered structure consisting of layers of isotropic material grown in the z-direction. The electromagnetic field can be decomposed into two polarizations: the TE polarisation, for which the electric field is orthogonal to the plane formed by the wavevector and the normal to the layers, and the TM polarisation for which the magnetic field is orthogonal to that plane.

In the case of the TE polarization we write the the electric field vector as $\vec{E} = (0, E_y, 0)$ and the magnetic field vector as $\vec{H} = (H_x, 0, H_z)$. We take the fields to have the harmonic time dependence $\sim \exp[-i\omega t]$ and without the loss of generality we can set the y component of the wavevector to zero. The spatial variation of the fields parallel to the structure is then $\sim \exp[ik_x x]$, where k_x is the same for all the layers. Then Maxwell equations can be reduced to the Helmholtz equation for the spatial dependence of the electric field E_y in each layer:

$$\frac{\partial^2 E_y}{\partial z^2} + k_z^2 E_y = 0, \tag{3.1}$$

where $k_z^2 = \varepsilon(\omega/c)^2 - k_x^2$, and ε is the layer dielectric permittivity. The general solution of the equation (3.1) is:

$$E_y = A\exp[ik_z z] + B\exp[-ik_z z], \tag{3.2}$$

where A is the amplitude of the forward propagating wave and B - that of the backward propagating wave. Now, in a homogeneous medium, if we know the amplitudes in the plane $z = z_0$, say, (A_0, B_0), the amplitudes (A_1, B_1) of the field in the plane $z = z_1$ are simply $A_1 = A_0\exp[ik_z(z_1 - z_0)], B_1 = B_0\exp[-ik_z(z_1 - z_0)]$. It is convenient to write this result in matrix form:

$$\begin{pmatrix} A_1 \\ B_1 \end{pmatrix} = \hat{M}\begin{pmatrix} A_0 \\ B_0 \end{pmatrix}; \quad \hat{M} = \begin{pmatrix} e^{ik_z d} & 0 \\ 0 & e^{-ik_z d} \end{pmatrix}, \tag{3.3}$$

where $d = z_1 - z_0$, and $\hat{M}$ is conventionally referred to as a transfer matrix. Here $\hat{M}$ is expressed in the basis of forward and backward propagating waves, but it is possible to transform to the basis of the tangential field components E_y and H_x. The tangential

components corresponding to Eq.(3.1) are:

$$E_y = A\exp[ik_z z] + B\exp[-ik_z z], \tag{3.4}$$

$$H_x = -\frac{k_z}{k_0}A\exp[ik_z z] + \frac{k_z}{k_0}B\exp[-ik_z z], \tag{3.5}$$

where $k_0 = \omega/c$. In matrix form:

$$\begin{pmatrix} E_y \\ H_x \end{pmatrix} = \hat{S}\begin{pmatrix} A \\ B \end{pmatrix}, \tag{3.6}$$

where

$$\hat{S} = \begin{pmatrix} 1 & 1 \\ -k_z/k_0 & k_z/k_0 \end{pmatrix}. \tag{3.7}$$

It follows that the transfer matrix in the basis of tangential components is $\hat{T} = \hat{S}\hat{M}\hat{S}^{-1}$ and

$$\begin{pmatrix} E_{y1} \\ H_{x1} \end{pmatrix} = \hat{T}\begin{pmatrix} E_{y0} \\ H_{x0} \end{pmatrix}, \tag{3.8}$$

where

$$\hat{T} = \begin{pmatrix} \cos(k_z d) & i(k_0/k_z)\sin(k_z d) \\ i(k_z/k_0)\sin(k_z d) & \cos k_z d \end{pmatrix}. \tag{3.9}$$

The matrix transferring the tangential fields across the interface of two layers with dielectric permittivities ε_1 and ε_2 is the unit matrix due to the electromagnetic boundary conditions. This fact can be used to derive the transfer matrix $\hat{L}$ across an interface in the case of the forward and backward propagating basis:

$$\hat{L} = \hat{S}_2^{-1}\hat{S}_1 = \frac{k_{z2}}{2k_{z1}}\begin{pmatrix} 1 + k_{z1}/k_{z2} & 1 - k_{z1}/k_{z2} \\ 1 - k_{z1}/k_{z2} & 1 + k_{z1}/k_{z2} \end{pmatrix}. \tag{3.10}$$

The corresponding results for the TM polarization can be derived in a similar manner, and in that case:

$$\hat{T} = \begin{pmatrix} \cos(k_z d) & ik_z/(\varepsilon k_0)\sin(k_z d) \\ ik_0\varepsilon/k_z\sin(k_z d) & \cos k_z d \end{pmatrix}. \tag{3.11}$$

$$\hat{L} = \frac{\varepsilon_1 k_{z2}}{2\varepsilon_2 k_{z1}} \begin{pmatrix} 1 + (\varepsilon_2 k_{z1})/(\varepsilon_1 k_{z2}) & 1 - (\varepsilon_2 k_{z1})/(\varepsilon_1 k_{z2}) \\ 1 - (\varepsilon_2 k_{z1})/(\varepsilon_1 k_{z2}) & 1 + (\varepsilon_2 k_{z1})/(\varepsilon_1 k_{z2}) \end{pmatrix}. \tag{3.12}$$

Thus, we now have expressions for all the matrix components in both bases and for both polarizations. By forming product of the appropriate layer and interface transfer matrices, we can obtain the transfer matrix of an arbitrary multilayered structure.

If we have the transfer matrix of a structure, we can calculate its transmission and reflection coefficients. In the basis of forward and backward propagating components, if we assume that the amplitude of the incident light is unity we can write:

$$\begin{pmatrix} t \\ 0 \end{pmatrix} = \hat{M} \begin{pmatrix} 1 \\ r \end{pmatrix}, \tag{3.13}$$

where r, t are the reflection and transmission coefficients respectively and $\hat{M}$ is the transfer matrix. It then follows that:

$$r = -\frac{\hat{M}_{21}}{\hat{M}_{22}}, \tag{3.14}$$

$$t = \frac{1}{\hat{M}_{22}}, \tag{3.15}$$

where the derivation of the expression for t has used the fact that all the transfer matrices for the structures placed in the symmetric environment, i.e. if the refractive indices of the surrounding media from the both sides of the structures are equal, since the determinant of such structure is equal to unity [50].

We can also derive the components of the transfer matrix from the reflection and transmission coefficients of the structure. Imagine an arbitrary layered structure bound with half-space of refractive index n_0 to the left and half-space of refractive index n_f to the right. We assume that we know the reflection and transmission coefficients for the light travelling at normal incidence from the left, denoted as r_l, t_l, and the reflection and transmission coefficients for the light travelling from the right, denoted as r_r, t_r. Our aim is to construct the transfer matrix of the layered structure $\hat{T}$ corresponding to the transfer of the electromagnetic field from the left side of the structure to the right side. We can write down two matrix equations:

$$\hat{T} \begin{pmatrix} 1 \\ r_l \end{pmatrix} = \begin{pmatrix} t_l \\ 0 \end{pmatrix}, \tag{3.16}$$

and

$$\hat{T}\begin{pmatrix}0\\ t_r\end{pmatrix}=\begin{pmatrix}r_r\\ 1\end{pmatrix}, \tag{3.17}$$

Since the system is not symmetric, it can be shown that the determinant of $\hat{T}$ in the case of normal incidence is equal to n_0/n_f. Using this relation and the four equations obtained from equation (3.16) and (3.17) we can evaluate the components of matrix $\hat{T}$:

$$\hat{T}=\frac{1}{t_r}\begin{pmatrix}(t_l t_r - r_l r_r)/t_r & r_r\\ -r_l & 1\end{pmatrix}. \tag{3.18}$$

For the case of normal incidence the following relations holds between t_l and t_r: $t_l = (n_0/n_f)t_r$. The picture simplifies drastically if $n_0 = n_f$. In this case $r_l = r_r = r, t_l = t_r = t$ and

$$\hat{T}=\frac{1}{t}\begin{pmatrix}(t^2 - r^2)/t & r\\ -r & 1\end{pmatrix}. \tag{3.19}$$

Using the transfer matrix approach it is also possible to derive the eigenvalues and eigenmodes of an infinite periodic structure. Applying Bloch's theorem for a periodic structure with period D:

$$\begin{pmatrix}E_y(z=D)\\ H_x(z=D)\end{pmatrix}=\hat{M}\begin{pmatrix}E_y(z=0)\\ H_x(z=0)\end{pmatrix}=e^{iKD}\begin{pmatrix}E_y(z=0)\\ H_x(z=0)\end{pmatrix}, \tag{3.20}$$

where $\hat{M}$ is the transfer matrix over the period of the structure and K is the Bloch vector. It follows that:

$$\cos(KD)=Tr(\hat{M})/2. \tag{3.21}$$

3.1.2 Tamm plasmon eigenfrequencies

In section 3.2 we consider the coupling of Tamm plasmon modes in the organic microcavities and obtain the analytical expressions for the resulting eigenmodes. In preparation, here we provide a definition of the Tamm plasmon polaritons and show how to obtain the dispersion relation for a single Tamm plasmon mode.

The Tamm plasmon polariton is a special type of cavity mode that can exist in a cavity with mirrors made of a metallic layer on one side and a Bragg reflector on the other side. Due to the use of a metallic mirror on one side, the cavity length needed to support the

eigenmode at a fixed wavelength is smaller than that of a conventional Bragg reflector cavity for the same wavelength. At the same time, due to the fact that the mode is still a cavity mode, it is characterized with a parabolic in-plane dispersion relation. Therefore, a Tamm plasmon mode can be used as a realization of a spatially compact (because of the small cavity length) and slow light (because of the parabolic dispersion and thus small group velocity for the small in-plane wavevectors). Despite the simplicity of the concept, Tamm plasmon polaritons were only proposed recently but have since attracted a lot of attention. Some of the many applications of Tamm plasmon polaritons include the realization of polariton logic devices [51], and the control of the radiative decay of the quantum dots [52].

In order to derive the dispersion relation for a Tamm plasmon polariton, we consider the structure shown in Fig.3.1 and look for optical modes localized close to the metal

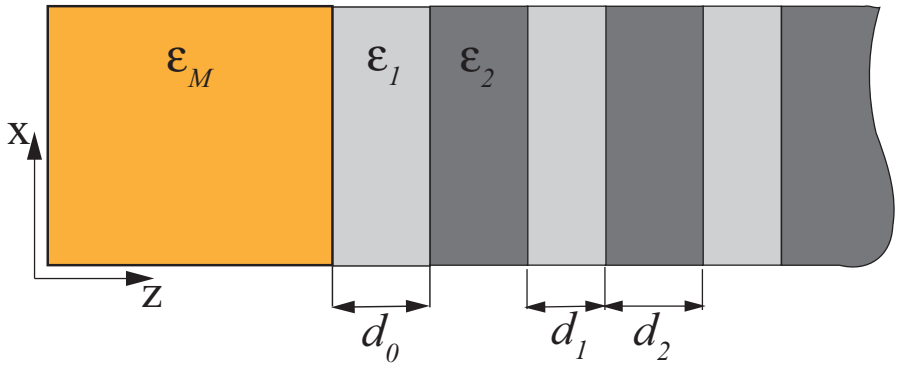

FIG. 3.1: The simplest realization of the structure where a Tamm plasmon mode can exist. A semi-infinite Bragg reflector (grey layers of dielectric permittivity ε_1 and ε_2) adjacent to a semi-infinite metal layer (yellow) with dielectric permittivity ε_M. The thickness of the dielectric layer adjacent to the metal may be varied to tune the frequency of the mode.

layer. To find the eigenfrequencies of such modes, we can utilize the well known general gcardinal condition for the eigenmodes of a general cavity:

$$r_L r_R e^{2i\Phi} = 1, \tag{3.22}$$

where r_L, r_R are the reflection coefficients of the left and right mirrors and Φ is the phase change across the width of the cavity.

In the case of normal incidence the reflection coefficient of the metal layer is:

$$r_M = \frac{\sqrt{\varepsilon_1} - \sqrt{\varepsilon_M}}{\sqrt{\varepsilon_1} + \sqrt{\varepsilon_M}} = \frac{n_1 - n_M}{n_1 + n_M}. \tag{3.23}$$

In the simplest Drude model:

$$\varepsilon_M = 1 - \omega_p^2/\omega^2, \tag{3.24}$$

where ω_p is the plasma frequency of the metal. In the application considered here the eigenfrequencies of the modes are around 1 eV and are much smaller than the plasma frequency which for the common noble metals is about 10 eV [53]. Therefore, the reflection coefficient of the metal half-space can be approximated as

$$r_M \approx \exp\left[i\left(\pi + \frac{2\sqrt{\varepsilon_1}\omega}{\omega_p}\right)\right]. \tag{3.25}$$

The reflection coefficient of the Bragg reflector calculated at the interface of layers with refractive indices $n_1 = \sqrt{\varepsilon_1}$ and $n_2 = \sqrt{\varepsilon_2}$ for the frequency in the vicinity of the stop band centre depends on the relation between n_1 and n_2. If $n_1 > n_2$ then

$$r_{Br} = \exp\left(\frac{i\pi n_2}{|n_1 - n_2|}\frac{\omega - \omega_0}{\omega_0}\right), \tag{3.26}$$

and if $n_1 < n_2$ then

$$r_{Br} = -\exp\left(\frac{i\pi n_1}{|n_1 - n_2|}\frac{\omega - \omega_0}{\omega_0}\right), \tag{3.27}$$

where ω_0 is the Bragg reflector stop band centre frequency. Finally, the phase change Φ in the vicinity of the stop band centre is given by:

$$\Phi \approx \frac{\pi}{2}\left(1 + \frac{\omega - \omega_0}{\omega_0}\right). \tag{3.28}$$

For the case $n_1 > n_2$ the eigenmode condition of equation (3.22) requires:

$$\pi + \frac{2n_1\omega}{\omega_p} + \pi + \pi\frac{\omega - \omega_0}{\omega_0} + \pi\frac{n_2}{n_1 - n_2}\frac{\omega - \omega_0}{\omega_0} = 2\pi. \tag{3.29}$$

which has the solution

$$\omega = \frac{\omega_0}{1 + 2\omega_0/(\pi\omega_p)|n_1 - n_2|}. \tag{3.30}$$

Equation (3.30) refers to the case when the thickness of the layer adjacent to the metal layer is equal to that of the other layers of the same type forming the Bragg reflector. However, by varying the thickness it is possible to tune the Tamm plasmon frequency exactly to the Bragg frequency ω_0.

It should be noted that when $n_2 > n_1$ there will be an additional contribution of π to the overall phase at the left side of the equation (3.29) and there will be no solutions in

the vicinity of the Bragg frequency.

3.1.3 Reflection coefficient of an exciton quantum well

In section 3.3 of this chapter we study a particular type of resonant periodic nanostructures in which light couples to excitons excited in quantum wells embedded in the layers of a Bragg reflector. To calculate the eigenfrequencies of the nanostructures using transfer matrix theory we need to derive the reflection coefficient for a single quantum well with a view to incorporating the effect of the quantum well excitons in the previously discussed transfer matrix theory. The detailed derivation of the quantum well reflection coefficient can be found in [54] and only the main steps are described here. Also, for simplicity we deal only with the normal incidence of electromagnetic waves on the quantum well.

In the case of normal incidence the electric field of the system is governed by the equation:

$$\frac{\partial^2 E}{\partial z^2} + \varepsilon k_0^2 E = -k_0^2 4\pi P_{exc}, \tag{3.31}$$

where ε is the background dielectric permittivity of the quantum well, $k_0 = \omega/c$, and P_{exc} is the excitonic polarization given by

$$4\pi P_{exc} = G\Phi(z) \int \Phi^*(z'')E(z'')dz''. \tag{3.32}$$

Here $\Phi(z) = \Psi_{exc}(R = 0, \rho = 0, z_e = z_h = z)$ is the exciton wavefunction taken with electron and hole having the same position in space,

$$G = \frac{Q}{\omega_0 - \omega - i\Gamma}, \tag{3.33}$$

where

$$Q = \pi a_B^3 \omega_{LT}, \tag{3.34}$$

in which a_B is the exciton effective Bohr radius, ω_{LT} is the longitudinal-transverse splitting, ω_0 is the exciton frequency and Γ is the nonradiative damping. $\Phi(z)$ can be chosen to be real when the origin of z coincides with the centre of the quantum well.

The general solution of an equation of the type $E''(x) + k^2 E = -F(x)$ can be written in the form:

$$E = E_1 \exp[ikx] + E_2 \exp[-ikx] + \frac{i}{2k} \int dx\prime \exp[ik(x - x')]F(x'). \tag{3.35}$$

Thus, when a wave with amplitude E_0 is incident from $z < 0$ on the quantum well, the solution to Eq. (3.31) can be written as:

$$E(z) = E_0 \exp[ikz] + \frac{ik_0^2}{2k} G \int dz' \exp[ik(z - z')]\Phi(z') \int \Phi^*(z'')E(z'')dz''. \tag{3.36}$$

Multiplying this equation by $\Phi(z)$ and integrating over z gives the following algebraic equation for $\Lambda = \int E(z)\Phi(z)dz$:

$$\Lambda = \Lambda_0 + i\frac{k_0^2}{k} G(\omega)\Lambda \int \int dzdz' \exp[ik(z - z')]\Phi(z)\Phi(z'), \tag{3.37}$$

where $\Lambda_0 = E_0 \int dz\Phi(z)E(z)$. The solution for Λ is then:

$$\Lambda = \int E(z)\Phi(z)dz = \frac{\Lambda_0}{1 - (ik_0^2)/(k)G(\omega) \int \int dzdz' \exp[ik(z - z')]\Phi(z)\Phi(z')}, \tag{3.38}$$

which can be substituted into Eq. (3.36) to give:

$$E(z) = E_0 \exp[ikz] + \frac{E_0(ik_0^2)/(2k)Q \int dz'' \exp[ikz'']\Phi(z'') \int dz' \exp[ik(z - z')]\Phi(z')}{\omega_0 - \omega - i\Gamma - 1 - i\frac{k_0^2}{k}Q \int \int dz''dz' \exp[ik(z'' - z')]\Phi(z'')\Phi(z')}. \tag{3.39}$$

The reflection and transmission coefficients are defined as:

$$r = \frac{E(z) - E_0(z)e^{-ikz}}{E_0 e^{-ikz}}_{(z\to-\infty)}; \quad t = \frac{E(z)}{E_0(z)e^{ikz}}_{(z\to\infty)}. \tag{3.40}$$

And using the fact that $\Phi(z)$ is an even function with respect to z, it follows that:

$$r = \frac{i\Gamma_0}{\tilde{\omega}_0 - \omega - i(\Gamma + \Gamma_0)}; \quad t = 1 + r, \tag{3.41}$$

where

$$\Gamma_0 = \frac{Qk_0^2}{2k} \left[\int \Phi(z) \cos(kz)dz \right]^2 \tag{3.42}$$

is called the exciton radiative broadening and

$$\tilde{\omega}_0 = \omega_0 + \frac{Qk_0^2}{2k} \int \int dzdz'\Phi(z)\Phi(z') \sin(k|z - z'|) \tag{3.43}$$

is the renormalisation of the exciton resonance frequency due to the polariton effect. As soon as we know the reflection and transmission coefficients of the quantum well we can easily reconstruct its transfer matrix using the expression (3.19) from section 3.1.1.

3.2 Parabolic polarization splitting of Tamm states in a metal-organic microcavity

In this section we study the optical properties of the structure shown in Fig.3.2 which consists of an a metallic layer and adjacent organic cavity layer sandwiched between two Bragg reflectors. The structure was grown and studied experimentally by our collaborators in Dresden.

3.2.1 Structure and experimental set up

The sample shown in Fig.3.2 consists of a microcavity structure composed of two dis-

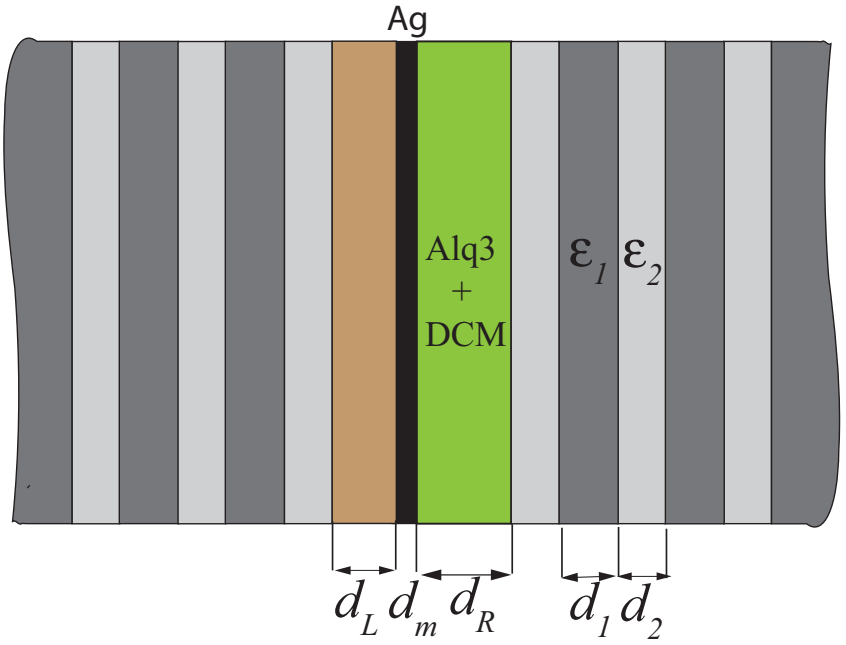

FIG. 3.2: Design of the structure investigated. Two Bragg reflectors enclose the cavity layer and the silver layer of variable thickness (gradient from 0 to 40 nm). The thicknesses of the layers being most sensitive to the eigenmodes are denoted by d_i.

tributed Bragg reflectors (DBRs) with two embedded layers: a thin silver layer and an organic half-λ cavity layer made of the host-guest system tris-8-hydroxyquinoline aluminium (Alq3) doped with 2 wt.percent of 4-dicyanomethylene-2 -methyl-6-p-imethylaminostyryl-4 H-pyran (DCM). The silver layer was deposited with a thickness graded from 0 to 40 nm on top of the first DBR (left hand side of Fig. 3.2) and then enclosed by the organic cavity layer and the top DBR. The optical thicknesses of both the cavity and the 21 alternating $\lambda/4$ layers of TiO_2/SiO_2 forming each DBR were chosen to correspond to the maximum of the DCM emission at 630 nm, so the structure could

be used in future to demonstrate direct coupling between exciton and Tamm plasmon states. However, the current structure used in the initial experiment discussed here was for proof-of-concept only, and the concentration of DCM was actually too small to achieve considerable exciton absorption. Due to the wedge shape, the silver layer only partly covers the first mirror resulting in a high quality, all dielectric microcavity as well as two microcavities separated by a varying metal thickness up to 40 nm and each capable of supporting Tamm plasmon polaritons that can couple through the thin silver film. A μ-photoluminescence (μ-PL) microscope setup was utilized to investigate the angle-resolved emission spectra of the structure at room temperature. By focusing the beam of a 405 nm cw laser with a microscope objective ($\times$25, NA 0.5) to a spot diameter of less than 2 μm, areas either with or without metal could be selectively excited. Such a small spot size was necessary in order to avoid collecting PL-signal from areas with different thicknesses of the silver layer and resulting in different spectral features. The high aperture of the objective ($\times$63, NA 0.8) collecting the sample emission covered a large angular range of around $\pm 55^o$ in the far field geometry. A second lens was used to map the Fourier plane of the first collecting objective, enabling the observation of the dependence $E(k)$. A polarization filter installed in front of the spectrometer was utilized to characterize the polarization properties of the sample emission. The spectrograph was equipped with a cooled charge-coupled device to record the spectrally, angularly, and polarization-resolved PL signal.

3.2.2 Comparison of results of numerical modelling with experiment

In Fig.3.3, the experimental angle-resolved emission spectra of the metal organic microcavity are shown for different metal thicknesses (left panels of Figs.3.3(a-d). These are compared to the results of numerical calculations based on the transfer matrix method (right panels). In the numeric simulation the full transfer matrix has been calculated based on the formalism presented in section 3.1.1. Transmission spectra were then calculated using (3.15) for different incidence angles resulting in the transmission coefficient map. Due to the small concentration of the DCM, the transmission spectra was almost identical to the experimental emission spectra. Three phenomena are apparent: First, because of the graded thickness of the metal layer placed inside the cavity and the small excitation spot used, an increasing metal thickness means moving away from metal-free areas. Thus, any scatter of the emission into metal free areas is reduced, leading to a weaker coupling into the original cavity mode at 632 nm. This behaviour is not accounted for in the numerical calculations, since we assume a constant metal thickness over large areas (compare left and right panels in Figs.3.3(a-d) at 632 nm).

Next, depending on the metal thickness, two modes arise. The spectrally broad emission above 700 nm corresponds to emission into the long wavelength sideband of the DBRs. At silver thicknesses of ≈25 nm, an initially broad mode emerges from the long wavelength sideband. This is a so-called Tamm plasmon-polariton, which has its origin in the localization of the electromagnetic field next to the metal layer. In addition to

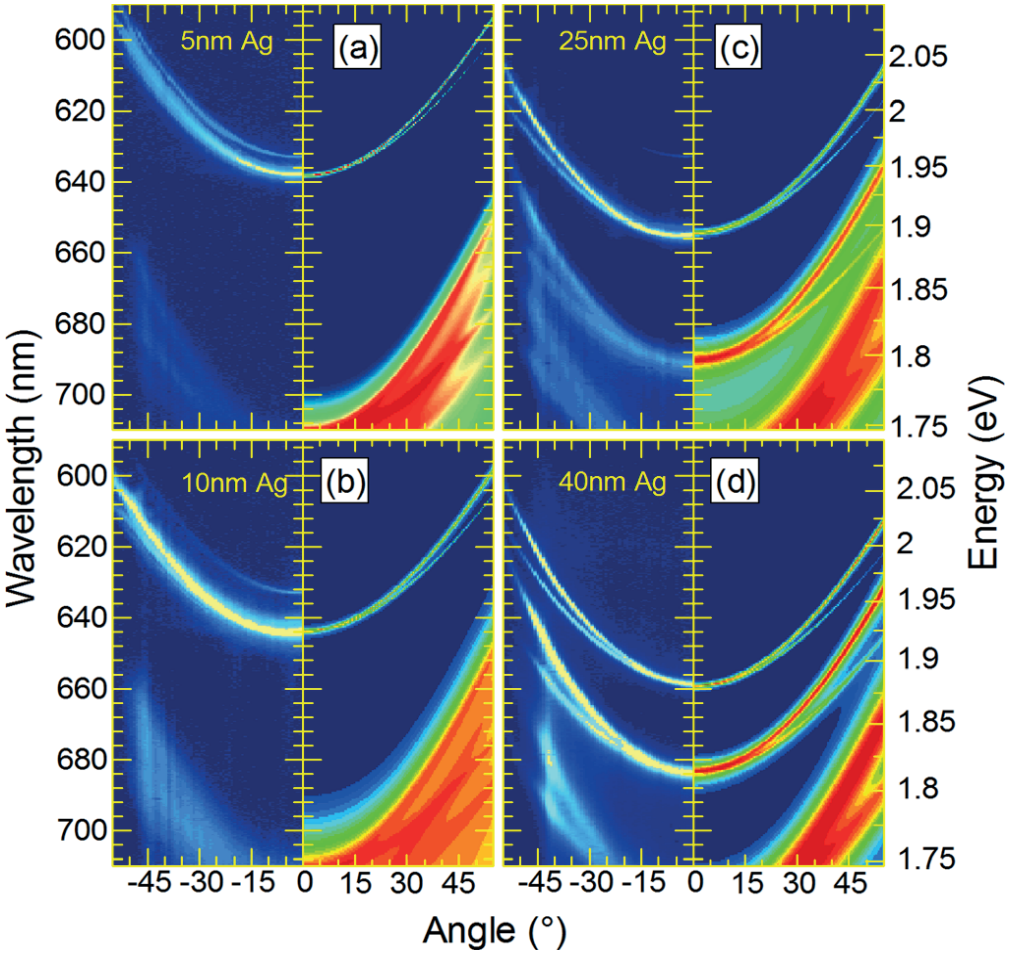

FIG. 3.3: Experimentally observed angle-resolved emission spectra (left panels) along with numerically calculated spectra (right panels). Deviations of the shape of the parabolae are due to imperfect refractive indices and their dispersions, on which the simulations are based.

this, a high energy resonance is observed, which at zero metal thickness converges to the original cavity mode. As metal is introduced, it starts shifting to the red. The reason for this shift is the coupling of this mode to the Tamm plasmon polariton evidenced by a clear anticrossing behaviour of the modes involved. Finally, at oblique angles and certain thicknesses of the embedded metal layer, a splitting of each mode is observed. Moreover, this splitting increases towards large angles of incidence. We observe that the polarizations of both branches are orthogonal to each other, characteristic of a splitting between TE- (lower branch) and TM-polarization (upper branch) modes. With

increasing metal thickness, the modes become increasingly detuned with respect to the centre of the DBR stop bands. The most sensitive way to control these phase shifts is by varying the thickness of the metal layer. In addition to the phase shift at the dielectric/metal interface, the reflectance and transmittance of this layer can be varied, which affects the coupling of the resonant modes. The observed splitting is strongly pronounced, reaching values of 37 meV for the shifted cavity mode and 45 meV for the Tamm plasmon polariton state at angles $\pm 55^o$ and a silver layer thickness of 40 nm.

3.2.3 Analytical expressions for the system eigenfrequencies

We start the analytical treatment of the system from writing down its transfer matrix:

$$A\begin{pmatrix}1\\ r_R\end{pmatrix}=\begin{pmatrix}e^{i\phi_R} & 0\\ 0 & \mathrm{e}^{-i\phi_R}\end{pmatrix}\begin{pmatrix}(t_-t_+ - r_-r_+)/t_- & r_-/t_-\\ -r_+/t_- & 1/t_-\end{pmatrix}\begin{pmatrix}e^{i\phi_L} & 0\\ 0 & e^{-i\phi_L}\end{pmatrix}\begin{pmatrix}r_L\\ 1\end{pmatrix}, \quad (3.44)$$

where A is a constant, r_L, r_R are respectively the reflection coefficients from the left and the right Bragg mirrors, ϕ_L, ϕ_R are respectively the phases gained in the left and the right parts of the cavity, and $r_\pm, t_\pm$ are the reflection and transmission coefficients of the metal layer (reflection (r) and transmission (t) from the left cavity to the right one corresponds to a plus sign and the opposite direction to a minus sign).

Eliminating A from Eq.(3.44) gives the equation for the eigenfrequencies:

$$\left(1-\frac{1}{r_Lr_+e^{-2i\phi_L}}\right)\left(1-\frac{1}{r_Rr_-e^{-2i\phi_R}}\right)=\frac{t_-t_+}{r_-r_+}. \quad (3.45)$$

Comparison with the Eq.(3.22) shows that the left side of the Eq.(3.45) contains two factors, whose roots correspond to the individual Tamm plasmons at the left and the right metal boundaries respectively. The right-hand side of Eq.(3.45) describes the coupling between the two Tamm states. It is now necessary to express Eq.(3.45) in terms of the parameters of the structure. We begin by looking at the right-hand side of the equation.

For the TE polarization

$$-\frac{t_-t_+}{r_-r_+}=\frac{4k_{zR}k_{zL}\kappa^2}{\cosh^2(\kappa d_m)(k_{zL}\kappa-k_{zR}\kappa)^2+\sinh^2(\kappa d_m)(\kappa^2+k_{zR}k_{zL})^2}, \quad (3.46)$$

where $k_{zm}=\sqrt{\varepsilon_m k_0^2-k_x^2}$, d_m is the thickness of the metal layer, $k_{zR,L}=\sqrt{\varepsilon_{R,L}k_0^2-k_x^2}$, $\varepsilon_L=n_L^2, \varepsilon_R=n_R^2, \varepsilon_m=n_m^2$ are the dielectric permittivities of left cavity, right cavity

and the metal layer respectively, and $\kappa = ik_{zm}$. There is analogous formula for the TM polarization. We assume that the transmission through the metal layer is very small, and thus the expression at the right-hand side of Eq.(3.47) is small, which will lead to the small splitting of the Tamm plasmon states compared to the frequencies of the Tamm plasmons. We then neglect the frequency and incidence angle dispersion of this coupling term, since the frequency and wavvector shift corrections would be proportional to a higher order of a small quantity. If we set $\omega = \omega_0$ and $k_x = 0$ in Eq.(3.47), where ω_0 is the Bragg reflector stop band centre frequency, we get the expression which is the same for both polarizations:

$$-\frac{t_- t_+}{r_- r_+} = -\frac{4n_R n_L|\varepsilon_m|}{\cosh^2(|n_m|\omega_0/cd_m)(n_L|n_m| - |n_m|n_R)^2 + \sinh^2(|n_m|\omega_0/cd_m)(|\varepsilon_m| + n_L n_R)}. \tag{3.47}$$

We now consider the left-hand side of the Eq.(3.45), beginning with the coefficients of reflection for the metal layer. When light is incident on the metal layer from the left cavity in the TE polarization, the reflection coefficient is given by

$$r_{TE+} = \frac{i\kappa(k_{zL} - k_{zR}) + \tanh(\kappa d_m)(-\kappa^2 - k_{zR}k_{zL})}{i\kappa(k_{zL} + k_{zR}) + \tanh(\kappa d_m)(\kappa^2 - k_{zR}k_{zL})}. \tag{3.48}$$

At frequencies well below the plasma frequency, $\kappa d_m \gg 1$ and $\tanh(\kappa d_m) \approx 1$, and

$$r_{TE+} \approx -\frac{1 - ik_{zL}/\kappa}{1 + ik_{zL}/\kappa}, \tag{3.49}$$

which can be written in terms of low frequency and small angle of incidence as

$$r_{TE+} \approx \exp\left(i\left[\pi + 2n_L\omega/\omega_p\sqrt{\varepsilon_b} - \omega/n_L/\omega_p/\sqrt{\varepsilon_b}\theta^2\right]\right), \tag{3.50}$$

where ω_p is the metal plasma frequency, and ε_b is the metal background dielectric constant. The corresponding results for the TM polarization are:

$$r_{TM+} = \frac{i\kappa\varepsilon_m(k_{zR}n_L/n_R - k_{zL}n_R/n_L) - \tanh(\kappa d_m)(\kappa^2 n_L n_R - k_{zR}k_{zL}/n_R/n_L\varepsilon_m^2)}{i\kappa\varepsilon_m(k_{zR}n_L/n_R + k_{zL}n_R/n_L) - \tanh(\kappa d_m)(\kappa^2 n_L n_R - k_{zR}k_{zL}/n_R/n_L\varepsilon_m^2)}, \tag{3.51}$$

$$r_{TM+} \approx -\frac{1 - i(\varepsilon_L\kappa)/(\varepsilon_m k_{zL})}{1 + i(\varepsilon_L\kappa)/(\varepsilon_m k_{zL})}, \tag{3.52}$$

$$r_{TM+} \approx \exp\left(i\left[\pi + 2n_L\omega/\omega_p\sqrt{\varepsilon_b} + \omega/n_L/\omega_p/\sqrt{\varepsilon_b}\theta^2\right]\right). \tag{3.53}$$

The expressions for r_{TE-} and r_{TM-} are obtained from Eqs. (3.50),(3.53) by changing n_L to n_R.

To calculate the reflection coefficients for the Bragg reflectors, that appear on the left-hand side of Eq.(3.45) it is instructive to recall that for a light in a medium A incident on an interface with medium B the reflection coefficient can be expressed in terms of the wave impedances Z_A and Z_B given by the ratio between the tangential components of the magnetic and electric fields $Z_i = H_i/E_i$ at the interface:

$$r_{AB} = \frac{Z_A - Z_B}{Z_A + Z_B}. \tag{3.54}$$

The impedances in the cavities for both polarizations are given by simple expressions:

$$Z^{TE}_{L,R} = -\frac{k_{z(L,R)}}{k_0}, \tag{3.55}$$

$$Z^{TM}_{L,R} = \frac{n^2_{L,R} k_0}{k_{z(L,R)}}. \tag{3.56}$$

The impedances at the internal interfaces of the Bragg reflectors can be obtained using the Bloch theorem. We assume that $z = 0$ coincides with an interface of the reflector and use the Bloch theorem:

$$\begin{pmatrix} E(z=D) \\ H(z=D) \end{pmatrix} = \hat{T} \begin{pmatrix} E(z=0) \\ H(z=0) \end{pmatrix} = e^{iKD} \begin{pmatrix} E(z=0) \\ H(z=0) \end{pmatrix}, \tag{3.57}$$

where D is the period of the structure, $\hat{T}$ is the transfer matrix for the period of the Bragg reflector, and K is the Bloch wavevector which can be obtained using Eq.(3.21). The expression for the wave impedance then is

$$Z_{Br} = H/E = \frac{\exp[iKD] - \hat{T}_{11}}{\hat{T}_{12}}. \tag{3.58}$$

The general expressions for $r^{TE,TM}_{L,R}$ then from Eq.(3.54):

$$r^{TE}_{L,R} = \frac{-k_{z(L,R)}/k_0 - Z^{TE}_{Br}}{-k_{z(L,R)}/k_0 + Z^{TE}_{Br}}, \tag{3.59}$$

$$r^{TM}_{L,R} = \frac{n^2_{L,R} k_0/k_{z(L,R)} - Z^{TM}_{Br}}{n^2_{L,R} k_0/k_{z(L,R)} + Z^{TM}_{Br}}. \tag{3.60}$$

At frequencies in the vicinity of the Bragg reflector stop band centre and at small incidence angle θ reflection coefficients can be approximated as:

$$r_{L,R}^{TE} \approx \exp\left[i\left(\frac{\pi n_{L,R}(\omega-\omega_0)}{|n_1-n_2|\omega_0}\left(1-\frac{\theta^2}{2n_1n_2}\right)\right)\right], \tag{3.61}$$

$$r_{L,R}^{TM} \approx \exp\left[i\left(\frac{\pi n_{L,R}(\omega-\omega_0)}{|n_1-n_2|\omega_0}\left(1+\frac{\theta^2}{2n_1n_2}\right)\right)\right], \tag{3.62}$$

where n_1, n_2 are the refractive indices of the Bragg reflector layers. The quantities on the left-hand side of Eq.(3.45) that remain to be evaluated are the cavity transit phase changes. ϕ_L and ϕ_R in the approximation of frequencies in the vicinity of the Bragg frequency, for the small angles of incidence and for cavity optical thicknesses equal to a quarter of the Bragg wavelength are given by:

$$2\phi_{L,R} = \pi\left(1+\frac{\omega-\omega_0}{\omega_0}-\frac{\theta^2}{2n_{L,R}^2}\right). \tag{3.63}$$

Finally, the equation for the eigenfrequencies of the structure can be written in the form:

$$(\omega-\omega_{TP,L}(\theta))(\omega-\omega_{TP,R}(\theta)) = \Omega^2 = \tag{3.64}$$
$$= \Delta\frac{\omega_0^2(n_2-n_1)^2}{(2n_L\omega_0/\omega_p+\pi(n_2+n_L-n_1)/(n_2-n_1))(2n_R\omega_0/\omega_p+\pi(n_2+n_R-n_1)/(n_2-n_1))},$$

where Δ is the expression at the right hand side of Eq.(3.47), and $\omega_{TP,(L,R)}$ are the angle-dependent eigenfrequencies of the Tamm plasmon polaritons in each cavity. The eigenfrequencies of the structure for the two polarization are then given by:

$$\omega_{1,2} = \frac{\omega_{TP,L}+\omega_{TP,R}}{2} \pm \sqrt{\frac{(\omega_{TP,L}-\omega_{TP,R})^2}{4}+\Omega^2}. \tag{3.65}$$

.

To verify the analytical formalism we have compared it with the experimental results and numerical results. Fig.3.4(a) shows the good agreement between the analytical approximations and the numerical results. Figure 3.4(b) illustrates large TE-TM splitting of Tamm plasmon modes.

In summary, the photon density of states of a microcavity changes substantially when a silver layer is embedded. The cavity mode is red-shifted due to coupling with the Tamm plasmon-polariton, and we are able to observe the associated spectral changes by using the emission spectrum of an organic semiconductor, which provides large oscillator strengths over a wide spectral range.

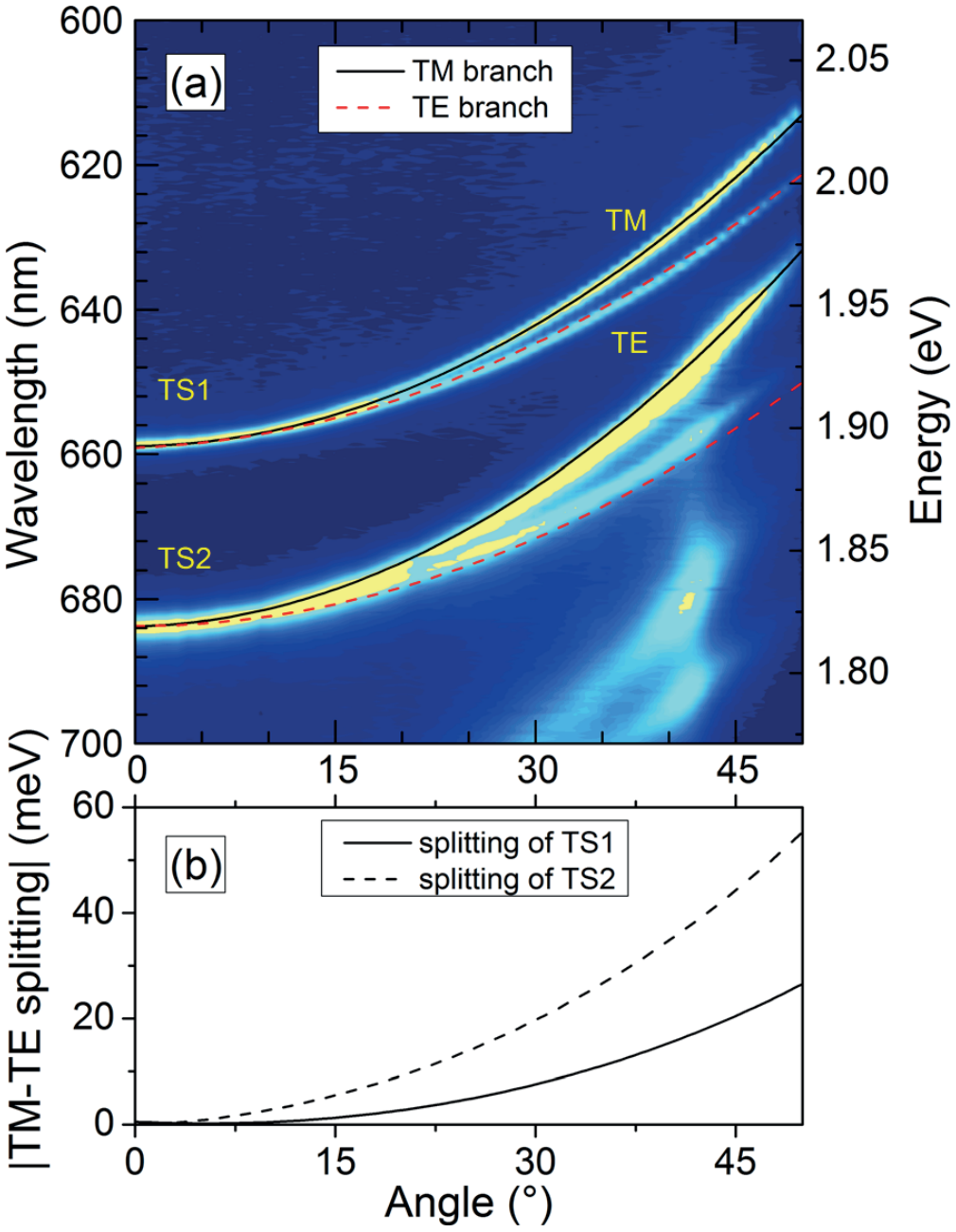

FIG. 3.4: (a) For the special case of a 40 nm silver layer inside the cavity, analytical results (black solid and red dashed line) showing good agreement with the numerical results. (b) Parabolic dependence of the splitting between the TE- and TM-modes of the shifted cavity resonance and Tamm plasmon-polariton as a function of the angle of incidence.

3.3 Eigenmode structure of periodic array of quantum wells buried in layers of one-dimensional photonic crystal.

In this section we study the linear optical properties of the Bragg structure shown in Fig.3.5(a), which comprises a periodic array of quarter-wavelength layers of GaAs with

refractive index $n_1 = n_{\mathrm{GaAs}} = 3.5$ and pseudo-layers AlAs/GaAs/InGaAs/GaAs/AlAs with effective refractive index $n_2 = n_{eff} = 3.2$ and effective optical length equal to $\lambda/4$. The pseudo-layers have at their centre 10 nm wide $In_{0.1}Ga_{0.9}As$ quantum wells which can support excitons with a ground state energy of 1.418 eV. Fig.3.5(b) shows experimental reflection spectra at 32 K which have been obtained by our collaborators in Crete. The structure has a wedge-like form, so that the effective layer thicknesses and hence the photonic stop-band frequency changes along the structure. In particular, the high-frequency edge of the stop-band, which is close to the exciton energy, varies from 1.38 to 1.44 eV.

The sharp extrema in the reflection spectra correspond to the eigenmodes of the system. It should be noted, that the exciton eigenfrequency can correspond to both the dips in the reflection spectra when the electric field antinodes are in the vicinity of the quantum wells and the sharp maxima in the reflection when the electric field nodes are in the vicinity of the quantum wells.

The dispersion of the eigenmodes can be extracted from the reflection spectra. The anticrossing behaviour of the exciton mode and a Bloch photonic mode positioned at the band-gap edge can be observed in the spectra. Moreover, in the case of resonance between the photonic band-gap edge and the exciton frequency, a triplet structure is observed in the spectra. The spectra have been calculated the spectra numerically using the transfer matrix method and are depicted in Fig.3.5(c). It can be seen, that the numerical model agrees well with the experimental data. However it is also instructive to derive some analytical expressions for the eigenmode frequencies.

A thorough analysis of the similar structures was performed by Ivchenko *et al.* in 2004 [54]. Using that theory, it is straightforward to show that in the case of the quarter-wavelength photonic crystal with quantum wells, the mode structure is defined by the equation

$$\cos(KD) = \left(\cos^2(\phi) - \frac{n_1^2 + n_2^2}{2n_1 n_2}\sin^2(\phi)\right) - \\ - \frac{\Gamma_0}{\omega_X - \omega - i\Gamma}\frac{(n_1+n_2)^2}{2n_1 n_2}\left(\sin(2\phi) - 2\frac{n_1 - n_2}{n_1 + n2}\sin(\phi)\right) \tag{3.66}$$

for the Bloch wavevector K, where $\phi = \pi\omega/(2\omega_B)$. Here ω_B is the stop-band centre frequency, Γ - is the non-radiative exciton decay rate, Γ_0 is the radiative exciton broadening given by Eq.(3.42), ω_X is the exciton frequency, and D is the period of the structure. In what follows we will neglect the non-radiative exciton decay rate Γ, which is negligible for the cryogenic temperatures considered. We note that first terms enclosed in the first parentheses on the right hand-side coincide with the dispersion relation for the Bragg reflector without quantum wells and thus correspond to the non-resonant contribution

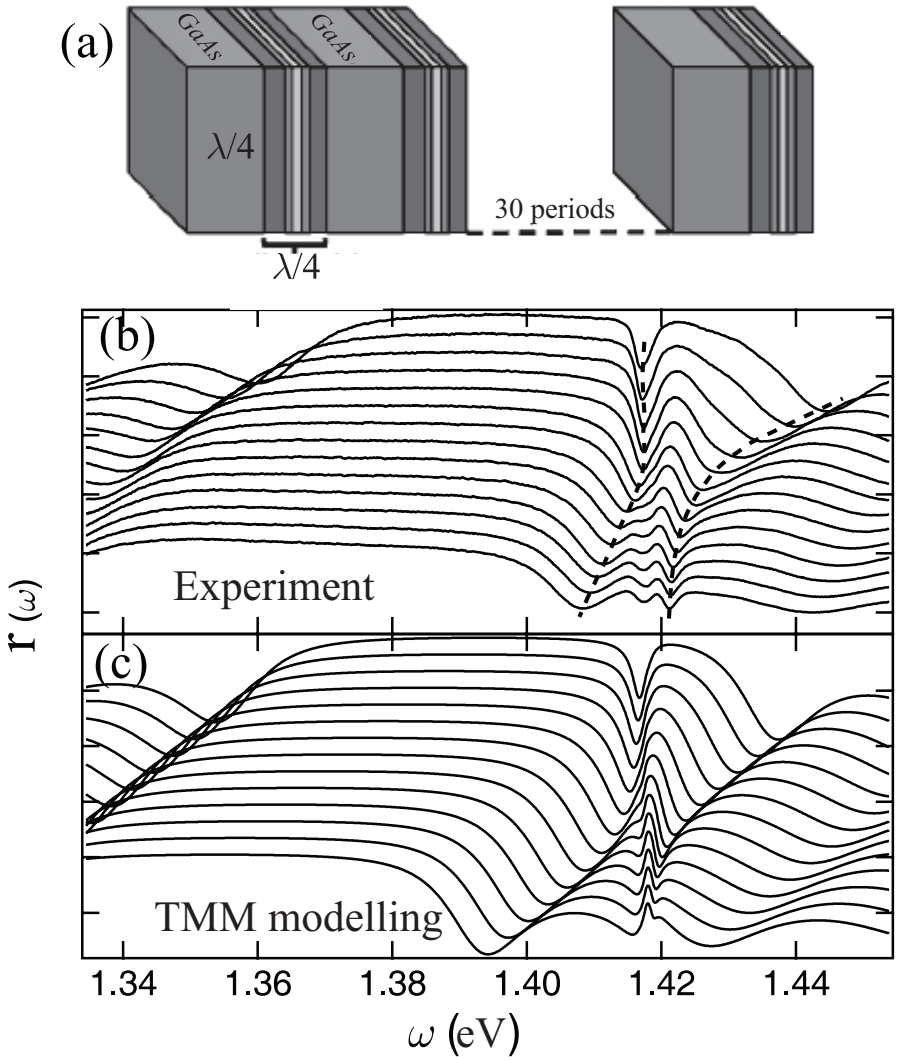

FIG. 3.5: (a) Geometry of the structure under consideration. (b) Experimental reflection spectra. (c) Reflection spectra calculated with transfer matrix method.

to the dispersion. The terms enclosed in the last parentheses correspond to the exciton contribution to the dispersion. For the analysis it is convenient to rewrite equation (3.66) in two equivalent forms:

$$\sin^2\left(\frac{KD}{2}\right) = \frac{(n_1+n_2)^2}{4n_1n_2}\sin\phi\left(\sin\phi - \frac{\Gamma_0}{\omega_X-\omega}\left(\cos\phi - \frac{n_1-n_2}{n_1+n_2}\right)\right), \tag{3.67}$$

$$\cos^2\left(\frac{KD}{2}\right) = \frac{(n_1+n_2)^2}{4n_1n_2}\cos\phi\left(\cos\phi + \frac{\Gamma_0}{\omega_X-\omega}\sin\phi\right). \tag{3.68}$$

Equation (3.67) is convenient to obtain the mode frequencies of the band edge corresponding to $K = 0$, and Eq.(3.68) for the frequencies of the band edge, corresponding to $K = \pi/D$. We can then expand the sine and cosine functions for frequencies close

to the stop band centre and obtain expressions for the band edges in closed form. The details can be found in [54].

Here we describe an alternative way to obtain the expressions for the eigenmode frequencies in a closed form, which also has the advantage of illustrating the mechanism of formation of the spectral triplet structure seen in figure 3.5. The formalism is mainly based on the model presented in [55] for the bulk excitons in photonic crystals.

We first write down the energy density of the electromagnetic field in the photonic crystal as

$$\mathcal{E}_{ph} = \frac{1}{2}\int d\mathrm{r}\left[\varepsilon(z)\mathrm{E}^2 + \mathrm{H}^2\right]. \tag{3.69}$$

The dielectric permittivity $\varepsilon(z)$ is a periodic function of z:

$$\begin{aligned} \varepsilon(a) &= \tilde{\varepsilon} + \delta\varepsilon F(z), \\ F(z+D) &= F(z), \end{aligned} \tag{3.70}$$

where $\tilde{\varepsilon}$ is the average dielectric permittivity and the periodic function $F(z)$ has unit amplitude. If the amplitude of the dielectric permittivity modulation is relatively weak, that is $\delta\varepsilon/\tilde{\varepsilon} \ll 1$, then we can make an approximation of only considering the first Fourier component of the periodic function F: $F = \cos(Gz + \varphi_0)$, where $G = 2\pi/D$ is the smallest reciprocal lattice vector, and φ_0 is a modulation phase, which is zero for a suitable choice of the coordinate system. The Fourier components of ε couple the terms with k and $k \pm G$ and if we consider only the frequencies close to the first Bragg resonance at $k \approx G/2 = \pi/D$, we can need only consider the first diffraction order $G - k \approx G/2$. Then the full photon Hamiltonian may be written as:

$$\begin{aligned} \mathcal{H}_{ph} = &\sum_q \left[\omega(q)\hat{a}^+_{\rightarrow}(q)\hat{a}_{\rightarrow}(q) + \omega(-q)\hat{a}^+_{\leftarrow}(-q)\hat{a}_{\leftarrow}(-q)\right] + \\ &+ \Omega_B\left[\hat{a}^+_{\rightarrow}(q)\hat{a}_{\leftarrow}(-q) + \hat{a}^+_{\leftarrow}(-q)\hat{a}_{\rightarrow}(q)\right]. \end{aligned} \tag{3.71}$$

Here $q = k - G/2$, $\hat{a}_{\rightarrow}(q) = \hat{a}_k$, $\hat{a}_{\leftarrow}(q) = \hat{a}_{k-G}$, where $\hat{a}_k$ is a photon annihilation operator and Ω_B is the band gap half-width which can be estimated by photonic crystal theory to be: $\Omega_B \approx \omega_B(n_1 - n_2)/(n_1 + n_2)$. $\omega(q)$ can be written as $\omega(q) = \omega_B\,(1 + 2q/G)$.

The exciton kinetic energy and exciton-photon interaction Hamiltonians are

$$\begin{aligned} \mathcal{H}_X = &\omega_X \sum_k \hat{b}^+(k)\hat{b}(k) + \\ &+ \Omega_R \sum_k \left[\hat{b}^+(k)\hat{a}(k) + \hat{a}^+(k)\hat{b}(k)\right], \end{aligned} \tag{3.72}$$

where ω_X is the exciton frequency, $\hat{b}(k)$ and $\hat{b}^+(k)$ are respectively exciton annihilation and creation operators and Ω_R is half the Rabi splitting, which describes the coupling of the excitons with the electromagnetic field. We should note that in the case of a periodic array of quantum wells, and contrary to the case considered in [55], k is not a true wavevector for the exciton since the component of the wavevector perpendicular to the interface is not defined for the exciton in a quantum well, being a Bloch wavevector of the periodic quantum well array. We neglect the energy dispersion of the exciton due to its relatively large effective mass. In the case of the excitons with the wavevectors close to the photonic band gap, approximations similar to those used for $\mathcal{H}_{ph}$ can be employed to obtain the full system Hamiltonian:

$$\begin{aligned}\mathcal{H} = &\sum_q \left[\omega(q)\hat{a}^+_{\rightarrow}(q)\hat{a}_{\rightarrow}(q) + \omega(-q)\hat{a}^+_{\leftarrow}(-q)\hat{a}_{\leftarrow}(-q)\right] + \\ &+ \sum_q \Omega_b \left[\hat{a}^+_{\rightarrow}(q)\hat{a}_{\leftarrow}(-q) + \hat{a}^+_{\leftarrow}(-q)\hat{a}_{\rightarrow}(q)\right] + \omega_X \sum_q \left[\hat{b}^+_{\rightarrow}(q)\hat{b}_{\rightarrow}(q) + \hat{b}^+_{\leftarrow}(-q)\hat{b}_{\leftarrow}(-q)\right] + \\ &+ \Omega_R \sum_q \left[\hat{b}^+_{\rightarrow}(q)\hat{a}_{\rightarrow}(q) + \hat{a}^+_{\rightarrow}(q)\hat{b}_{\rightarrow}(q) + \hat{b}^+_{\leftarrow}(-q)\hat{a}_{\leftarrow}(-q) + \hat{a}^+_{\leftarrow}(-q)\hat{b}_{\leftarrow}(-q)\right].\end{aligned} \tag{3.73}$$

Intoducing the vector operator $\hat{v} = [\hat{a}_{\rightarrow}(q), \hat{a}_{\leftarrow}(-q), \hat{b}_{\rightarrow}(q), \hat{b}_{\leftarrow}(-q)]$, the full Hamiltonian can be written as: $\mathcal{H} = \hat{v}^+ \mathrm{H} \hat{v}$, where the H is the matrix:

$$\mathrm{H} = \begin{pmatrix} \omega(q) & \Omega_B & \Omega_R & 0 \\ \Omega_B & \omega(-q) & 0 & \Omega_R \\ \Omega_R & 0 & \omega_X & 0 \\ 0 & \Omega_R & 0 & \omega_X \end{pmatrix}. \tag{3.74}$$

The eigenvalues of H are the system eigenmode frequencies. But to obtain the eigenvalues it is convenient to simplify H first. We first change the basis from $\hat{v}$ to basis $\hat{v}' = [\hat{U}, \hat{L}, \hat{X}_s, \hat{X}_a]$, where $\hat{U}$ and $\hat{L}$ are the annihilation operators of the lower and upper Bloch modes, and $\hat{X}_s$ and $\hat{X}_a$ are the annihilation operators for symmetric and antisymmetric exciton modes. If $\hat{v}' = \mathrm{M}\hat{v}$, then:

$$\mathrm{M} = \begin{pmatrix} \frac{1}{\sqrt{1+(\omega(q)-\omega_U)^2/\Omega_B^2}} & -\frac{1}{\sqrt{1+\Omega_B^2/(\omega(q)-\omega_U)^2}} & 0 & 0 \\ \frac{1}{\sqrt{1+(\omega(q)-\omega_L)^2/\Omega_B^2}} & -\frac{1}{\sqrt{1+\Omega_B^2/(\omega(q)-\omega_L)^2}} & 0 & 0 \\ 0 & 0 & \frac{1}{\sqrt{2}} & \frac{1}{\sqrt{2}} \\ 0 & 0 & \frac{1}{\sqrt{2}} & -\frac{1}{\sqrt{2}} \end{pmatrix}, \tag{3.75}$$

where $\omega_{U,L}$ are the eigenfrequencies of the Bloch modes, given by:

$$\omega_{U,L} = \omega_B \left(1 \pm \sqrt{4\frac{q^2}{G^2} + \frac{\Omega_B^2}{\omega_B^2}}\right). \tag{3.76}$$

The Hamiltonian H′ in the new basis is $\mathrm{H}' = \mathrm{M}^{-1}\mathrm{HM}$ and is:

$$\mathrm{H}' = \begin{pmatrix} \omega_U & 0 & 0 & \sqrt{2}\Omega_R \\ 0 & \omega_L & \sqrt{2}\Omega_R & 0 \\ 0 & \sqrt{2}\omega_R & \omega_X & 0 \\ \Omega_R & 0 & 0 & \omega_X \end{pmatrix}. \tag{3.77}$$

Here we should recall that the exciton frequency in the experiment is close to the upper edge of the photonic band gap, and furthermore the Rabi frequency Ω_R is much smaller than the photonic band gap width Ω_B. As a result, the lower Bloch mode is remote in frequency from the other three modes and we can assume its dispersion is essentially unperturbed and that it does not perturb the other modes significantly. Excluding the column and row corresponding to $\hat{L}$ from the Hamiltonian gives:

$$\mathrm{H}' = \begin{pmatrix} \omega_U & 0 & \sqrt{2}\Omega_R \\ 0 & \omega_X & 0 \\ \sqrt{2}\Omega_R & 0 & \omega_X \end{pmatrix}, \tag{3.78}$$

and introducing $\delta = \omega_U - \omega_X$, we find the system eigenfrequencies to be

$$\omega_1 = \omega_X;\ \omega_{2,3} = \omega_X + \left(\delta \pm \sqrt{\delta^2 + 8\Omega_R^2}\right)/2. \tag{3.79}$$

In the case of a finite structure the Bloch vector K has a set of discrete values, which correspond to discrete values of ω_U and we should change ω_U to ω_{U1} in our analysis, where ω_{U1} is the frequency of the discrete Bloch mode closest to the upper band edge as illustrated in Fig.3.6).

Figure 3.7 shows a comparison of the experimental results with the predictions of the analytic model. It is seen that the analytic results for the mode frequencies as a function of the difference between the photonic band edge and the exciton energy generally agree well with the experimental data. The theory does not predict any dispersion of the middle branch $\omega_1 = \omega_X$ as a result of excluding the lower Bloch mode from the Hamiltonian. However, the experimental results confirmed that the dispersion is very weak.

In the experiment the exciton frequency was tuned to the low frequency edge of the second photonic band. However, it is also possible to tune the frequency to the high frequency edge. In this case the Bloch wavevector is close to zero, and we can introduce an effective mass for the Bloch mode, which will be negative close to the photonic band edge. We have carried out numerical modelling of this case using the same refractive indices as in the experiments and layers giving a Bragg frequency equal to 1 eV.

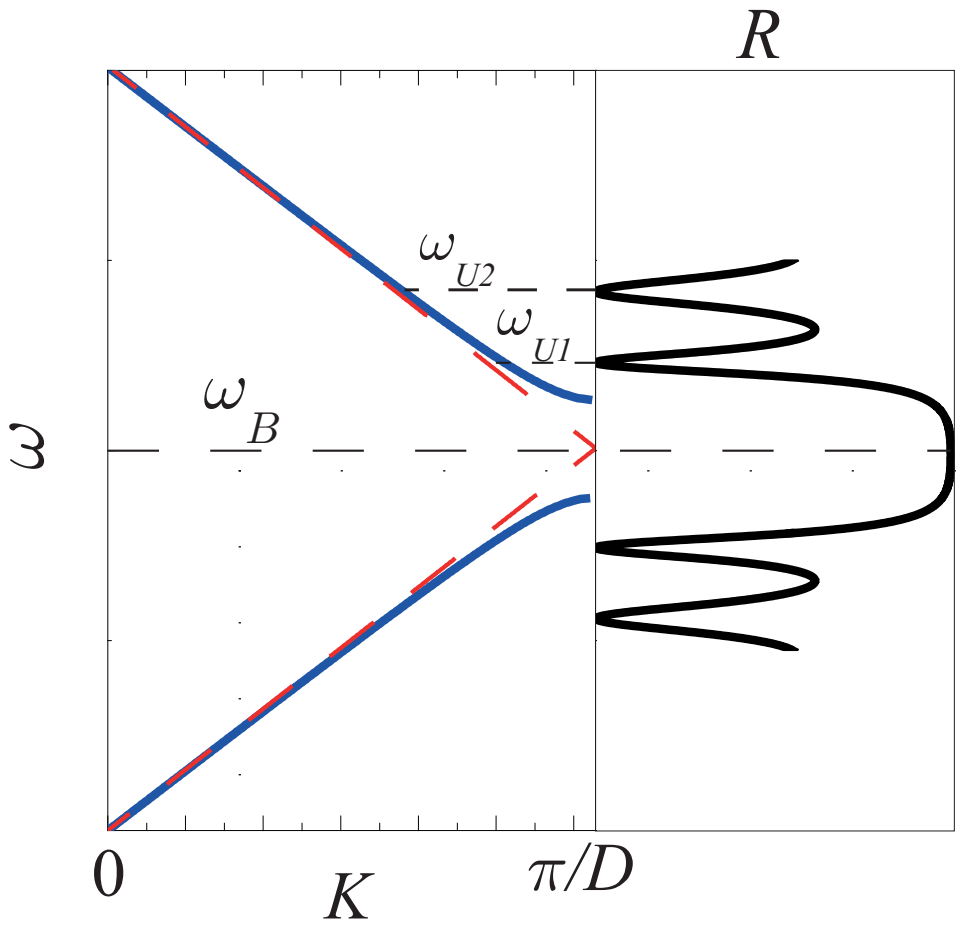

FIG. 3.6: Band structure of the photonic crystal without quantum wells. Red lines show the dispersions of the propagating photonic modes $\hat{a}_{\rightarrow}(q)$,$\hat{a}_{\leftarrow}(-q)$, black lines show the dispersions of the Bloch modes $\hat{U}$,$\hat{L}$. Right picture shows the reflection spectrum from the finite structure. Reflection coefficient minima correspond to discrete Bloch modes, which are characterized by frequencies ω_{U1}, ω_{U2}, etc.

The second band gap vanishes in a quarter-wavelength Bragg reflector, so the layer thicknesses and refractive indices have been chosen so that: $n_1 d_1 = (3/8)\lambda_B$; $n_2 d_2 = (1/8)\lambda_B$, where λ_B is a Bragg wavelength. Transfer matrix calculation results given in Fig.3.8 show that in the case of the exciton frequency being in resonance with the upper edge of the second band at 1.96 eV, two polaritonic states emerge, and one of those states is characterized by negative effective mass and group velocity in the direction perpendicular to the layers interfaces. Thus, the effective mass tensor for this mode has two positive and one negative components.

To conclude, in this section we have demonstrated a simplified analytical model, which illustrates the mechanism of triplet structure formation in the reflection spectra. It has been shown that the eigenfrequencies measured experimentally agree well with the predictions of the analytical model. It has also been demonstrated that the strong coupling

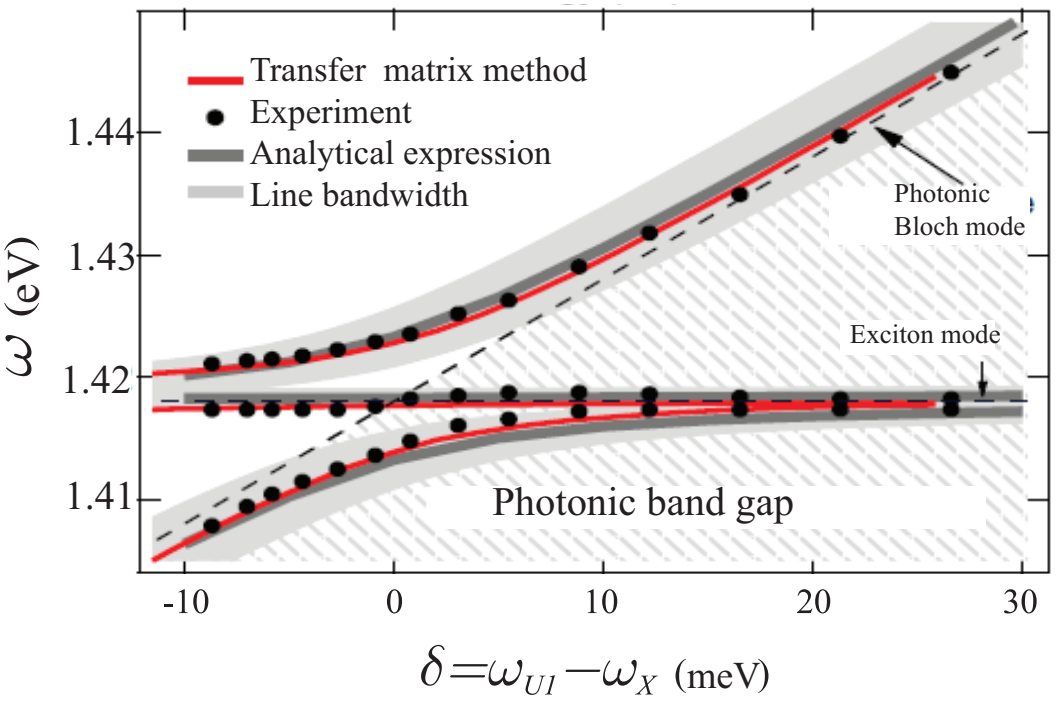

FIG. 3.7: Dependence of the system eigenfrequencies on the detuning between the exciton energy and photonic band edge, obtained from experiment, transfer matrix method and with the analytical model.

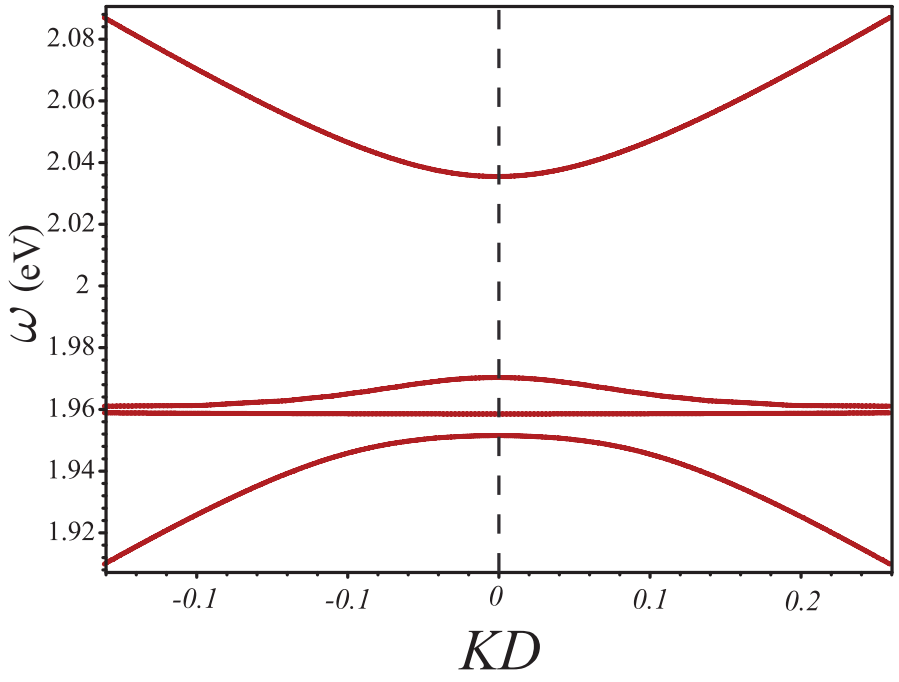

FIG. 3.8: Eigenmode dispersion in the case of tuning of the exciton mode to the upper edge of the second photonic band. Exciton frequency - 1.96 eV. Refractive indices of the layers $n_1 = 3.5$, $n_2 = 3.2$, and thicknesses of the layers $d_1 = 133$ nm, $d_2 = 43$ nm.

of the photonic crystal eigenmodes and excitons can lead under some circumstances to the formation of polaritonic modes characterized with negative effective mass and group velocity.

3.4 Parametric amplification by a periodic array of quantum wells embedded in layers of a one-dimensional photonic crystal.

3.4.1 Parametric amplification of exciton-polaritons

The eigenmodes of the system, discussed in section 3.3 are mixed exciton-photon modes - exciton-polaritons. Here we consider the phenomenon of parametric amplification of exciton-polaritons which occurs due to the scattering of exciton-polaritons and is one of the two main nonlinear effects occurring in the polaritonic systems the other being a blue shift of the ground polaritonic state [48]. The mechanism of the parametric amplification can be understood by looking at the lower polariton dispersion curve shown in Fig.3.9. The non-parabolicity of the ground polaritonic branch leads to the existence of a so-

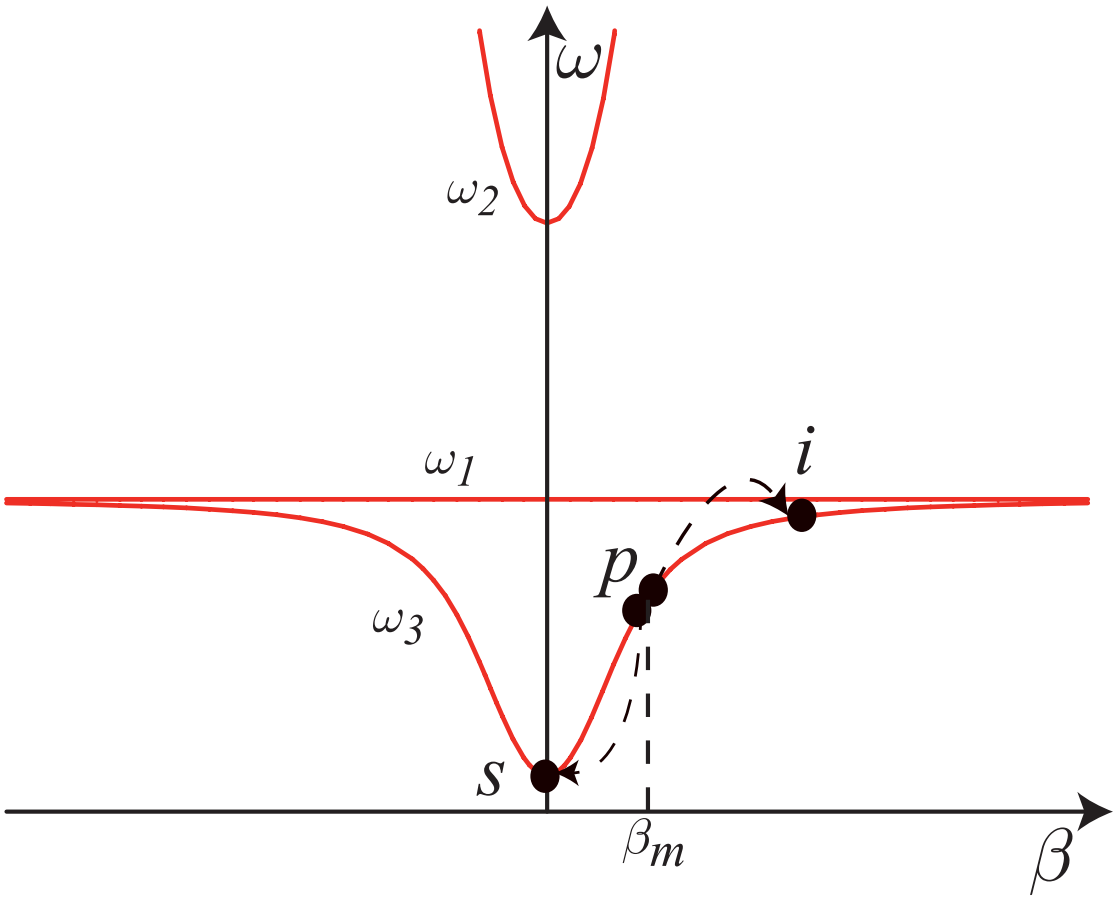

FIG. 3.9: Dispersion of the exciton-polariton. Arrows show how the two pump polaritons p scatter elastically into a ground state s and an idler state i.

called magic wavevector β_m, where two polaritons with such a wavevector can scatter elastically, with one scattering into the ground state and the other into the state with

wavevector $2\beta_m$. Thus, if we pump such a system resonantly at the magic wavevector and frequency, it is possible to observe a strong luminescence enhancement from the ground state. Studies of polariton-polariton scattering features, which lead to the parametric amplification have been reported in a number of theoretical and experimental papers - see for example [56, 57].

A series of pump probe experiments have been performed by the Cambridge group with the sample discussed in section 3.3, which have revealed parametric amplification occurring in the structure. The main experimental results have been presented in [47]. We have been able to show by numerical simulation of these results, that the theory of parametric amplification in conventional microcavity [48] can be successfully applied to the case of a periodic quantum well array.

3.4.2 Experimental measurements and results

In the experiments, which were performed by the Cambridge group, the system was pumped with pulses of 1ps length and 3.5 meV linewidth, at an angle of incidence corresponding to the magic wavevector. A broadband 150 fs probe pulse was incident normal to the interface of the structure and time-dependent reflection spectrum were measured. The violet line in Fig. 3.10(a) shows the reflection spectra in the absence of a pump pulse including dips at the frequencies corresponding to the three polaritonic modes, which were studied in section 3.3.

If a pump pulse is applied with zero delay time relative to the probe pulse, the reflection spectrum changes dramatically, and there is a peak in the reflection spectrum at a frequency which is 3 meV higher than the ground polaritonic state. The peak height corresponds to the enhancement of the probe pulse by a factor of 6.4 (see Fig. 3.10(c)). The time dependence of the normalized reflection spectra in Fig.3.10(b) indicates a nonlinear response with a response time of about 1.8 ps, which is close to the values typically obtained for the microcavity polaritons [58]. However, the polariton lifetime in this system is less than for conventional microcavity polaritons resulting in a wider band of polaritonic states and thus a wider enhancement peak (about 2.5 meV).

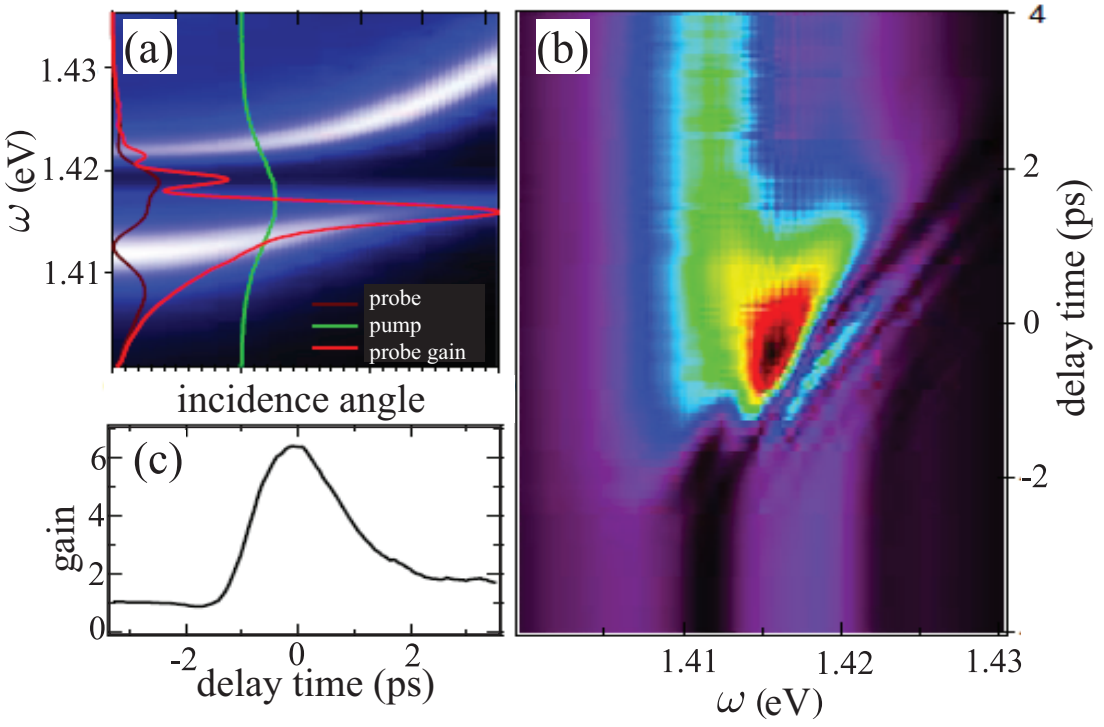

FIG. 3.10: An illustration of parametric amplification. (a) Reflection spectrum in the case of a single probe pulse (violet line). The green line corresponds to a 50 mW pump pulse, which is tuned to the ground polaritonic branch with wavevector equal to the magic wavevector (corresponding to an incidence angle 20 degrees). In this case there is strong amplification of a probe pulse (red line). (b) Colour map showing the dependence of the reflection on the frequency and delay time. (c) Dependence of the probe pulse enhancement on the delay time.

3.4.3 Three-level model of parametric amplification

It has been shown in [48], that the process of parametric scattering of two polaritons p into the signal s and idler modes i is described by the Hamiltonian,

$$H = \hbar\omega_p \hat{a}_p^+ \hat{a}_p + \hbar\omega_s \hat{a}_s^+ \hat{a}_s + \hbar\omega_i \hat{a}_i^+ \hat{a}_i + \hbar M \left(\hat{a}_p \hat{a}_p \hat{a}_s^+ \hat{a}_i^+ + \hat{a}_s \hat{a}_i \hat{a}_p^+ \hat{a}_p^+\right) + \tag{3.80}$$
$$+ \hbar U \left(|X_s|^2 \hat{a}_s^+ \hat{a}_s + |X_p|^2 \hat{a}_p^+ \hat{a}_p + |X_i|^2 \hat{a}_i^+ \hat{a}_i\right) \left(|X_s|^2 \hat{a}_s^+ \hat{a}_s + |X_p|^2 \hat{a}_p^+ \hat{a}_p + |X_i|^2 \hat{a}_i^+ \hat{a}_i\right),$$

where $\omega_s, \omega_i, \omega_p$ are the frequencies of the signal, idle and pump modes respectively, $\hat{a}$ are the annihilation operators, and X_α are the Hopfield coefficients [59], which define the excitonic part of a polaritonic state α. The first three terms correspond to the kinetic energy of the polaritons in the three state, the fourth term defines the energy of the parametric processes, M being the matrix element of these processes, and the last term, proportional to U, corresponds to the blue-shift of exciton polaritons caused by the exciton-exciton interaction. In what follows we will neglect the last term to simplify the formalism, taking advantage of the fact that the effect of blue shift was weak in the

experiment. Reference [60] gives the following expression for M

$$M \approx \frac{12\pi}{\hbar}\frac{a_B^2}{S}E_b^2|X_s|^2|X_i|^2|X_p|^4, \tag{3.81}$$

where a_B is an exciton effective Bohr radius, S is the sample area, and E_b is the exciton binding energy.

To derive the equations for the dynamics of the occupation numbers of the three states considered we first introduce the density matrix of ρ the system:

$$\rho = \sum_{j=s,i,p} w_j|\psi_j\rangle\langle\psi_j|, \tag{3.82}$$

where ψ_j is the eigenfunction of each state, and w_j is the probability of the polariton to be in one of the states. The density operator obeys the Liouville-von Neumann equation:

$$i\hbar\frac{d\rho}{dt} = [H, \rho]. \tag{3.83}$$

The expectation value $\langle\hat{N}_j\rangle$ of the number operator $\hat{N}_j = \hat{a}_j^+\hat{a}_j$ can be obtained as a trace over the density matrix:

$$N_j = \mathrm{Tr}(\hat{a}_j^+\hat{a}_j\rho). \tag{3.84}$$

To show this, it is instructive to recall that for an operator $\hat{A}$ in a finite-dimensional vector space with an orthonormal basis set $|j\rangle$ the trace of operator $\hat{A}$ is defined as

$$\mathrm{Tr}(\hat{A}) = \sum_{j=1}^{j=n}\langle j|\hat{A}|j\rangle = A_{jj}, \tag{3.85}$$

where the summation is performed over the repeated index. We can then expand $\mathrm{Tr}(\rho\hat{A})$ using equations (3.82) and (3.85) as:

$$\begin{aligned}\mathrm{Tr}(\rho\hat{A}) = \sum_j\sum_k w_k\langle j|\psi_k\rangle\langle\psi_k|\hat{A}|j\rangle = \sum_j\sum_k w_k\langle\psi_k|\hat{A}|j\rangle\langle j|\psi_k\rangle = \\ = \sum_k w_k\langle\psi_k|\hat{A}|\psi_k\rangle,\end{aligned} \tag{3.86}$$

since $\sum|j\rangle\langle j|$ is an identity matrix. Therefore we can can write down the equation for the expectation value of the occupation number of state k in the form:

$$\frac{dN_k}{dt} = -\frac{i}{\hbar}\mathrm{Tr}(\hat{a}_k^+\hat{a}_k[H, \rho]). \tag{3.87}$$

Using the commutation rules for the operators we obtain:

$$\frac{dN_s}{dt} = 2\mathrm{Im}[M\mathrm{Tr}(\hat{a}_s^+\hat{a}_i^+\hat{a}_p\hat{a}_p)\rho], \tag{3.88}$$

$$\frac{dN_i}{dt} = 2\mathrm{Im}[M\mathrm{Tr}(\hat{a}_s^+\hat{a}_i^+\hat{a}_p\hat{a}_p)\rho], \tag{3.89}$$

$$\frac{dN_p}{dt} = -4\hbar\mathrm{Im}[M\mathrm{Tr}(\hat{a}_s^+\hat{a}_i^+\hat{a}_p\hat{a}_p)\rho]. \tag{3.90}$$

The operator $\hat{a}_s^+\hat{a}_i^+\hat{a}_p\hat{a}_p = \hat{C}$ is a fourth-order correlator denoting the correlations between different states, in the classical limit, this correlator is equal to zero since no correlations are accounted for. To derive the dynamics of this correlator we use the same approach taking the appropriate trace:

$$\frac{d\langle\hat{C}\rangle}{dt} = -\frac{i}{\hbar}\mathrm{Tr}(\hat{a}_s^+\hat{a}_i^+\hat{a}_p\hat{a}_p[H,\rho]) = iM\left(N_p^2(N_s+N_i+1) - 4N_sN_i(N_p+1)\right). \tag{3.91}$$

We should also add phenomenological terms corresponding to the polariton decay, $N_{s,i,p}/\tau_{s,i,p}$ where the $\tau_{s,i,p}$ are the polariton decay times in the respective states:

$$\tau_\alpha = \left(\frac{|X_\alpha|^2}{\tau_X} + \frac{|C_\alpha|^2}{\tau_c}\right)^{-1}, \tag{3.92}$$

where τ_c, τ_X - are the photonic and excitonic decay times. The Hopfield coefficients for the states X_α, C_α are the components of the normalized eigenvectors of the matrix (3.78), corresponding to the lower polariton branch. The photon lifetime is the inverse imaginary part of the eigenfrequency of the system in the absence of excitons and can be calculated by the transfer matrix method. The approximate values of the excitonic lifetime are known from the experiment and are about 1 ns [61].

We should also add the terms corresponding to the pump. In the experiment, there are two pumping mechanisms: resonant pumping to the pump state and nonresonant pumping with a probe pulse, which pumps all the three states. Therefore, We introduce three different pumping terms $P_p(t), P_s(t), P_i(t)$ corresponding to the time-dependent pump rates in each of the states. Furthermore, initial conditions should be imposed. Here we choose for these to be an initial absence of polaritons. As a result we get a

system of four first-order nonlinear differential equations with zero initial conditions:

$$\begin{aligned}
&\dot{N}_p = -\mathrm{Im}(MC) - N_p/\tau_p + P_p(t), \\
&\dot{N}_s = 2\mathrm{Im}(MC) - N_s/\tau_s + P_s(t), \\
&\dot{N}_i = 2\mathrm{Im}(MC) - N_i/\tau_i + P_i(t), \\
&\dot{C} = iM\left(N_p^2(N_s + N_i + 1) - 4N_sN_i(N_p + 1)\right) - \left(\frac{1}{2\tau_s} + \frac{1}{2\tau_i} + \frac{1}{\tau_p}\right)C, \\
&S|_{t=0} = n_s|_{t=0} = n_p|_{t=0} = n_i|_{t=0} = 0.
\end{aligned} \tag{3.93}$$

Some Numerical modelling results are shown in Fig.3.11. Figure 3.11(a) shows the evolution of the occupancy numbers for the pump and signal states in the case when the both pulses arrive at the same time. We can see that the nonlinear response time δt is about 0.75 ps, which agrees well with the experimental result (1.5 ps, see Fig.3.10(b)). Figure 3.11(b) shows a plot of maximum amplification versus the pump-probe delay time. We observe that the maximum amplification is 10 which is fifty percent larger than the experimentally observed value (see Fig.3.10(c)).

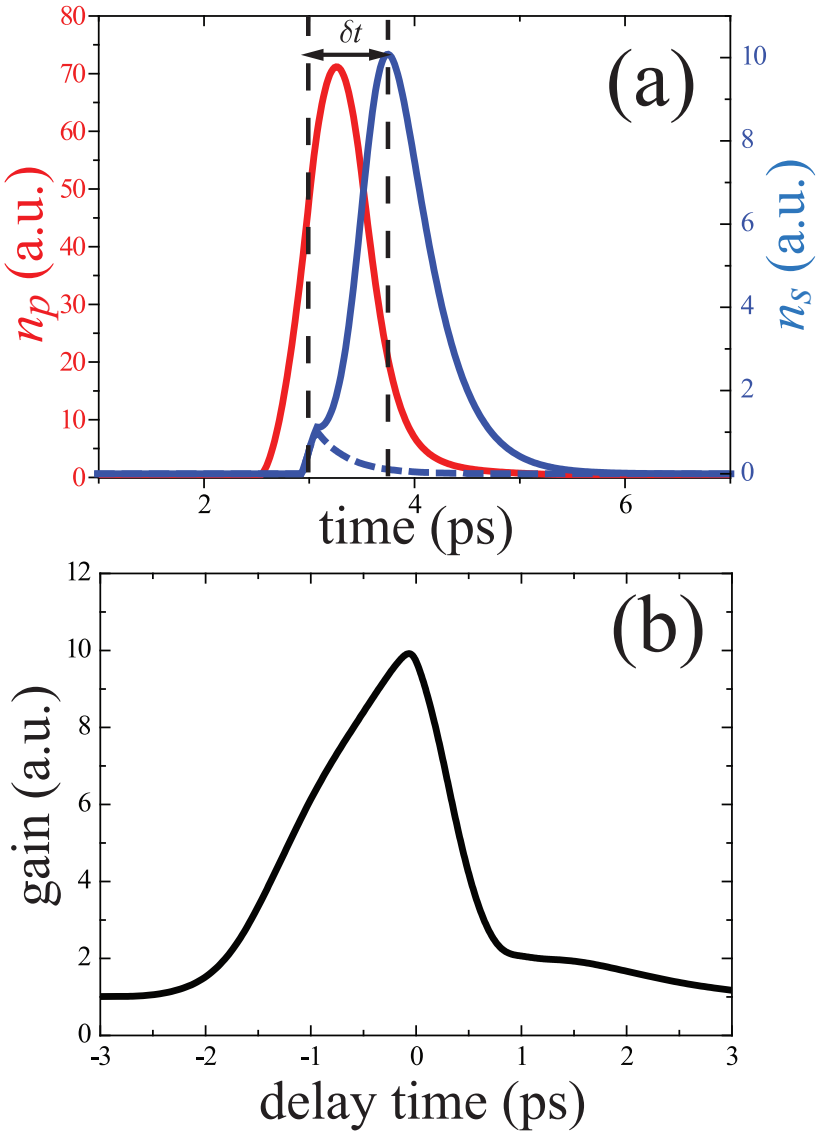

FIG. 3.11: Numerical modelling of the experiment, performed by the Cambridge group, with the sample considered in section 3.3 demonstrating parametric amplification in the system. (a) Time dependence of the pump state (red line) and signal state (blue line) occupancies in the case when the pump and probe pulse arrive at the same time $t = 3$ ps. Blue dashed line shows the evolution of the signal state in the absence of the pump pulse. All the values are normalized to the maximum occupancy of the signal state in the absence of a pump pulse. δt shows the nonlinear response time of the system. (b) Dependence of the probe pulse amplification on the pump-probe delay time.

3.5 Brief summary

We have obtained following main results in this chapter:

- We have derived analytical expressions for the optical properties of a system consisting of adjacent metal and organic layers in a microcavity. It has been demonstrated that sharp spectral features occur in the reflectivity specta of the structure

due to the strong coupling of Tamm plasmon polariton states at each of the metal interfaces.

- We have developed a simplified theory of the interaction of a periodic array of quantum well excitons with photonic crystal optical eigenmodes. We have calculated theoretical reflection spectra for these structures which agree well with the experimental data. We have also predicted a new type of polaritonic mode.

- We have shown that Bragg polaritons can be characterized by negative group velocity and effective mass in the case when the exciton frequency is tuned to the upper edge of the second photonic band.

- We have performed modelling of the parametric amplification of these polaritons within a three level formalism. The values of the nonlinear response time and maximum signal amplification obtained agree well with the experimental results.

Chapter 4

Kinetics of exciton-polariton condensates and the modelling of polariton lasers

4.1 Introduction

This chapter describes work on modelling of the kinetic processes in polariton laser diodes [62], which was motivated by and performed in collaboration with an experimental group from the École Politechnique Fédérale de Lausanne (EPFL). The work covered the modelling of both the steady state properties of polariton lasing, including the temperature and detuning dependence of the lasing threshold, and the small signal response of certain polariton laser diodes, where the device transfer function has been calculated[1].

The chapter is organized as follows. In the first section the basic concepts of polariton condensation and polariton lasing are discussed and a brief historical overview of the field is presented. The next section is dedicated to a discussion of possible designs of the polariton laser diode and is largely based on the original ideas of our experimental collaborators. The third section describes the kinetic processes occurring in the laser and presents the semi-classical Boltzmann equations formalism which is the basis of the modelling carried out. That is followed by a presentation and discussion of the numerical results obtained from the modelling. A brief summary of the chapter is presented in the last section.

[1] My contribution to the work involved developing and performing the modelling based on semi-classical Boltzmann equations using parameters provided by our experimental collaborators. The presentation of the work closely follows reference [62], for which I was first author.

4.2 Background theory

4.2.1 Bose-Einstein condensation of exciton-polaritons

Consider N non-interacting bosons in a system of linear dimensions L and volume L^d, where d is the dimensionality of the system. If the system is in thermal equilibrium at temperature T, the bosons are distributed in energy according to a Bose-Einstein distribution:

$$f(\mathbf{k}, T, \mu) = \frac{1}{\exp\left[\frac{E(\mathbf{k})-\mu}{k_B T}\right] - 1}, \tag{4.1}$$

where $\mathbf{k}$ is the boson wavevector, $E(\mathbf{k})$ is the energy of state $\mathbf{k}$, and k_B is the Boltzmann constant. In what follows we assume that the ground state $\mathbf{k} = 0$ corresponds to the zero energy. μ is a chemical potential, which denotes the energy needed to add a particle to the system, and for bosons is always less than or equal to zero. The total number of the particles in the system can be written as

$$N(T, \mu) = \sum_{\mathbf{k}} f(\mathbf{k}, T, \mu). \tag{4.2}$$

To proceed it is instructive to split the above sum into the number of particles in the ground state $\mathbf{k} = 0$ and in all the excited states:

$$N(T, \mu) = \frac{1}{\exp\left[-\mu/k_B T\right] - 1} + \sum_{\mathbf{k}\neq 0} f(\mathbf{k}, T, \mu). \tag{4.3}$$

Moving to the thermodynamic limit,(increasing the number of the particles and the system size indefinitely in such a way, that the density of the particles $n = N/L^d$ remains constant) the particles density is:

$$n(T, \mu) = \lim_{L\to+\infty} \frac{1}{L^d} \frac{1}{\exp\left[-\mu/k_B T\right] - 1} + \frac{1}{(2\pi)^d} \int_0^\infty f(\mathbf{k}, T, \mu) d\mathbf{k}. \tag{4.4}$$

If μ is nonzero, then the first term vanishes. On the other hand, the second term, which denotes the density of bosons in the excited states, is an increasing function of μ, and we can define the maximum possible density of bosons in the excited states n_c as:

$$n_c(T) = \lim_{\mu\to 0} \frac{1}{(2\pi)^d} \int_0^\infty f(\mathbf{k}, T, \mu) d\mathbf{k}. \tag{4.5}$$

If this integral converges, it means that there exists a maximum density of bosons n_c that can be accommodated in the excited states and if the total density n is larger than n_c then μ is zero and there is a density $n_0 = n - n_c$ in the ground state resulting in a macroscopic occupation of a single quantum state.

It has been shown that the integral (4.5) converges for $d > 2$. For the case of three dimensional system and parabolic dispersion the integral can be evaluated analytically as:

$$n_c = \frac{1}{\sqrt{2\pi}}\zeta\left(\frac{3}{2}\right)\left(\frac{mk_BT}{\hbar^2}\right)^{3/2}, \tag{4.6}$$

where $\zeta(x)$ is the Riemann zeta function. Note, that the critical concentration of the particles is proportional to $(mT)^{3/2}$, and thus increases with temperature and boson mass. Let us consider the fixed total concentration of bosons n and consider the system in thermal equilibrium at temperature T. If for this temperature the critical concentration n_c given by (4.6) is larger than n, there is no condensation in the system. If we start to decrease the temperature adiabatically, at some finite temperature T_c, n_c becomes equal to n. For temperatures lower then T_c, the macroscopic occupation of the ground state would be observed. T_c is called the Bose-condensation temperature, and is inversely proportional to the boson mass.

The first clear experimental verification of Bose condensation in a weekly interacting system was achieved by Anderson et al. in 1995 using a very dilute gas of alkali atoms at a temperature of hundreds nanokelvin and was rewarded by the Nobel Prize for Physics in 2001.

There are some specific features about the condensation of exciton-polaritons to consider. The first is the fact that the exciton-polaritons are 2-dimensional particles, and the integral for n_c in equation (4.6) does not converge for $n = 2$, suggesting that there can be no thermodynamic Bose condensation. However, this restriction can be overcome if we recall that the polariton condensation usually takes place in a finite area and that the polaritons have finite lifetime. It means, that there can be no thermodynamic equilibrium for the polaritonic system. Another issue is that the exciton is actually a composite particle, an electron-hole pair, which can be considered as a boson only in the low-density regime. It is easy to estimate an upper limit for the concentration for which the approximation of a boson gas is valid. It is required that the average distance between the excitons a in the gas is much larger then the exciton Bohr radius a_B:

$$a \approx n^{-1/2} \gg a_B. \tag{4.7}$$

The corresponding condition for the exciton concentration n is $n \ll 1/(a_B)^2$. The condition for the exciton-polaritons can be written down as: $\sum n_k |X|_k^2 \ll 1/(a_B)^2$, where n_k is the concentration of polaritons in state k and X_k is the Hopfield coefficient showing the exciton fraction in the polariton state k.

Another important feature of the polariton condensation is the very high temperatures at which the condensation can take place which is due to the very small effective mass of polaritons close to the ground state. This property makes possible the observation of Bose-condensation and related phenomena in semiconductor systems at relatively high temperatures and even up to room temperature in certain systems. As a consequence, the physics of polariton condensates has become one of the most rapidly expanding and exciting fields of condensed matter physics. The observation of the Bose-condensation of polaritons occurring in CdTe-based planar microcavities at cryogenic temperatures was first reported in [63] and triggered the further research on the phenomenon. Bose-condensation was later reported at room temperature in wide bandgap organic and inorganic semiconductors which exhibit highly stable excitons [64–66]. Some of the exotic phenomena occurring in polariton condensates include hints of superfluidity such as integer and half-quantized vortices [67, 68] and the ballistic motion of condensates [69, 70]; and also spontaneous coherent oscillations between adjacent condensates that share similarities with the ac Josephson effect [71].

4.2.2 Polariton lasing

Our work has been dedicated to the study of one of the most attractive of polariton condensation phenomena with regard to potential applications - namely polariton lasing [9]. A schematic diagram of the polariton laser is shown in fig.4.1(a). To understand the basic concept of polariton lasing, consider a polaritonic system which is being continuously pumped nonresonantly, as shown in fig.4.1(b), creating polaritons in high k states. Polaritons then either relax into the ground state or decay either radiatively or non-radiatively. If we assume that all the polaritons excited have infinite lifetime, then according to the theory presented previously, after some certain density of the excited states is reached, all other polaritons would fall into the ground state, where they would decay radiatively producing coherent emission of light (laser-like light) from the microcavity. This coherent emission needs no carrier population inversion since the emission is spontaneous, not stimulated, and therefore should have a significantly lower threshold pumping requirement than in a conventional laser. In reality polaritons have a finite lifetime and it is essential that the relaxation time of the excited polaritons to the ground state is less then the polariton lifetime. However, due to the bosonic nature

of the polaritons, the relaxation rates are proportional to both the initial state occupation and the final state occupation, the condition on the relaxation time is equivalent to the condition of the critical polariton density in the system, and thus to a fixed finite threshold pump power.

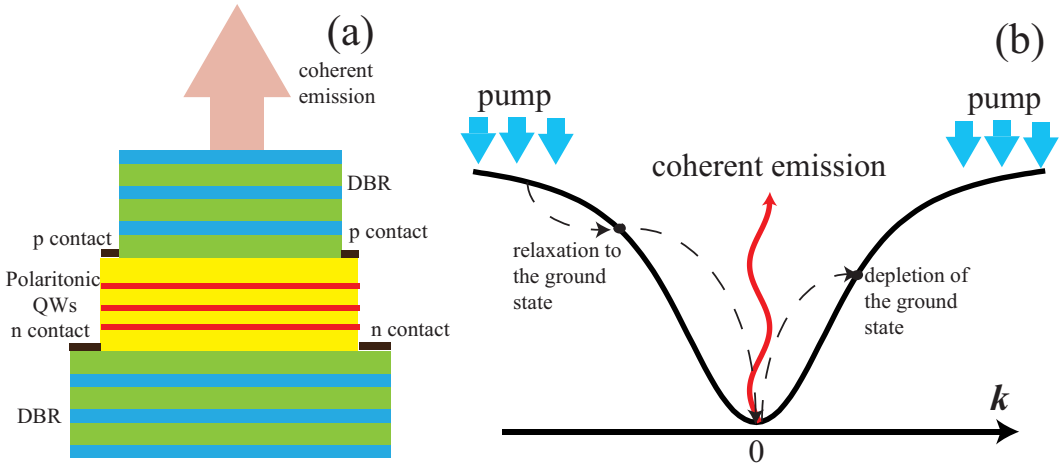

FIG. 4.1: (a) Schematic diagram of a polariton laser. (b) Schematic illustration of the kinetic processes in the system: pump to the excited states, relaxation to and from the ground state, and coherent emission from the ground state due to the finite polariton lifetime.

Electrically pumped polariton light emitting diodes (LEDs) have been reported in [72] to operate in a wide range between cryogenic and room temperatures. These structures, obviously operating in the strong coupling regime (SCR), have a design relatively close to that of their near-infrared vertical cavity surface emitting laser (VCSEL) counterparts (which are based on the same material system) operating in the weak coupling regime. However, the realization of room-temperature (RT) GaAs-based polariton laser diodes (LDs) is probably precluded by the value of the exciton binding energy (E_X^B) in this material system (usually less than 10 meV for the quantum wells (QWs) of interest) [73], which is small compared to the thermal energy at 300 K. Indeed, it has been previously shown that the value of E_X^B is the main limiting factor for the high-temperature observation of optical nonlinearities of polaritonic origin under resonant excitation [74]. In the search of the material systems defined by the larger values of the exciton binding energy, a strong interested has been directed to the III-nitride compounds [75], which have a number of advantages compared to the other wide bandgap semiconductor systems such as organic compounds or ZnO. It is suggested that III-nitride systems could have threshold current densities (J_{thr}) as low as $\sim 10\,\mathrm{Acm}^{-2}$ at room temperature, which is two orders of magnitude less than state of the art GaN based edge-emitting diodes. The reason for such a low threshold is because that the condensation process is expected to occur at medium polariton densities - lower then those causing significant screening and phase space filling effects that would lead to the transition of polaritons

and excitons toward an electron-hole plasma - because of the low effective density of states of polaritons resulting from their very light mass near the center of the Brillouin zone.

4.3 Designs of the polariton lasers considered

To begin, it is useful to consider some aspects of III-nitride structures relevant to the implementation of an electrical injection scheme suitable for polariton LDs [75] [2]. A recent theoretical study of the characteristics of a bulk GaN polariton light emitting diode LDs predicted a J_{thr} value of $\sim 50\,\mathrm{Acm}^{-2}$ at room temperature (RT), thereby indicating the potential of such devices as low-threshold coherent light emitters [76]. Although such a structure has the advantage of simplicity it should be noted that a realistic design for RT operation will most likely rely on a multiple QW (MQW) active region because of the improved carrier confinement and the higher exciton binding energy over bulk in such two-dimensional heterostructures.

The number of quantum wells (N_{QW}) should be large enough to achieve a well defined strong coupling regime signature at room temperature i.e. to get a sufficiently large Rabi splitting (Ω_{VRS}) to polariton linewidth ratio [77]. The latter is due to the detrimental impact of the inhomogeneous linewidth broadening of III-nitride QWs, which can blur the signature of polaritons if it is too large for a small N_{QW} value (note also that the homogeneous broadening is usually non-negligible at 300 K) [78]. To get efficient electrical injection, the most appropriate choice of active region would be obtained by switching from the usual GaN/AlGaN MQW system to InGaN/GaN MQWs [65, 79] since good p-type conductivity becomes progressively more difficult to obtain when increasing the Al content of the AlGaN layers due to the significant rise of the activation energy of the deep Mg acceptor level [80]. At first sight, InGaN/GaN MQWs might seem an unpromising choice to achieve strong coupling because of their large inhomogeneous QW linewidth. But low indium content ($7\% < x < 10\%$) $\mathrm{In}_x\mathrm{Ga}_{1-x}\mathrm{N}$/GaN MQW microcavity structures with a design close to that of GaN/AlGaN MQW microcavity samples [65, 77] are expected to exhibit clear strong coupling features and polariton lasing under optical pumping at RT. Such an approach is also motivated by the recent development of crack-free, lattice-matched AlInN/GaN distributed Bragg reflectors (DBRs) grown on freestanding GaN substrates that combine low dislocation density ($\leq 10^6\ \mathrm{cm}^{-2}$), smooth rms surface roughness (~ 0.26 nm for a $4 \times 4\ \mu\mathrm{m}^2$ area) and high peak reflectivity ($R \sim$

[2] like much of this chapter the presentation in this subsection closely follows reference [62], of which I am first author. However, the discussion in this subsection is mainly based on work carried out largely by the authors of [62] at EPFL and is very similar to work previously published by them in [75]. It does, however, provide important practical background information to theory provided here and is included for that purpose.

99.6 %) [81]. Microcavity structures grown on such a DBR would certainly exhibit a much improved optical quality, i.e., a reduced in-plane cavity disorder compared with similar structures grown on *c*-plane sapphire substrates [82].

With such microcavity samples, another matter to be addressed is the achievement of a uniform injection of electrons and holes into the active region, which is known to be an issue in III-nitride optoelectronic devices [83]. A way to circumvent the conflicting requirements presented by a structure where N_{QW} should be large for the realization of strong coupling and small for electrical injection would be to use an intracavity pumping geometry as illustrated in Fig.4.2 [84]. Within such a pumping scheme, a small number of QWs (QWs-1) sandwiched in the intrinsic region of a *p-i-n* diode would be electrically pumped. Polaritons would not be formed in these QWs but they would emit photons at an energy greater than the absorption edge of a MQW region (second QW subset, QWs-2) located underneath, which would be in the strong coupling regime when pumped by the emission from QWs-1. Other specific constraints regarding the design of polariton LDs have been described in Ref. [75] and are included in the three-dimensional (3D) cross-section of the InGaN/GaN MQW polariton LD displayed in Fig.4.2 An intracavity contact scheme is used, as described in the case of III-nitride VCSEL structures [85]. To compensate for the relatively poor lateral hole spreading into the *p*-type GaN layer that is mainly due to current crowding - a detrimental effect whose impact is enhanced by the annular contact geometry - and thus to get light emission from the active region sandwiched between the DBRs, various approaches can be implemented. First a buried, oxidized AlInN interlayer can be inserted on the *n*-side underneath QWs-1 in a similar fashion to that implemented for micro-LEDs [86] to confine the electron current flow in the central part of the device. A transparent conductive oxide (TCO), like indium tin oxide or ZnO, sandwiched between the *p*-type GaN layer and the top dielectric DBR [87] (Fig.4.2) also might be used to improve the lateral spreading of the hole current. Then the use of an electron-blocking layer (EBL), located on top of the electrically-pumped region can act to avoid an excess of electrons on the *p*-type side and thus limit unwanted electron-hole recombination.[88]

Beyond issues related to electrical pumping, another critical parameter when considering the above-mentioned geometry is the significant increase in the effective cavity length (L_{eff}). Indeed, it is known that as a first approximation Ω_{VRS} scales like $1/\sqrt{L_{eff}}$ [89]. However, L_{eff} also includes a contribution associated with the penetration depth of the electromagnetic field into the DBRs and one way to mitigate this effect is to use a top dielectric DBR with a short penetration depth. This can be achieved by adopting the SiO_2/TiO_2 bilayer system since it exhibits a very large refractive index contrast ($n_{TiO_2}(\lambda = 415\text{ nm}) = 2.6$ vs $n_{SiO_2}(\lambda = 415\text{ nm}) = 1.495$) [75]. As an illustration, the penetration depth obtained at λ= 415 nm only amounts to $0.83\lambda/2$ for a SiO_2/TiO_2 DBR

against $2.47\lambda/2$ for the more conventional SiO_2/Si_3N_4 structure, where $n_{Si_3N_4}(\lambda = 415$ nm$) = 1.83$ [90]. Note, however, that the SiO_2/TiO_2 DBR is not suited to a nonresonant optical pumping due to the strong rise in the absorption in TiO_2 layers for wavelengths shorter than 375 nm. However, we have used this structure in the simulations. The electric field profile at λ= 415 nm of the complete structure shown in Fig.4.2, derived from a transfer matrix simulation, along with the corresponding refractive index profile are displayed in Fig.4.3. The refractive indices for the III-nitride compounds were taken from the work of Brunner *et al.*[91] (AlGaN alloys), Carlin *et al.*[92, 93] (AlInN alloys) and Bergmann and Casey [94] (InGaN alloys), respectively, and the refractive index value for ZnO was taken from the work of Schmidt *et al.* [95].

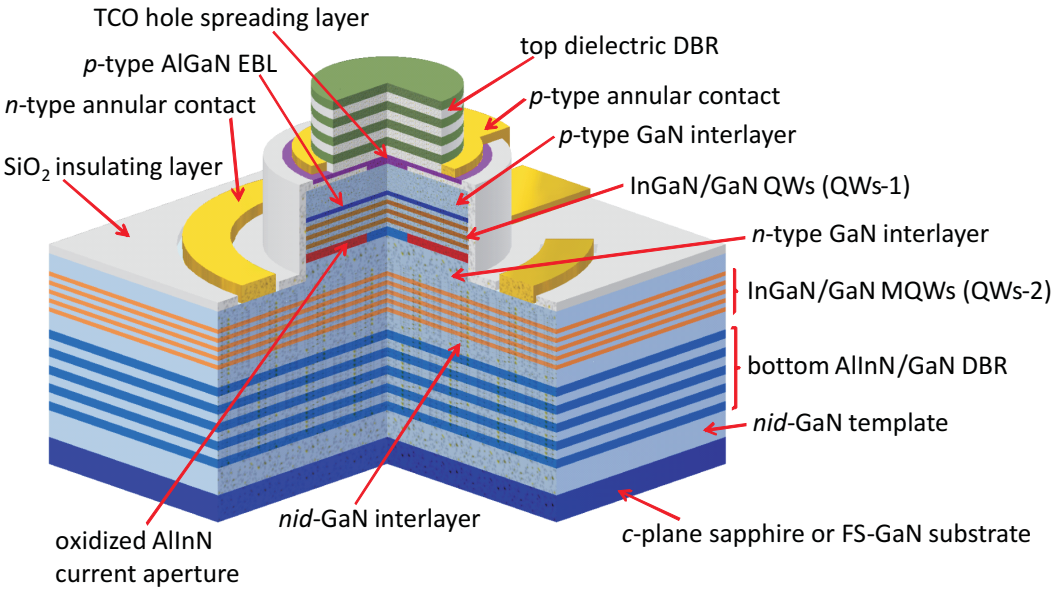

FIG. 4.2: Schematic 3D cross-section of an InGaN/GaN MQW polariton LD based on an intracavity pumping geometry. The structure is sandwiched between bottom (shown in dark blue/light blue) and top (shown in green/white) DBRs. The polaritons are formed in the QWs-2 region (shown in orange/light blue). In the case of intracavity pumping, the QWs-2 are pumped with the optical emission from the electrically pumped QWs-1.

We have considered two types of pumping for the polariton laser illustrated in Fig.4.2:

- Electrons and holes are injected into QWs-2 and QWs-1 are ignored. This pumping scheme is further referred to as electrical pumping.
- QWs-1 are electrically pumped and their optical emission pumps QWs-2. This pumping scheme is further referred to as intracavity pumping.

The two schemes are discussed in more details in section 4.4.2

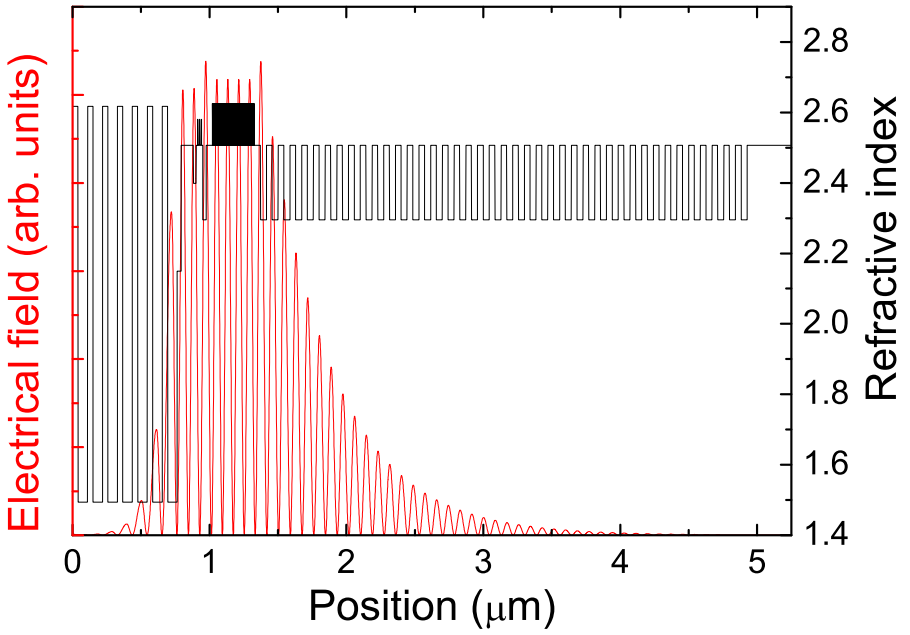

FIG. 4.3: Results of a transfer matrix simulation of the field intensity profile of a polariton LD shown in Fig.4.2 centred at λ= 415 nm along with the corresponding refractive index profile.

4.4 Modelling formalism

4.4.1 Semiclassical Boltzmann equations

Semiclassical Boltzmann equations have been used to describe the polariton laser kinetics. Here we briefly outline how those equation can be derived from the quantum mechanical density matrix formalism by a series of successive approximations.

Let $|\Psi\rangle$ be the field operator for all the quasiparticles in the system, specifically polaritons, photons, phonons and electrons, which obeys the Schrodinger equation:

$$i\hbar\frac{\partial}{\partial t}|\Psi\rangle = \hat{H}|\Psi\rangle, \tag{4.8}$$

where $\hat{H}$ is the full Hamiltonian of the system. The holes are not considered in the simulation since we assume that the active region is $n-doped$ and most of the free carriers are electrons. Now if we introduce the density operator $\hat{\rho} = |\Psi\rangle\langle\Psi|$, then from the Schrödinger equation we can derive the so called Liouville equation for $\hat{\rho}$

$$i\hbar\frac{\partial\hat{\rho}}{\partial t} = [\hat{H}, \hat{\rho}]. \tag{4.9}$$

To proceed further it is necessary to make approximations. We first apply the Born approximation, which neglects the correlations between the polariton, phonon, electron and photon fields in the system. In this case we express the full density operator as a direct product of density operators of the subsystems:

$$\hat{\rho}(t) = \hat{\rho}_{pol}(t) \otimes \hat{\rho}_{phon} \otimes \hat{\rho}_{el} \otimes \hat{\rho}_{\gamma} \tag{4.10}$$

Where $\hat{\rho}_{phon}, \hat{\rho}_{el}, \hat{\rho}_{\gamma}$ correspond to the density operators of the phonon, free electron and photon subsystems, and $\hat{\rho}_{pol}(t)$ is the operator for the polariton subsystem. Moreover, we assume that only the polaritons are described by a time-dependent density operator and all the other operators correspond to thermal equilibrium. In order to eliminate the phonon, electron and photon density operators we take the trace over all except the polariton subsystem, which gives us the following equation for the polariton density operator which will in what follows be denoted by $\hat{\rho}$.

$$\dot{\hat{\rho}} = \mathcal{L}_{pol}\hat{\rho} + \mathcal{L}_{phon}\hat{\rho} + \mathcal{L}_{el}\hat{\rho} + \mathcal{L}_{lifetime}\hat{\rho} + \mathcal{L}_{pump}\hat{\rho}. \tag{4.11}$$

Here each $\mathcal{L}_{\alpha}$ denotes a so called Liouvillian describing the interaction of the polaritonic system with subsystem α. Each Liouvillian contains only the annihilation ($\hat{a}(k)$) and creation ($\hat{a}^{\dagger}(k)$) operators of the polaritons. In order to obtain the semiclassical Boltzmann equation we should apply the Born approximation for the polariton system itself, i.e. assume that there is no coherence between polariton states with different momenta, and that the polariton density operator can be decomposed into a direct product:

$$\hat{\rho}(t) = \hat{\rho}_0(t) \otimes \hat{\rho}_{k1}(t) \dots \hat{\rho}_k(t) \dots . \tag{4.12}$$

If we now take the trace over the polariton states, to get the equations for the polariton numbers in different states $N_k = \langle \hat{a}^{\dagger}(k)\hat{a}(k) \rangle$, they contain fourth order correlators of the form $\langle \hat{a}^{\dagger}(k)\hat{a}(k)\hat{a}^{\dagger}(k')\hat{a}(k') \rangle$ and eighth order correlators of a similar form, like the fourth order correlator $\hat{C}$ which was considered in subsection 3.4.3. However using the Born-Markov approximation we can decompose these operators as $\langle \hat{a}^{\dagger}(k)\hat{a}(k)\hat{a}^{\dagger}(k')\hat{a}(k') \rangle = \langle \hat{a}^{\dagger}(k)\hat{a}(k) \rangle \langle \hat{a}^{\dagger}(k')\hat{a}(k') \rangle = N_k N_{k'}$. As a result, the equations contain only the occupation numbers of different states, resulting in a set of semiclassical Boltzmann equations for the polariton occupation numbers N_k

$$\frac{dN_k}{dt} = P_k - \frac{N_k}{\tau_k} - \sum_{k\prime} W_{k \to k'} N_k (1 + N_{k'}) + \sum_{k'} W_{k' \to k} N_{k'} (1 + N_k), \tag{4.13}$$

where for each state k, P_k denotes the pumping rate and τ_k, and the W terms describe the scattering rates between different polariton states. Each scattering rate contains

three contributions:

$$W = W_{pol-phon} + W_{pol-el} + W_{pol}, \tag{4.14}$$

relating to the polariton-phonon, polariton-electron and polariton-polariton interactions. The derivation of the scattering rates can be found in [96, 97] and the relevant formulae are presented in the next subsection.

The values of wavevector allowed in (4.13) should be considered. To solve the system of equations (4.13) numerically it is necessary to set up a grid of discrete values of wavevector, and the finite size of the device suggests a natural quantization step $\delta k = 2\pi/L$, where L is the characteristic size of polariton excitation spot. The upper limit of the allowed values of k should be chosen as $k_{max} = 2\pi/a_B$ since excitons with wavevectors larger than the inverse Bohr radius cannot be treated as bosons because of the uncertainty principle. Furthermore, we should account for the two-dimensional nature of the polaritons with states described by $\mathbf{k} = [k_x, k_y]$, so the quantization should be performed for both wavevector components. Hence, the estimated number of wavevector values and equations N represented by equation (4.13) is:

$$N = \left(\frac{L}{a_B}\right)^2. \tag{4.15}$$

4.4.2 Scattering rates in polariton relaxation processes

Pumping schemes

In the simulations two different pumping schemes have been considered. In the first scheme, it is assumed that electrically-pumped electrons and holes are uniformly injected into the set of strongly-coupled QWs, emitting at $\sim$ 415 nm (i.e., the QW subset QWs-1 described in section 4.3 is ignored). Such a scheme is not well suited to III-nitride structures with a large N_{QW} but it is adopted as a simplified approach, and one that is potentially applicable to low temperature GaAs-based polariton LDs. After some time, charge carriers are either removed due to nonradiative recombination occurring at dislocations, trapping or Auger recombination, or they bind into pairs forming excitons. Those excitons may be characterized by various energies and in-plane wavevectors ($\mathbf{k}$) and their ensemble is considered as an incoherent reservoir pumped from the electron-hole plasma. This exciton reservoir then feeds the condensate of exciton-polaritons, which is a coherent multiparticle state responsible for polariton lasing.

The second scheme concerns the design shown in Fig.4.2, where the region QWs-1, ideally emitting in the 390-400 nm range, is uniformly electrically-pumped by charge carriers

and high energy photons subsequently emitted by those QWs are then absorbed by QWs-2, [75] which is the set of strongly-coupled QWs, that will lead to the formation of an incoherent exciton reservoir. This intracavity optical pumping geometry essentially differs from the first one by (i) the fact that overall, for a given current density, the population of excitons in the reservoir feeding the condensate will be smaller due to the internal quantum efficiency (IQE), which is less than 100%. This latter quantity is taken to be 90%, which which is typical of state of the art LEDs. (ii) The density of free carriers in the region QWs-2 is constant since they are located in the $n-$type region (cf. Fig. 4.2), whereas this density is current-dependent in the first scheme and will have an impact on the injection-dependence of the exciton-free carrier scattering term. (iii) While one can assume that in the intracavity optical pumping scheme, free electrons in the n-doped region are thermalized and obey Fermi statistics with an effective temperature (T_{eff}) close to the lattice temperature (T_{latt}), in the direct electrical pumping schem,e electrons are not thermalized with the lattice. In this latter situation, we consider a Boltzmann carrier distribution with $T_{eff} > T_{latt}$.

We now present the expressions for the rates of all the kinetic processes in the system pointing out the differences between the two pumping schemes.

Pumping of the polariton laser

In order to evaluate the pumping term in the case of electrical pumping we can write down a simplified rate equation for the number of electron-hole pairs n_{eh} injected in the microcavity:

$$\frac{dn_{eh}}{dt} = \frac{J}{e} - \frac{n_{eh}}{\tau_{eh}} - W n_{eh}, \tag{4.16}$$

where J is the electrical pumping rate, e is the elementary charge, τ_{eh} is the decay rate of the electron-hole plasma, and W is the exciton formation rate from the electron-hole plasma.

Eq. ((4.16)) can be solved analytically to yield the time dependence of $n_{eh}(t)$:

$$n_{eh}\,(t) = \frac{J}{e}\frac{\tau_{eh}}{1 + W\tau_{eh}}\left[1 - \exp\left(-Wt - \frac{t}{\tau_{eh}}\right)\right], \tag{4.17}$$

assuming an electron-hole plasma density equal to zero at $t = 0$. We then assume that the excitons that are formed from the electron-hole plasma, have an additional energy Δ compared to the ground state exciton energy E_x, which is equal to the exciton binding energy and thus the excitons occupy only the relatively high k exciton states with energy

$E(k)$ which are not coupled to the microcavity optical mode. Moreover, we assume that those states are all pumped at an equal rate. Thus, we can write down the expression for the pump term in a simple form:

$$P_k = 0, \quad E_k - E_x < \Delta, \tag{4.18}$$

and,

$$P_k = \frac{W n_{eh}}{\widetilde{N}}, \quad E_k - E_x > \Delta. \tag{4.19}$$

Here $\widetilde{N}$ is the number of states in our quantization lattice which have the energy $E(k)$ satisfying the condition (4.19).

For the intracavity optical pumping geometry we consider that the strongly-coupled quantum wells are indirectly electrically pumped with an energy-dependent optical pump intensity given by:

$$P_k = \frac{\eta_{int} J(\Delta E_k)}{\sqrt{2\pi}(e\delta E)} \exp\left(-\frac{(E_k - E_{pump})^2}{2(\delta E)^2}\right). \tag{4.20}$$

Here J is the electrical current in QWs-1, η_{int} is the internal quantum efficiency of the pumping LED, E_{pump} is the central photon emission energy of the LED which is set equal to the exciton energy of QWs-1, δE is the linewidth of the LED, which is set to 90 meV and is considered temperature-independent as a first approximation, and ΔE_k is the energy range associated with state $\mathbf{k}$, which is the area of the grid cell of the state on the energy grid. Note here that for the sake of illustration we consider the limiting case where the pumping QW set (QWs-1) is resonant with the exciton energy of the second QW set (QWs-2) that leads to the formation of polaritons, to make a clear distinction between the performance of the two possible pumping geometries. However, in practice, a nonresonant intracavity pumping scheme would probably apply.

Polariton lifetime decay

The polariton lifetime τ_k is calculated in the same way for both pumping schemes and can be obtained by relation:

$$\tau_k = \left(\frac{|X_k|}{\tau_x} + \frac{|C_k|}{\tau_c(k)}\right)^{-1}, \tag{4.21}$$

where τ_x and τ_c are the lifetimes of the exciton and cavity mode respectively and X_k and C_k are the Hopfield coefficients which define the polariton components. While the

exciton lifetime is assumed wavevector-independent and has been chosen on the basis of the experimental results provided by our collaborators, the cavity mode lifetime depends on the in-plane wavevector and can be calculated exactly in the approximation of the laterally unbound microcavity by the transfer matrix method, and is just the imaginary part of the eigenfrequency of the structure. The Hopfield coefficients can be calculated using the coupled-oscillator approach in the following way. The Hamiltonian of the system can be expressed in matrix form in the basis of the cavity and exciton modes:

$$\hat{H} = \begin{pmatrix} E_x(k) & \Omega_{VRS} \\ \Omega_{VRS} & E_c(k) \end{pmatrix} \tag{4.22}$$

The eigenvalues of this matrix are the energies of the lower and upper polariton states:

$$E_{up}(k) = \frac{E_x(k) + E_c(k) + \sqrt{(E_x(k) - E_c(k))^2 + 4\Omega_{VRS}^2}}{2}, \tag{4.23}$$

$$E_{low}(k) = \frac{E_x(k) + E_c(k) - \sqrt{(E_x(k) - E_c(k))^2 + 4\Omega_{VRS}^2}}{2}. \tag{4.24}$$

The Hopfield coefficients for the lower polariton branch are the components of the normalized eigenvector corresponding to the lower polariton eigenvalue and are given by:

$$X_k = \frac{1}{\sqrt{1 + \left[(E_{low}(k) - E_c(k))/(\Omega_{VRS})\right]^2}}, \tag{4.25}$$

$$C_k = \frac{1}{\sqrt{1 + \left[\Omega_{VRS}/(E_{low}(k) - E_c(k))\right]^2}}. \tag{4.26}$$

Polariton-phonon scattering

The expressions for the scattering process involving acoustic phonons are equivalent for both pumping schemes. Two opposite processes take place in the system: absorption of an acoustic phonon by a polariton with scattering to a higher k state, and emission of a phonon with relaxation of the polariton to a lower k state. The exciton-phonon interaction matrix element has been calculated in [98] as:

$$W_{k\to k\prime}^{exc-ph} = \frac{\Theta^2(q)}{\hbar\rho_0 c_s S^2}\left(N_{phon}(q) + \frac{1 \pm 1}{2}\right)\frac{q^2}{q_z}\theta(q - q_z), \tag{4.27}$$

where the plus sign correponds to the emission of a phonon, and minus to the absorption of a phonon. q is the magnitude of the phonon wavevector and can be obtained from energy conservation and the phonon dispersion to give $q = |E_p(k) - E_p(k\prime)|/c_s$, where c_s is the speed of sound in the material, and $E_p(k)$ is the energy of a polariton with wavevector $\mathbf{k}$. Since the excitons are two-dimensional quasiparticles and the phonons

are three dimensional, only the in-plane component of the phonon wavevector $q_{\|}$ must meet the momentum conservation law: $q_{\|} = |\mathbf{k} - \mathbf{k}'|$. The orthogonal component of the phonon wavevector is $q_z = \sqrt{q^2 - q_{\|}^2}$. ρ_0 is the mass density of the material and S is the area of the cavity. N_{phon} is a Bose-Einstein distribution, since we assume that the phonon subsystem remains in the thermal equilibrium. θ is a Heaviside step function and the function Θ can be written as:

$$\Theta = \frac{D_e Z_e(q_z)}{\left[1 + m_h q_{\|} a_B/(2m_x)\right]^{3/2}} + \frac{D_h Z_h(q_z)}{\left[1 + m_h q_{\|} a_B/(2m_x)\right]^{3/2}}, \tag{4.28}$$

where D_e, D_h are the deformation potentials for electrons and holes, and m_e, m_h, m_x are the electron, hole and exciton effective masses. $Z_{e,h}$ are the overlap integrals between the phonon and electron (hole) wavefunctions:

$$Z_{e,h}(q_z) = \int_{z=-\infty}^{z=+\infty} dz \phi_{e,h}^2(z) e^{iq_z z}, \tag{4.29}$$

where $\phi_{e,h}$ are the normalized one-dimensional wavefunctions for electrons and holes. In order to obtain the polariton-phonon scattering rate, we should multiply the exciton phonon scattering rate by the Hopfield coefficients for the initial and final states:

$$W_{k \to k\prime}^{pol-ph} = W^{exc-ph} |X_k| |X_{k'}|. \tag{4.30}$$

The interaction with acoustic phonons is one of the main mechanisms of relaxation for the excitons. However, it becomes inefficient for polaritons because of the region of very large group velocity, the so called bottleneck region, which is situated close to the inflection point point of the lower polariton band. The polariton-phonon relaxation is suppressed in this region, because there is a lack of phonons with the appropriate momentum and energy. Thus, when only the polariton-phonon relaxation exists, the polaritons tend to accumulate in the bottleneck region. However, the accumulation of the polaritons in this region is reduced by the other relaxation processes that occur, such as polariton-polariton and polariton-free electron scattering, which will be discussed later in this section. Polariton-phonon scattering also affects the depletion of the ground state, since the polaritons absorb phonons and are scattered to the higher energy states [99, 100].

Polariton-optical phonon scattering has not been considered in the modelling, because optical phonons in the III-nitride semiconductors have an almost flat dispersion throughout the Brilloin zone and have the energy of the order of 130 meV, which is larger then the energy mismatch between the ground polariton state and the highest polariton state considered in the simulation. Thus, optical phonons cannot provide the scattering from

one polariton state to another. However, optical phonon scattering has been accounted for by the modification to the exciton lifetime, a value for which was provided by our experimental collaborators.

Polariton-polariton scattering

The polariton-polariton scattering rate is the same for the both pumping schemes and can be calculated in the following way. A derivation of the formula for the rate can be found in [97] (and references therein) which gives:

$$W_{k\to k'} = \frac{2\pi}{\hbar}\sum_{\mathbf{q}} |M^{ex}|^2 |X_k||X_{k'}||X_q||X_{\mathbf{k+q-k'}}| n_q(1+n_{\mathbf{k+q-k'}}) \times F(\mathbf{k},\mathbf{k'},\mathbf{q}), \quad (4.31)$$

where

$$M^{ex} = 6\frac{a_B^2}{S}E_X^B \quad (4.32)$$

and the function $F(\mathbf{k},\mathbf{k\prime},\mathbf{q})$ corresponds to the energy conservation condition taking into account the finite polariton lifetime:

$$F(\mathbf{k},\mathbf{k'},\mathbf{q}) = \frac{\hbar/\tau_{k'}}{\left(E(k)+E(q)-E(k')-E(|\mathbf{k}+\mathbf{q}-\mathbf{k'}|)\right)^2 + (\hbar/\tau_{k'})^2}. \quad (4.33)$$

A few computational considerations should be mentioned here. The first one is the fact that the polariton-polariton scattering rate contains the *a priori* unknown polariton occupation numbers. Thus, in order to calculate the polarion-polariton scattering dynamics, the scattering rates should be recalculated at each time step, which makes the computation extremely time-consuming. It is also worth mentioning that due to the uniform wavevector quantization lattice it is always possible to find a lattice node corresponding to the state $\mathbf{k}+\mathbf{q}-\mathbf{k'}$, which means that we can also fulfil the momentum quantization rule. However, we could consider another quantization scheme for which the energies of the quantized states are uniformly distributed as in [96]. In this case, we could automatically fulfil the energy conservation condition , but we would also be obliged to introduce an additional function describing the momentum mismatch. Unlike the energy broadening, which occurs due to the finite polariton lifetime, the broadening of the momentum is due to the finite area of the sample and is related to the inverse length of the sample for all the states. It is clear that in a real experimental set up there would be broadening both in energy and in momentum, which cannot be accounted for in the simulation due to the computational difficulty. The final comment that should be made is that in order to simplify the computation it is instructive to set the terms of the sum in the Eq.(4.31) to zero in the case of large energy mismatch. If we do this, the final

Jacobian, which is calculated during the numerical solution of the system of differential equations, becomes sparse and makes the computation far more time-efficient.

Polariton-free electron scattering

This mechanism has been shown to play a key role in polariton condensation in the case of non-resonant pumping [101]. The expression for the polariton-free electron scattering rate has been derived in [102]. Two process may occur during the exciton-electron scattering: elastic scattering of the exciton from a free electron and the dissociation of the exciton into an electron and hole. In our simulations we account explicitly only for the elastic process. The inelastic dissociation process has been accounted for implicitly by the corrections to the exciton non-radiative lifetime. The general expression for the polariton-electron scattering rate is given by:

$$W^{pol-el}_{\mathbf{k}\to\mathbf{k'}} = |X_k||X_{k'}|\frac{S}{2\pi\hbar}\int d^2k_e \frac{|V_{exc}+V_{dir}|^2\delta(k_e-k_e^*)}{\left[\frac{d(E_e(k_e)-E_e(|\mathbf{k_e}+\mathbf{k}-\mathbf{k'}|))}{dk_e}\right]_{k_e=k_e^*}} \times f(k_e)\times(1-f(|\mathbf{k_e}+\mathbf{k}-\mathbf{k'}|)). \tag{4.34}$$

Here k_e^* is the electron wavevector which satisfies the energy conservation condition:

$$E_{pol}(k)+E_e(k_e) = E_{pol}(k')+E_e(|\mathbf{k_e}+\mathbf{k}-\mathbf{k'}|). \tag{4.35}$$

The function f is the electron momentum distribution function, which differs significantly for the two pumping schemes. In the case of intracavity pumping we assume that the electrons are in thermal equilibrium with the system and are described by a Fermi-Dirac distribution: $f = [\exp((E_e-\mu)/kT)+1]^{-1}$ with temperature equal to the lattice temperature and chemical potential μ:

$$\mu = kT\log\left(\exp\left[\frac{\pi\hbar^2 n_e}{m_e kT}\right]-1\right), \tag{4.36}$$

where n_e is the concentration of the free electrons in the system. For the case of the electrical pumping we also assume a Fermi Dirac distribution of the electrons, but in this case the temperature of the electron gas is much higher than the lattice temperature and does not depend on it, and the total concentration of the electrons depends on the pumping current and is proportional to the total number of electrons obtained from equation Eq.(4.17). V_{exc} and V_{dir} are the matrix elements of the exchange and direct scattering mechanisms respectively. The matrix element of the direct Coulomb

interaction is given by:

$$V_{dir}(q) = \frac{4\pi e^2 a_b^3}{\varepsilon_0 S D_{qw}} h(a_B q) \left(g(\beta a_b q/2) - g(\alpha a_b q/2) \right), \tag{4.37}$$

where $q = |\mathbf{k} - \mathbf{k\prime}|$, $\alpha = m_e/m_x$, $\beta = m_h/m_x$, and functions g, h have the forms:

$$g(a_B q) = [1 + (a_B q)^2]^{-3/2}, \tag{4.38}$$

$$h(a_B q) \approx \frac{D_{QW}^2 q^2}{2(a_B q)^3}. \tag{4.39}$$

The exchange interaction term is:

$$V_{exc}(\mathbf{\Delta k}, q) = -\frac{8e^2 a_B^5}{\varepsilon_0 S D_{QW}^2} \int d^2 k_1 h(a_B k_1) g(\alpha |\mathbf{k_1} + \alpha \mathbf{q} - \mathbf{\Delta k}|) \times (g(\alpha |\mathbf{k_1} + \mathbf{q} - \mathbf{\Delta k}|) - g(\alpha |\mathbf{q} - \mathbf{\Delta k}|)), \tag{4.40}$$

where $\mathbf{\Delta k} = \mathbf{k_e} - \alpha \mathbf{k}$. This integral should be calculated numerically. Despite the considerable difficulty which arise in the calculation of the exchange term, it cannot be omitted in the modelling since it is dominant in the polariton-free electron scattering.

4.5 Numerical results and discussion

In the numerical calculations we have used the parameters, presented in table 4.1 with the right column showing the source in the literature for the value quoted. When no source is shown the value was provided by our experimental collaborators.

TABLE 4.1: Parameters of the modelling of polariton laser

Parameter	**Value**	**Source**
cavity photon lifetime τ_c	1 [ps]	
exciton lifetime τ_x	1 [ns]	[61]
lateral size of the system L	50 [μm]	[61]
electron-hole pair lifetime τ_{eh}	5 [ns]	[103]
exciton formation rate W	0.01 [ps^{-1}]	[103]
exciton binding energy E_b	45 [meV]	
Rabi-splitting Ω_R	45 [meV]	
number of quantum wells N_{QW} (QWs-2)	65	device design
exciton inhomogeneous broadening γ_{ex}	35 [meV]	
effective electron mass m_e	0.2 free electron mass	[104]
effective hole mass m_h	1.1 free electron mass	[104]
deformation potential D	11.1 [eV]	[104]
mass density ρ_0	6150 [kg/m^3]	
speed of sound c_s	7960 [m/s]	[105]
internal quantum efficiency η_{int}	0.9	
effective electron temperature	800 K	

Values of the parameters used in the modelling. Right column shows the source in the literature for the value quoted. When no source is shown the value was provided by our experimental collaborators.

Figure 4.4 shows the evolution of the ground state polariton occupation number vs pump current density for different temperatures and detunings for the two pumping geometries. In a realistic set up, changing the cavity mode frequency would inevitably change other parameters such as Rabi-splitting for example. However, in the modelling we assume the detuning to be decoupled from the other parameters of the system, so that it can be changed independently. The threshold current density for condensation (J_{thr}) can be clearly identified in each case. The detuning is defined as difference between the ground exciton and cavity mode energy, which is in its turn defined by the cavity length and the refractive index.

We have also calculated the J_{thr} dependence as a function of temperature and detuning which is shown in Fig. 4.5. In this way one obtains the polariton condensation phase

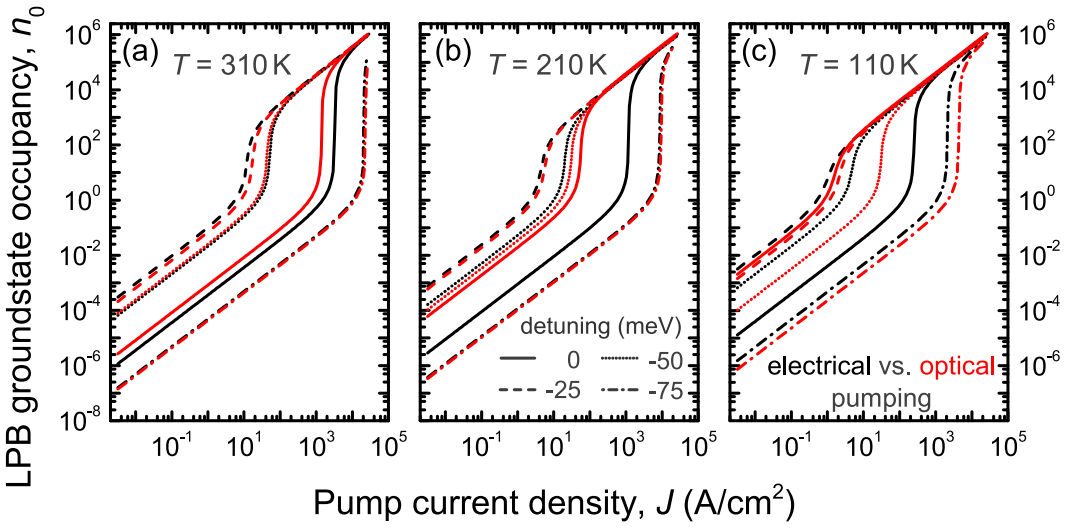

FIG. 4.4: (a)-(c) Occupancy of the polariton ground state vs pump current density calculated for the two pumping geometries at various temperatures and detunings (see text for details).

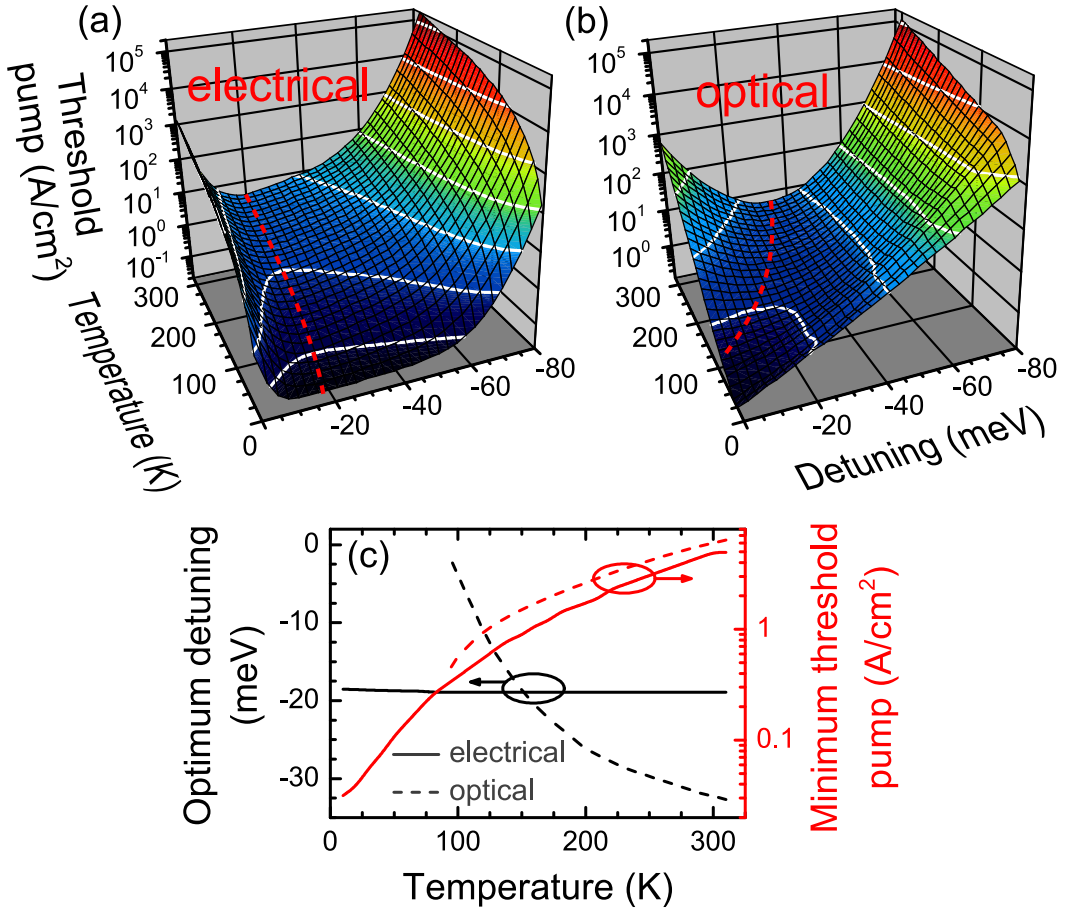

FIG. 4.5: Plots of J_{thr} vs detuning and temperature for (a) the direct electrical and (b) the intracavity optical pumping schemes. The red dashed line on each plot corresponds to the evolution of $J_{thr,min}$ as a function of temperature. (c) Evolution of the optimum detuning (black solid and black dashed lines) and condensation threshold current density (red solid and red dashed lines) at the optimum detuning as a function of lattice temperature for the direct electrical (solid lines) and the intracavity (dashed lines) pumping schemes.

diagram under electrical pumping, which is analogous to that derived under optical pumping for GaN/AlGaN MQW microcavities [79, 100]. One can see that at room temperature the lowest threshold current density ($J_{thr,min}$) is obtained for a negative detuning of -19 meV and amounts to ~ 5 Acm^{-2} for the direct electrical pumping geometry while a $J_{thr,min}$ value of ~ 6 Acm^{-2} at a detuning of -32 meV is derived for the intracavity pumping geometry. The values are in good agreement with those predicted in previous work [75]. The optimum detuning (δ_{opt}) corresponds to the case where the mean polariton relaxation time equals the mean polariton lifetime [100, 106]. The system then switches from the kinetic to the thermodynamic regime. In other words, it undergoes a crossover from a regime where J_{thr} decreases with increasing detuning (decreasing of δ absolute value), because of the enhancement of the total scattering rate to the ground state, to a regime where J_{thr} increases concomitantly with δ due to the combined effects of the increasing polariton effective mass (which leads to a larger value of the critical density for polariton condensation, $n_{2D,crit}$) and thermal detrapping from the ground state [100]. It is also noticeable that the temperature dependence of δ_{opt} significantly differs from one geometry to the other (Figs. 4.5(a) to 4.5(c)). This is attributed to the difference in the efficiency of the free electron scattering mechanism as a function of temperature [101]. For the direct electrical pumping geometry, the electron distribution does not depend on T_{latt}, since electrons are not thermalized, thus leading only to slight changes in the free electron scattering rate with temperature and thereby explaining the weak $\delta_{opt}(T)$ variation displayed in Figs. 4.5(a) and 4.5(c). While for the intracavity optical pumping geometry, electrons are thermalized to T_{latt}, which leads to a behaviour closer to that reported for GaN/AlGaN MQW microcavities under nonresonant optical pumping (Figs. 4.5(b) and 4.5(c)) [100]. However, it should be recognized that assuming an electron temperature equal to T_{latt} is a crude approximation. We should also point out that, for the sake of simplicity, we did not account for the large activation energy of the Mg acceptor in GaN compounds, which would probably degrade the electrical characteristics and thus lead to an increase in J_{thr} at low temperatures.

The low threshold values reported for the intracavity pumping geometry can probably be explained by the broad spectral distribution of the pump P_k. In the direct electrical injection geometry, excitons characterized by high energies and large in-plane wave vectors are created from the electron-hole plasma, which requires a comparatively long time to relax to the $k = 0$ state. However, in the case of intracavity optical pumping a broad distribution of excitons centered on the QW-1 exciton energy, but also covering lower energy states, is created. Those excitons which occupy lower energy and lower $\mathbf{k}$ states compared with the direct electrical pumping geometry quickly relax to the lower polariton branch ground state and enhance polariton relaxation, which results in the lower threshold for this geometry. However, if the intracavity emission line is strongly

blueshifted from the polariton modes, the ratio between the polariton lasing thresholds for the two pumping configurations is expected to be modified. One would then expect a higher threshold for the intracavity pumping geometry owing to the IQE of the internal pump, which is less than 100%.

4.5.1 Simplified rate equation modeling: steady-state solutions

In order to obtain a qualitative understanding of the functionality of polariton laser diodes we compare the modelling results obtained with the full set of semi-classical Boltzmann equations with a simplified quasi-analytical model. For the direct electrical pumping geometry, the model is based on three rate equations describing the electron-hole plasma (namely Eq. (4) introduced in section III.A), the exciton reservoir and ground state polaritons, respectively:

$$\frac{dn_x}{dt} = -\frac{n_x}{\tau_x} + Wn_{eh} - an_x\left(n_p+1\right) + ae^{-\beta\Delta_{esc}}n_pn_x - bn_x^2\left(n_p+1\right) - cn_{eh}n_x\left(n_p+1\right), \tag{4.41}$$

$$\frac{dn_p}{dt} = -\frac{n_p}{\tau_p} + an_x\left(n_p+1\right) - ae^{-\beta\Delta_{esc}}n_pn_x + bn_x^2\left(n_p+1\right) + cn_{eh}n_x\left(n_p+1\right), \tag{4.42}$$

where n_x, and n_p are the concentrations of excitons and exciton-polaritons, respectively. τ_p is the lifetime of exciton-polaritons in the ground state, a accounts for the acoustic phonon relaxation rates, $\beta = 1/k_BT$, and Δ_{esc} is the characteristic energy splitting between the bottom of the LPB and states beyond the inflection point of the LPB where zero in-plane wavevector polaritons are scattered, which is a quantity sensitive to the detuning [79, 99, 100]. b is the exciton-exciton scattering rate and c is the rate of exciton relaxation mediated by free carriers. The solid line curves in Fig. 4.6 show the detuning dependence of the fitting parameters a, b, and c (for different temperatures) for them to yield the same threshold pumping current density for the direct electrical pumping scheme as the full semi-classical Boltzmann model predicts.

If now the more realistic intracavity optical pumping geometry is considered, the previous quasi-analytical three-level model can be simplified further to a two-level model since the free carrier dynamics does not have to be accounted for explicitly. Then:

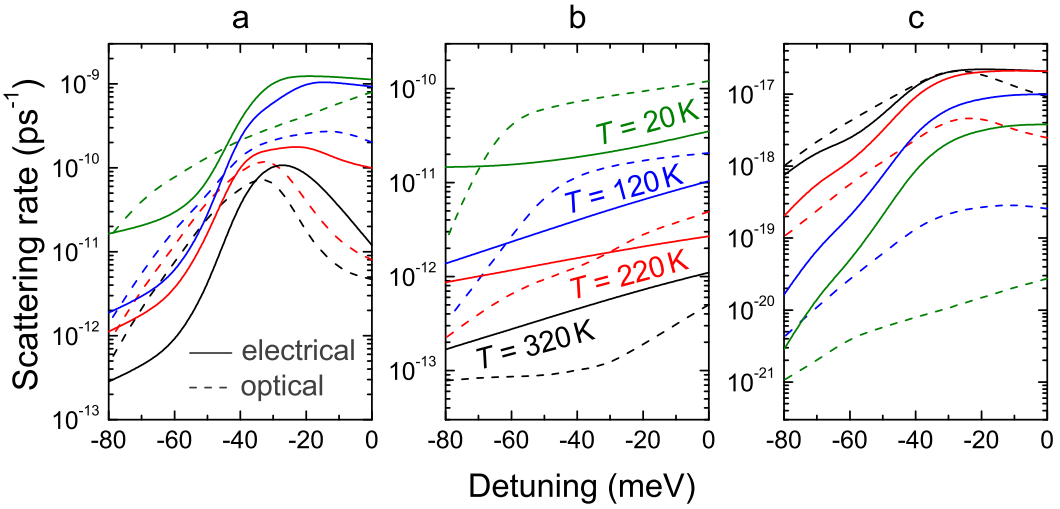

FIG. 4.6: Averaged scattering rates a, b, and c as a function of detuning obtained by fitting the full semi-classical Boltzmann system of equations at various temperatures for the two pumping schemes: electrical (solid lines) and intracavity (dashed lines) pumping.

$$\frac{dn_x}{dt} = P_x - \frac{n_x}{\tau_x} - an_x\left(n_p+1\right) + ae^{-\beta\Delta_{esc}}n_pn_x - bn_x^2\left(n_p+1\right) - cn_dn_x\left(n_p+1\right), \quad (4.43)$$

$$\frac{dn_p}{dt} = -\frac{n_p}{\tau_p} + an_x\left(n_p+1\right) - ae^{-\beta\Delta_{esc}}n_pn_x + bn_x^2\left(n_p+1\right) + cn_dn_x\left(n_p+1\right), \quad (4.44)$$

where n_d is the concentration of free-carriers obtained from the doping level in the region QWs-2, and taken equal to 2×10^{12} cm^{-2}. In the simplest approximation P_x can be taken to be $P_x = \eta_{int}J/q$, where η_{int} is the internal quantum efficiency of the electrically-pumped region QWs-1. The dashed lines in Fig. 4.6 show the values of the fitting parameters a, b, and c which yield the same threshold pumping current density for the intracavity optical pumping scheme as the full semi-classical Boltzmann model for different temperatures and detunings.

One can see in this latter figure that - overall - all the scattering mechanisms that contribute to populate the polariton lasing mode become more efficient with decreasing negative detuning (in absolute value). It could be explained by the reduction of the exciton fraction of the polariton states at large negative detuning, so that all interactions involving polaritons become weaker than at zero or positive detuning. In some cases, the detuning dependence of the scattering rates is non-monotonic and it is also sensitive to the pumping scheme. This is due to the complexity of the lower polariton branch

dispersion. The average scattering rates are therefore sensitive to both the shape of the polariton dispersion and the excitation spectrum profile.

Above threshold the $(1+n_p)$ and $(1+n_x)$ terms appearing in the rate equations can be approximated as n_p and n_x, respectively. After some algebra the steady-state solutions ($t = +\infty$) for the electron-hole pair, exciton and polariton populations for the direct electrical pumping geometry are obtained as:

$$n_{eh_\infty} = \frac{J\tau_{eh}}{q(1+\tau_{eh}W)}, \tag{4.45}$$

$$n_{x_\infty} = \frac{-cn_{eh_\infty} + a(e^{-\beta\Delta_{esc}} - 1) + \sqrt{(-cn_{eh_\infty} + a(e^{-\beta\Delta_{esc}} - 1))^2 + \frac{4b}{\tau_p}}}{2b}, \tag{4.46}$$

$$n_{p_\infty} = \tau_p(Wn_{eh_\infty} - \frac{n_{x_\infty}}{\tau_x}). \tag{4.47}$$

Note that for the intracavity optical pumping geometry, slight changes occur since n_{eh_∞} in Eq. (4.46) has to be replaced by n_d, and Wn_{eh_∞} in Eq. (4.47) has to be replaced by P_x. We should emphasize that for this latter geometry the carrier population, which acts as a reservoir for the stimulated relaxation process (here the excitons), gets clamped once it crosses the condensation threshold, which is expected owing to the similarities of the above-mentioned rate equations with those describing conventional laser diodes [107]. A similar treatment can be used for the direct electrical pumping geometry since $4b/\tau_p \gg (-cn_{eh_\infty} + a(e^{-\beta\Delta_{esc}} - 1))^2$. Thus, for both cases, we obtain $n_{x_\infty} \approx 1/\sqrt{b\tau_p}$. The evolution of n_{x_∞} as a function of temperature at the optimum detuning is shown in Fig.4.7 using both the exact expression and the approximate one for the two pumping geometries. The validity of the approximation for n_{x_∞} is confirmed by the close correspondence between the two quantities whatever the temperature. Considering its approximate expression, the increase with temperature of n_{x_∞} can be directly inferred from the results displayed in Fig. 4.6, which show a decrease in the exciton-exciton scattering rate b with increasing T_{latt}, and is also fully consistent with the overall temperature dependence of the analytical expression for b derived by Tassone and Yamamoto [96]. Note that one also expects a decrease in n_{x_∞} with increasing detuning probably due to the concomitant increase in the relaxation process from the excitonic reservoir (which coincides with the decrease or even the disappearance of the relaxation bottleneck) and that of τ_p [96]. Because low J_{thr} values in the condensation phase diagram are essentially reported for negative δ values (cf. Figs. 4.5(a) and 4.5(b)), one should keep in mind that the present situation corresponds to a decrease of δ in absolute value.

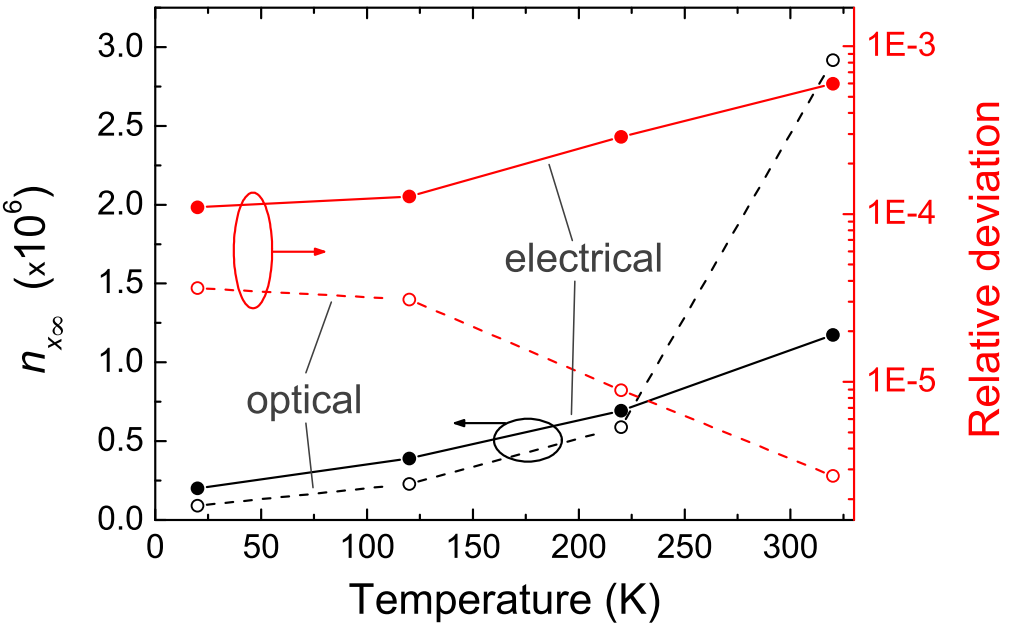

FIG. 4.7: Left-hand side vertical scale: evolution of n_{x_∞} as a function of temperature calculated at the optimum detuning using the exact expressions for the electrical (connected black dots) and the intracavity (connected black circles) pumping geometries (see text for details). Right-hand side vertical scale: relative deviation between the exact and the approximated expressions for the electrical (connected red dots) and the intracavity (connected red circles) pumping geometries.

4.5.2 Simplified rate equation modelling: high-speed current modulation treatment

In this section, the dynamical response of polariton laser diodes (LDs) to a small perturbation, such as a modulation of the current above threshold, is investigated. Since exact analytical solutions to the full rate equations cannot be obtained, a differential analysis of the simplified rate equations given in the previous section using the approach described by Coldren and Corzine for the case of conventional diodes is considered [107]. The resulting small-signal responses are derived by taking the differential of the rate equations which can be written in compact matrix form for the two pumping geometries as follows:

Electrical pumping geometry

$$\frac{d}{dt}\begin{bmatrix} dn_x \\ dn_p \end{bmatrix} = \begin{bmatrix} -\gamma_{xx} & -\gamma_{xp} \\ \gamma_{px} & -\gamma_{pp} \end{bmatrix} \begin{bmatrix} dn_x \\ dn_p \end{bmatrix} + \begin{bmatrix} dn_{eh}(W - cn_{x_\infty} n_{p_\infty}) \\ 0 \end{bmatrix} \tag{4.48}$$

where

$$\gamma_{xx} = \frac{1}{\tau_x} + an_{p_\infty} + 2bn_{x_\infty}n_{p_\infty} + cn_{eh_\infty}n_{p_\infty} - an_{p_\infty}e^{-\beta\Delta_{esc}}, \tag{4.49}$$

$$\gamma_{pp} = \frac{1}{\tau_p} - an_{x_\infty} - bn_{x_\infty}^2 - cn_{eh_\infty}n_{x_\infty} + an_{x_\infty}e^{-\beta\Delta_{esc}}, \tag{4.50}$$

$$\gamma_{xp} = an_{x_\infty} + bn_{x_\infty}^2 + cn_{eh_\infty}n_{x_\infty} - an_{x_\infty}e^{-\beta\Delta_{esc}}, \tag{4.51}$$

$$\gamma_{px} = an_{p_\infty} + 2bn_{x_\infty}n_{p_\infty} + cn_{eh_\infty}n_{p_\infty} - an_{p_\infty}e^{-\beta\Delta_{esc}}. \tag{4.52}$$

Intracavity pumping geometry

$$\frac{d}{dt}\begin{bmatrix} dn_x \\ dn_p \end{bmatrix} = \begin{bmatrix} -\gamma_{xx} & -\gamma_{xp} \\ \gamma_{px} & -\gamma_{pp} \end{bmatrix}\begin{bmatrix} dn_x \\ dn_p \end{bmatrix} + \begin{bmatrix} \frac{\eta_{int}}{q}dJ \\ 0 \end{bmatrix} \tag{4.53}$$

where

$$\gamma_{xx} = \frac{1}{\tau_x} + an_{p_\infty} + 2bn_{x_\infty}n_{p_\infty} + cn_dn_{p_\infty} - an_{p_\infty}e^{-\beta\Delta_{esc}}, \tag{4.54}$$

$$\gamma_{pp} = \frac{1}{\tau_p} - an_{x_\infty} - bn_{x_\infty}^2 - cn_dn_{x_\infty} + an_{x_\infty}e^{-\beta\Delta_{esc}}, \tag{4.55}$$

$$\gamma_{xp} = an_{x_\infty} + bn_{x_\infty}^2 + cn_dn_{x_\infty} - an_{x_\infty}e^{-\beta\Delta_{esc}}, \tag{4.56}$$

$$\gamma_{px} = an_{p_\infty} + 2bn_{x_\infty}n_{p_\infty} + cn_dn_{p_\infty} - an_{p_\infty}e^{-\beta\Delta_{esc}}. \tag{4.57}$$

To obtain the small-signal response of the exciton (dn_x) and the polariton (dn_p) populations to a sinusoidal current modulation dJ, we assume solutions of the form $dJ = J_1\exp(i\omega t)$, $dn_{eh} = n_{eh1}\exp(i\omega t)$, $dn_x = n_{x1}\exp(i\omega t)$, and $dn_p = n_{p1}\exp(i\omega t)$. The linear systems ((4.48)) and ((4.53)) can then be solved for the small-signal polariton population by simply applying Cramer's rule. The small-signal solutions after expansion of the determinants can be written as:

Electrical pumping geometry

$$n_{p1}(\omega) = \frac{\gamma_{px}[W - cn_{x_\infty}n_{p_\infty}] + (i\omega + \gamma_{xx})cn_{x_\infty}n_{p_\infty}}{(\gamma_{px}/\tau_p - \omega^2 + i\omega\gamma_{xx})}\frac{J_1/q}{i\omega + W + 1/\tau_{eh}} = n_{p1}(0)H(\omega), \tag{4.58}$$

where $H(\omega)$ is the modulation transfer function given by:

$$H(\omega) = \frac{\gamma_{px}/\tau_p(W + 1/\tau_{eh})}{\gamma_{px}[W - cn_{x_\infty}n_{p_\infty}] + \gamma_{xx}cn_{x_\infty}n_{p_\infty}} \frac{\gamma_{px}[W - cn_{x_\infty}n_{p_\infty}] + (i\omega + \gamma_{xx})cn_{x_\infty}n_{p_\infty}}{(\gamma_{px}/\tau_p - \omega^2 + i\omega\gamma_{xx})(i\omega + 1/\tau_{eh} + W)}. \tag{4.59}$$

Intracavity pumping geometry

$$n_{p1}(\omega) = \frac{\gamma_{px}\eta_{int}J_1/q}{(\gamma_{px}/\tau_p - \omega^2 + i\omega\gamma_{xx})} = n_{p1}(0)H(\omega) \tag{4.60}$$

where $H(\omega)$ is the modulation transfer function given by:

$$H(\omega) = \frac{\gamma_{px}/\tau_p}{(\gamma_{px}/\tau_p - \omega^2 + i\omega\gamma_{xx})}. \tag{4.61}$$

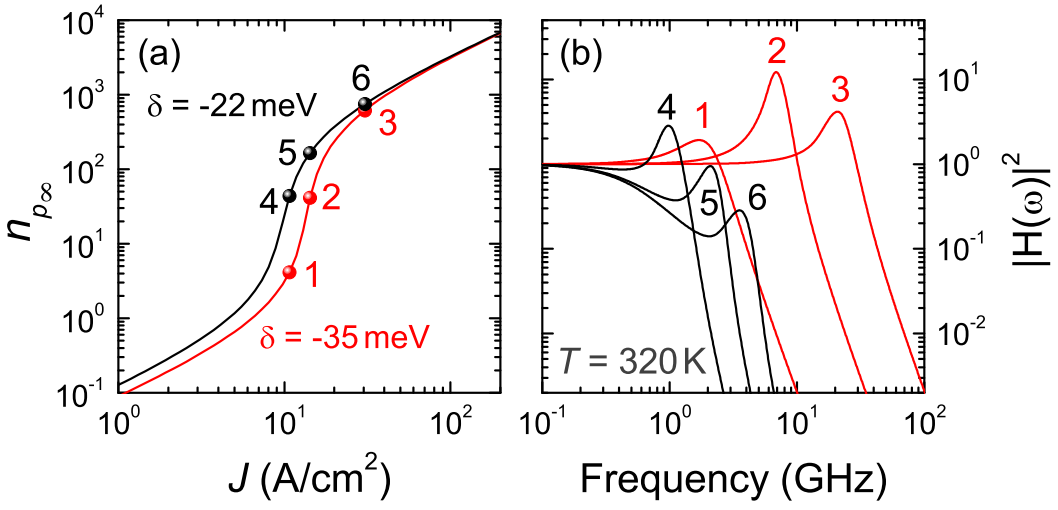

FIG. 4.8: (a) Polariton condensate occupation number vs current density for the electrical (red line) and intracavity (black line) pumping geometries determined at 320 K and at the optimum detuning. (b) Frequency dependence ($\nu = \omega/2\pi$) of the square modulus of the modulation transfer function, $|H(\omega)|^2$. Each curve corresponds to one of the steady state solutions indicated in Fig. 4.8(a).

For both pumping geometries a relaxation resonance frequency equal to $\omega_{R,polLD} = \sqrt{\gamma_{px}/\tau_p}$ can be defined while the γ_{xx} term can be readily identified with a damping factor.

The expression for γ_{px} derived for the two geometries (Eqs. (4.52) and (4.57)) can be greatly simplified since the term describing the exciton-exciton interaction ($\propto b$) dominates over the phonon-exciton and the free carrier-exciton scattering terms ($\propto a$ and c, respectively) whatever the exciton-photon detuning and the temperature (cf. Fig. 4.7). Consequently, the square of the resonance frequency reduces to:

$$\omega_{R,polLD}^2 \approx \frac{2bn_{x_\infty}n_{p_\infty}}{\tau_p} \approx 2n_{p_\infty}\sqrt{\frac{b}{\tau_p^3}}. \tag{4.62}$$

Therefore, within this theoretical framework, the resonance frequency for polariton LDs is directly proportional to the square root of the polariton population in the condensate and inversely proportional to the square root of the polariton lifetime (keeping in mind that the exciton population of the reservoir n_{x_∞} is clamped above threshold). In this respect, such a dependence is similar to the dependence of ω_R in conventional LDs above threshold, since in this latter case:

$$\omega_R^2 \approx \frac{v_g a_{diff} N_p}{\tau_{cav}}, \tag{4.63}$$

where v_g is the group velocity, a_{diff} is the differential gain, N_p is the average photon density in the cavity, and τ_{cav} is the cavity photon lifetime already defined in section III.A [107].

From Eqs. (4.49) and (4.54), the damping factor can be rewritten as:

$$\gamma_{xx} = \frac{1}{\tau_x} + \gamma_{px} = \frac{1}{\tau_x} + \omega_R^2\tau_p. \tag{4.64}$$

It is thus seen that for large resonance frequencies, the damping of the response is ruled by the polariton lifetime. On the other hand, the inverse of the exciton lifetime acts as a damping factor offset, which is important for small polariton condensate populations where the resonance frequency is small.

At this stage, we should point out that the validity of the previous treatment for the intracavity pumping scheme might be limited by the actual response of the pumping LED. Therefore it is necessary to determine the LED cutoff frequency $\omega_{3dB,LED}$, i.e.,

the frequency at which the electrical power response drops to half its dc value, and compare it to $\omega_{R,polLD}$.

Following the theoretical approach described in previous sections, the rate equation governing the emission of the LED is given by:

$$\frac{dn_x}{dt} = -\frac{n_x}{\tau_x} + W n_{eh}, \tag{4.65}$$

from which one can deduce the modulation transfer function $H_{LED}(\omega)$ using harmonic analysis:

$$H_{LED}(\omega) = \frac{1/\tau_x \left(1/\tau_{eh} + W\right)}{\left(i\omega + 1/\tau_x\right)\left(i\omega + 1/\tau_{eh} + W\right)}. \tag{4.66}$$

The corresponding relaxation resonance frequency $\omega_{R,LED}$ and the damping factor γ_{LED} can be written as:

$$\omega_{R,LED} = \sqrt{\frac{1}{\tau_x}\left(\frac{1}{\tau_{eh}} + W\right)} \approx 20.1 \text{ ns}^{-1}, \tag{4.67}$$

which corresponds to 3.2 GHz, and

$$\gamma_{LED} = \frac{1}{\tau_x} + \frac{1}{\tau_{eh}} + W = 70.4 \text{ ns}^{-1}, \tag{4.68}$$

which corresponds to 11.2 GHz, respectively. Additional features of the LED response can be derived from the frequency dependence of the square modulus of $H_{LED}(\omega)$. On a general basis, such a response is characterized by a second-order, low-pass-band filter behaviour with a damped resonance appearing near the cutoff frequency $\omega_{LED,3dB}$. For $|H_{LED}(\omega)|^2$, the expression for the peak frequency of the resonance $\omega_{P,LED}$ is given by:

$$\omega_{P,LED}^2 = \omega_{R,LED}^2 \left[1 - \frac{1}{2}\left(\frac{\gamma_{LED}}{\omega_{R,LED}}\right)^2\right], \tag{4.69}$$

and that of the cut-off frequency $\omega_{LED,3dB}$ by:

$$\omega_{3dB,LED}^2 = \omega_{P,LED}^2 + \sqrt{\omega_{P,LED}^4 + \omega_{R,LED}^4}. \tag{4.70}$$

In the present case, since $\gamma_{LED} > \omega_{R,LED}$, the two previous equations reduce to:

$$\omega_{P,LED} = 0, \tag{4.71}$$

and

$$\omega_{3dB,LED} = \omega_{R,LED} \approx 20.1 \text{ ns}^{-1}. \tag{4.72}$$

To evaluate the impact of the LED response on the intracavity pumping geometry, one should first consider the evolution of $|H(\omega)|^2$ at room temperature and at the optimum detuning δ_{opt} for different values of the input current J using Eqs. (4.59) and (4.61) (Figs. 4.8(a) and 4.8(b)). Hence it is seen that for the electrical pumping case (Eq. (4.59)) with current densities in the range 10 to 20 Acm^{-2}, the peak frequency ω_P lies in the range 6–12 GHz and the cutoff frequency ω_{3dB} is expected to be $\sim$ 19 GHz (Fig. 4.8(b)). Much larger values are predicted for the intracavity pumping geometry when using Eq. (4.61) ($\omega_{3dB} \gg 400$ GHz). However, in this regime the modulation transfer function of the device is limited by the frequency response of the pumping LED, which has a cutoff frequency given by Eq. (4.69). Finally, we have to point out that the above-mentioned values are upper bounds since they do not account for example, for possible electrical parasitic effects that could potentially affect the transmission line impedance.

4.6 Conclusions

In summary, we have theoretically investigated some relevant electrical features of realistic III-nitride polariton diodes. First a formalism relying on coupled semi-classical Boltzmann equations adapted for an electrically-driven exciton-polariton device was used to derive the evolution of the occupation number of the polariton ground state vs pump current density for two pumping geometries: namely the direct electrical and the intracavity optical pumping schemes. The corresponding condensation phase diagrams under electrical injection, i.e., plots of J_{thr} vs detuning and temperature, were also extracted. It led to the determination of the minimum threshold current density $J_{thr,min}$ as a function of lattice temperature for the two pumping schemes. $J_{thr,min}$ values of $\sim$ 5 Acm^{-2} and 6 Acm^{-2} at room temperature has been derived for the direct electrical and the intracavity optical pumping geometries, respectively, which are close to previous estimates. Then a simplified rate equation modeling treatment was introduced to derive both steady-state and high-speed current modulation solutions. This simplified analysis made it possible to show that the carrier population which, acts as a reservoir for the stimulated relaxation process, namely that of the excitons, gets clamped once it crosses the condensation threshold, which is a direct consequence of the similarities of the simplified rate equations with those describing conventional laser diodes. The analysis of the modulation transfer function, derived from the dynamical response of polariton LDs to a small modulation of the current above threshold, demonstrates the interesting potential of the direct electrical pumping scheme, since a cutoff frequency ω_{3dB} up to $\sim$ 19 GHz is predicted, whereas for the intracavity optical pumping scheme, the cutoff frequency is shown to be limited by the frequency response of the pumping LED, for which $\omega_{3dB} \approx 3.2$ GHz.

Chapter 5

Summary, conclusions and further work

The thesis is concerned with three general areas of study: (i) the negative refraction of certain dielectric and metallic photonic crystals, (ii) the optical properties of periodic dielectric structures with resonant inclusions such as semiconductor quantum wells, (iii) the kinetics of two types of microcavity-based polariton laser.

Negative refraction by photonic crystals is considered in Chapter 2. Negative refraction has been attracting considerable interest in recent years due to the possibility of using the effect to realize optical components such as superlenses and invisibility cloaks. Section 2.2 is concerned with negative refraction at the side-edge of a one-dimensional dielectric photonic crystal. It has been shown that the effect of negative refraction in this case is equivalent to -1 order diffraction and is very dependent on the angle of incidence and thus cannot be used to produce a practical superlens. However, a new effect - spatial oscillations of the Poynting vector of the refracted radiation - has been predicted analytically and observed in finite-difference time-domain numerical simulations.

Section 2.3 is dedicated to the modelling of a new type of spectral filter for terahertz radiation using a metallic photonic crystal prism. The filtering is based on the negative refraction of electromagnetic waves with frequencies lying in the second photonic band of the metallic photonic crystal. Thus, compared to a conventional prism, there is a large angular dispersion between the frequency components lying in the second photonic band and other frequencies. The optimal design of the prism was obtained using finite-difference time-domain simulations. Subsequently colleagues fabricated a prism, based on the proposed design, and their experimental measurements have shown that the proposed device can indeed act as an efficient spectral filter for the terahertz frequency range.

Chapter 3 reported studies of the optical properties of the dielectric photonic structures with resonant inclusions such as optical cavities adjacent to thin metal films or quantum wells the can support excitons. Section 3.2 describes theoretical calculations of the eigenmode structure of a metal layer sandwiched between two Bragg reflectors. It is shown that Tamm plasmon polariton states exist on both sides of the metal layer and are coupled via the evanescent waves inside the metal film. The coupling of the Tamm plasmon modes leads to eigenfrequency splitting and thus to distinctive features in the band structure of the system. Analytical formulae for the system eigefrequencies have been derived and are shown to agree well with numerical modelling and with measurements on the structures studied by collaborators.

Section 3.3 is concerned with the eigenmodes of a periodic array of quantum wells embedded in the layers of a dielectric Bragg mirror. Analytical expressions for the mode eigenfrequencies have been derived and used to explain the origin of the triplet structure seen in the experimental reflection spectra. Section 3.4 describes the modelling of the parametric amplification which has also been experimentally observed in the system. Modelling results, which have been obtained using a three-level formalism, are shown to agree well with the experimental results.

Chapter 4 concerns modelling of the kinetics of GaN-based polariton lasers. The modelling was performed using a semiclassical Boltzmann equation approach. It is shown that a threshold pump of the order of 50 Acm^{-2} can be reached at room temperature if the optimal detuning between the exciton and cavity mode is chosen. Studies of the small signal response of the polariton laser are also presented. It has been shown that the polariton laser operates as a low-pass-band filter with a cut-off frequency about 3 GHz. The relatively low threshold pump powers and high cut-off frequencies are very promising for the realization of new types of optoelectronic devices based on polariton lasers.

We now comment on the impact of the work presented in the thesis and possible future work on the structures considered. We believe that the work on negative refraction at the side-edge of one-dimensional photonic crystals has been taken as far as it is reasonable to do so, particularly since it has been shown recently that layered metal-dielectric nanostructures can exhibit all-angle negative refraction in a wide frequency range [108], making them a far more promising basis for the realization of superlenses and invisibility cloaks. However, the work on the terahertz spectral filter based on a metallic photonic crystal prism, while lacking opportunities for the further original theoretical investigations could play a significant role in modern terahertz technology, since effective spectral band pass filters for the terahertz range are not commonplace,

and the device proposed has the additional advantage that it could be deposited on a chip.

The impact of the work on Tamm states in metal-organic cavities is illustrated by the fact, that the subsequent work by our experimental collaborators dedicated to the same topic was published in Nature Photonics [109]. The authors produced a lateral patterning of the metal-organic microcavity, introducing a set of metallic stripes rather than a uniform metal film inside the cavity. Moreover, they have shown that the introduction of the metal inside the cavity does not significantly degrade the coherence properties of the optical cavity mode. Such structures could be used to organize exciton-polariton condensates in a periodic potential and to do so at room-temperature due to the large binding energy of the excitons in the organic systems.

We believe, the work on exciton-polaritons in photonic crystals with embedded quantum wells is important because it showed both theoretically and experimentally that it is possible to realize strong coupling between the photonic crystal modes and the excitons. The resulting exciton-polaritons exhibit strong nonlinear dynamics, such as the parametric amplification that is typical for the exciton-polaritons in conventional microcavities. However, photonic crystal modes provide larger flexibility of the dispersion properties of the exciton-polaritons. In particular, it has been predicted that for certain structures, exciton-polaritons with negative group velocity and effective mass could be observed. Such polaritons would have peculiar nonlinear dynamics since their ground state, defined by the zero in-plane wavevector, would at the same time have the largest energy. This property should also lead to an unusual characteristics of polariton-phonon and polariton-electron scattering.

With regard to further work, the theoretical formalism, such as the transfer matrix method and other theory used to describe the optical properties of periodic dielectric nanostructures presented in chapter 3, can also be applied to the case of the periodic layered structures containing metal layers. Consider a periodic layered metal-dielectric nanostructure comprising alternating metal and dielectric layers with dielectric permittivitties $\varepsilon_m, \varepsilon_d$ and thicknesses d_m, d_d, respectively. If the period of the structure is much less than the electromagnetic wavelength then the effective medium [110] approximation can be used and the structure treated as a uniaxial, anisotropic medium with components of dielectric permittivity tensor given by:

$$\varepsilon_{\parallel} = \frac{\varepsilon_m d_m + \varepsilon_d d_d}{d_d + d_m}; \quad \varepsilon_{\perp} = \left(\frac{d_d}{\varepsilon_d} + \frac{d_m}{\varepsilon_m} \right)^{-1}, \tag{5.1}$$

where the symbols $\parallel$ and $\perp$ correspond to the in-plane and axial components of the dielectric permittivity tensor respectively. It follows that the dispersion relation between

frequency ω and the wavevector components $k_{\parallel}, k_{\perp}$ is $\omega^2/c^2 = k_{\parallel}^2/\varepsilon_{\perp} + k_{\perp}^2/\varepsilon_{\parallel}$. It is clear that if the dielectric permittivity tensor components have different signs as occurs in this case due to the negative permittivity of the metal layers, the isofrequency contours obtained from the dispersion relations will have a hyperbolic shape, in contrast to the elliptical shape of conventional anisotropic media. The characteristic shape of the isofrequency contours of such hyperbolic media leads to the possibility of realizing a number of useful effects, including all-angle negative refraction [111], and superlensing [112]. However, one of the most intriguing properties of the hyperbolic media is the divergent density of states caused by the unbound isofrequency contours [113]. The divergent density of states directly leads to a great enhancement in the spontaneous emission rate (so called *Purcell factor*) for point-like emitters placed inside such media.

The decease of the spontaneous emission lifetime of sources placed inside hyperbolic media has been extensively studied both theoretically [114] and experimentally [115] in recent years. However, I propose to study the Forster resonant energy transfer (FRET) between two point emitters placed inside hyperbolic media. FRET is a non-radiative resonant process of energy transfer between two two-level systems, which can be considered to be carried out by virtual photons [116]. The efficiency of the FRET process can be calculated using second-order perturbation theory and is inversely proportional to the sixth power of the distance between the two systems, which makes it a powerful tool for precise measurement of the distance between the chromophores in the biological systems, for example. The picture is expected to change dramatically when the emitters are placed inside a hyperbolic medium due to the huge density of the photonic states [117]. Furthermore, I am also planning to study the optical properties of hyperbolic media when the components of the dielectric permittivity tensors are characterized by a nonlinear (Kerr) dielectric permittivity. In particular, it is planned to study the modification to the spontaneous emission lifetime of point sources placed inside such nonlinear hyperbolic media.

Finally, the formalism for modelling GaN-based polariton laser, described in the chapter 4 together with the associated software developed constitute a powerful tool for modelling the dynamics of polariton lasers in general. To enhance its performance, the software should be merged with a finite element simulation code, which would calculate the dispersion of the eigenfrequencies of device with realistic 3D geometries. Furthermore, this work could be extended to the case when a strong magnetic field of about 1 T is applied to the microcavity. A series of recent experiments have shown that the polariton lasing threshold can be significantly decreased by the application of magnetic field. The modelling could be undertaken in the similar way to that presented in chapter 4. The magnetic field would affect the dispersion of the low polaritonic branch (there

would actually be 4 separate polaritonic branches in this case) and the density of polaritonic states. Therefore the additional mechanism of spin-flipping resulting in the scattering of the polaritons between different branches would have to be considered in the modelling. Nevertheless, these effects can be accounted for by a relatively small changes to the modelling software.

References

[1] W.L. Bragg. The diffraction of short electromagnetic waves by a crystal. *Proceedings of the Cambridge Philosophical Society*, 17:43–57, 1913.

[2] J. W. S. Rayleigh. On the remarkable phenomenon of crystalline reflection described by Prof. Stokes. *Philosophical Magazine*, 26:256–265, 1888.

[3] E. Yablonovitch. Inhibited spontaneous emission in solid-state physics and electronics. *Phys. Rev. Lett.*, 58(20):2059–2062, 1987.

[4] S. John. Strong localization of photons in certain disordered dielectric superlattices. *Phys. Rev. Lett.*, 58(23):2486–2489, 1987.

[5] J. D. Joannopoulos, S. G. Johnson, J. N. Winn, and R. D. Meade. *Photonic crystals. Molding the flow of light.* Princeton University Press, 2008.

[6] G. Wannier. The structure of electronic excitation levels in insulating crystals. *Phys. Rev.*, 52:191, 1937.

[7] E.L. Ivchenko, A.I. Nesvizhskii, and S. Jorda. Bragg reflection of light from quantum-well structures. *Phys. Solid State*, 36:1156–1161, 1994.

[8] V.M. Agranovich and O.A. Dubovskii. Effect of retarded interaction on the exciton spectrum in one-dimensional and two-dimensional crystals. *JETP Letters*, 3:233, 1966.

[9] A. Imamoglu, R. J. Ram, S. Pau, and Y. Yamamoto. Nonequilibrium condensates and lasers without inversion: Exciton-polariton lasers. *Phys. Rev. A*, 53:4250, 1996.

[10] S. Kundermann, M. Saba, C. Ciuti, T. Guillet, U. Oesterle, J.L. Staehli, and B. Deveaud. Coherent control of polariton parametric scattering in semiconductor microcavities. *Phys. Rev. Lett.*, 91(10):107402, 2003.

[11] T. C. Liew, A. V. Kavokin, T. Ostatnicky, M. A. Kaliteevski, I. A. Shelykh, and R. A. Abram. Exciton-polariton integrated circuits. *Phys. Rev. B*, 82(3):033302, 2010.

[12] F. P. Laussy, A. V. Kavokin, and I. A. Shelykh. Exciton-polariton mediated superconductivity. *Phys. Rev. Lett.*, 104:106402, 2010.

[13] I.-H. Chen, Y. Y. Lin, Y.-C. Lai, E. S. Sedov, A. P. Alodjants, S. M. Arakelian, and R.-K. Lee. Solitons in cavity-qed arrays containing interacting qubits. *Phys. Rev. A*, 86:023829, 2012.

[14] I. V. Iorsh, M. A. Kaliteevski, S. Brand, R. A. Abram, and N. A. Kaliteevskaya. An 'electromagnetic wiggler' originating from refraction of waves at the side edge of a Bragg reflector. *Journal of Modern Optics*, 58:686–693, 2011. doi: 10.1080/09500340.2011.565887.

[15] G. P. Swift, A. J. Gallant, N. Kaliteevskaya, M. A. Kaliteevski, S. Brand, D. Dai, A. J. Baragwanath, I. Iorsh, R. A. Abram, and J. M. Chamberlain. Negative refraction and the spectral filtering of terahertz radiation by a photonic crystal prism. *Optics Letters*, 36:1641–1643, 2011.

[16] V. G. Veselago. Electrodynamics of media with simultaneously negative electric permittivity and magnetic permeability. *UFN*, 92(3):517–526, 1967.

[17] P. M. Valanju, R. M. Walser, and A. P. Valanju. Wave refraction in negative-index media: Always positive and very inhomogeneous. *Phys. Rev. Lett.*, 88: 187401, 2002.

[18] J. Pendry. Negative refraction. *Contemporary Physics*, 45(3):191, 2004.

[19] M.I. Stockman. Criterion for negative refraction with low optical losses from a fundamental principle of causality. *Phys. Rev. Lett.*, 98:177404, 2007.

[20] V. Shklover C. Hafner V. Veselago, L. Braginsky. Negative refraction index materials. *Journal of Computational and Theoretical Nanoscience*, 3:1–30, 2006.

[21] D. R. Smith and N. Kroll. Negative refractive index in left-handed materials. *Phys. Rev. Lett.*, 85:2933–2936, 2000.

[22] L.D. Landau and E.M. Lifshitz. *Electrodynamics of Continuous Media*. Pergamon, New York, 1974.

[23] R.A. Shelby, D.R. Smith, and S. Schultz. Experimental verification of a negative index of refraction. *Science*, 292(5514):77–79, 2001.

[24] D.R. Smith, S. Schultz, P. Markos, and C.M. Soukoulis. Determination of effective permittivity and permeability of metamaterials from reflection and transmission coefficients. *Phys. Rev. B*, 65(19), 2002.

[25] J. B. Pendry, A. J. Holden, W. J. Stewart, and I. Youngs. Extremely Low Frequency Plasmons in Metallic Mesostructures. *Phys. Rev. Lett.*, 76(25):4773–4776, 1996.

[26] D.F. Sievenpiper, M.E. Sickmiller, and E. Yablonovitch. 3D wire mesh photonic crystals. *Phys. Rev. Lett*, 76(14):2480–2483, 1996.

[27] P.V. Parimi, W.T. Lu, P. Vodo, J. Sokoloff, J.S. Derov, and S. Sridhar. Negative refraction and left-handed electromagnetism in microwave photonic crystals. *Phys. Rev. Lett*, 92(12):127401, 2004.

[28] P. Vodo, W. T. Lu, Y. Huang, and S. Sridhar. Negative refraction and plano-concave lens focusing in one-dimensional photonic crystals. *Appl. Phys. Lett.*, 89 (8):084104, 2006.

[29] D.O.S. Melville, R.J. Blaikie, and C.R. Wolf. Submicron imaging with a planar silver lens. *Appl. Phys. Lett.*, 84(22):4403–4405, 2004.

[30] J. B. Pendry. Negative refraction makes a perfect lens. *Phys. Rev. Lett.*, 85(18): 3966–3969, 2000.

[31] W. Cai, U.K. Chettiar, A.V. Kildishev, and V.M. Shalaev. Designs for optical cloaking with high-order transformations. *Opt. Express*, 16(8):5444–5452, 2008.

[32] M. Kaliteevski, S. Brand, R. A. Abram, A. J. Gallant, and J. M. Chamberlain. Negative refraction can make non-diffracting beams. *Opt. Express*, 16(19):14582–14587, 2008.

[33] C. Luo, S.G. Johnson, J.D. Joannopoulos, and J.B. Pendry. All-angle negative refraction without negative effective index. *Phys. Rev. B*, 65(20):201104, 2002.

[34] J. E. Lugo, B. de la Mora, R. Doti, R. Nava, J. Tague na, A. del Rio, and J. Faubert. Multiband negative refraction in one-dimensional photonic crystals. *Opt. Express*, 17(5):3036–3041, 2009.

[35] A.V. Kavokin, G. Malpuech, and I.A. Shelykh. Negative refraction of light in Bragg mirrors made of porous silicon. *Physics Letters A*, 339(3-5):387–392, 2005.

[36] I.C. Botten, M.S. Craig, L.V. Adams, and J.R. Andrewarth. The dielectric lamillar diffraction grating. *Journal of Modern Optics*, 28(3):413–428, 1981.

[37] M.A. Kaliteevski, D.M. Beggs, S. Brand, R.A. Abram, and V.V. Nikolaev. Stability of the photonic band gap in the presence of disorder. *Phys. Rev. B*, 73(3): 033106, 2006.

[38] A. Kavokin, G. Malpuech, A. Di Carlo, P. Lugli, and F. Rossi. Photonic Bloch oscillations in laterally confined Bragg mirrors. *Phys. Rev. B*, 61:4413–4416, 2000.

[39] J.M. Chamberlain. Where optics meets electronics: recent progress in decreasing the terahertz gap. *Philosophical Transactions of the Royal Society A.P*, 362:1815, 2004.

[40] J. B. Jackson, M. Mourou, J. F. Whitaker, I. N. Duling, S. L. Williamson, M. Menu, and G. A. Mourou. Terahertz imaging for non-destructive evaluation of mural paintings. *Optics Letters*, 281:527–532, 2008.

[41] E. Pickwell and V. P. Wallace. Biomedical applications of terahertz technology. *Journal of Physics D*, 39:301, 2006.

[42] S. Brand, R. A. Abram, and M. A. Kaliteevski. Complex photonic band structure and effective plasma frequency of a two-dimensional array of metal rods. *Phys. Rev. B*, 75(3):035102, 2007.

[43] A. J. Gallant, M. A. Kaliteevski, S. Brand, D. Wood, M. Petty, R. A. Abram, and J. M. Chamberlain. Terahertz frequency bandpass filters. *Journal of Applied Physics*, 102(2):023102, 2007.

[44] T. Matsui, A. Agrawal, A. Nahata, and Z.V. Vardeny. Transmission resonances through aperiodic arrays of subwavelength apertures. *Nature*, 446:517–521, 2007.

[45] B. Voisiat, A. Biinas, I. Kaalynas, and G. Raiukaitis. Band-pass filters for thz spectral range fabricated by laser ablation. *Applied Physics A*, 104:953–958, 2011.

[46] R. Brückner, M. Sudzius, S. I. Hintschich, H. Fröb, V. G. Lyssenko, M. A. Kaliteevski, I. Iorsh, R. A. Abram, A. V. Kavokin, and K. Leo. Parabolic polarization splitting of Tamm states in a metal-organic microcavity. *Appl. Phys. Lett.*, 100 (6):062101, 2012.

[47] A. Askitopoulos, L. Mouchliadis, I. Iorsh, G. Christmann, J. J. Baumberg, M. A. Kaliteevski, Z. Hatzopoulos, and P. G. Savvidis. Bragg polaritons: Strong coupling and amplification in an unfolded microcavity. *Phys. Rev. Lett.*, 106:076401, 2011.

[48] I. A. Shelykh, R. Johne, D. D. Solnyshkov, A. V. Kavokin, N. A. Gippius, and G. Malpuech. Quantum kinetic equations for interacting bosons and their application for polariton parametric oscillators. *Phys. Rev. B*, 76:155308, 2007.

[49] P. Yeh, A. Yariv, and A. Cho. Optical surface waves in periodic layered media. *Appl. Phys. Lett.*, 32(2):104–105, 1978.

[50] A. Yariv and P. Yeh. *Optical waves in crystals: propagation and control of laser radiation*. Wiley, New York, 2002.

[51] T. C. H. Liew, A. V. Kavokin, T. Ostatnický, M. Kaliteevski, I. A. Shelykh, and R. A. Abram. Exciton-polariton integrated circuits. *Phys. Rev. B*, 82:033302, 2010.

[52] O. Gazzano, S. Michaelis de Vasconcellos, K. Gauthron, C. Symonds, J. Bloch, P. Voisin, J. Bellessa, A. Lematre, and P. Senellart. Evidence for confined Tamm plasmon modes under metallic microdisks and application to the control of spontaneous optical emission. *Phys. Rev. Lett.*, 107:247402, 2011.

[53] P. B. Johnson and R. W. Christy. Optical constants of the noble metals. *Phys. Rev. B*, 6(12):4370–4379, 1972.

[54] E.L. Ivchenko, M.M Voronov, M.V. Erementchouk, L.I. Deych, and Lisyansky A.A. Multiple-quantum-well-based photonic crystals with simple and compound elementary supercells. *Phys. Rev. B*, 70(19):195106, 2004.

[55] A.Y. Sivachenko, M.E. Raikh, and Z.V. Vardeny. Excitations in photonic crystals infiltrated with polarizable media. *Phys. Rev. A.*, 64(1):138091–138098, 2001.

[56] C. Ciuti, P. Schwendimann, and A. Quattropani. Parametric luminescence of microcavity polaritons. *Phys. Rev. B*, 63:041303, 2001.

[57] R. M. Stevenson, V. N. Astratov, M. S. Skolnick, D. M. Whittaker, M. Emam-Ismail, A. I. Tartakovskii, P. G. Savvidis, J. J. Baumberg, and J. S. Roberts. Continuous wave observation of massive polariton redistribution by stimulated scattering in semiconductor microcavities. *Phys. Rev. Lett.*, 85:3680–3683, 2000.

[58] P.G. Savvidis, J.J. Baumberg, R.M. Stevenson, M.S. Skolnick, D.M. Whittaker, and J.S. Roberts. Angle-resonant stimulated polariton amplifier. *Phys. Rev. Lett*, 84(7):1547–1550, 2000.

[59] J. J. Hopfield and D. G. Thomas. Theoretical and experimental effects of spatial dispersion on the optical properties of crystals. *Phys. Rev.*, 132(2):563–572, Oct 1963. doi: 10.1103/PhysRev.132.563.

[60] Y. Yamamoto, F. Tassone, and H. Cao. *Semiconductor Cavity Quantum Electrodynamics*. Springer, New York, 2000.

[61] Y. Narukawa, Y. Kawakami, S. Fujita, and S. Nakamura. Dimensionality of excitons in laser-diode structures composed of $in_xga_{1-x}N$ multiple quantum wells. *Phys. Rev. B*, 59:10283–10288, 1999.

[62] I. Iorsh, M. Glauser, G. Rossbach, J. Levrat, M. Cobet, R. Butté, N. Grandjean, M. A. Kaliteevski, R. A. Abram, and A. V. Kavokin. Generic picture of the emission properties of III-nitride polariton laser diodes: Steady state and current modulation response. *Phys. Rev. B*, 86:125308, 2012.

[63] J. Kasprzak, M. Richard, S. Kundermann, A. Baas, P. Jeambrun, J. M. J. Keeling, F. M. Marchetti, R. André M. H. Szymańska, J. L. Staehli, V. Savona, P. B. Littlewood, B. Deveaud, and Le Si Dang. Bose Einstein condensation of exciton polaritons. *Nature (London)*, 443:409, 2006.

[64] S. Christopoulos, G. Baldassarri Höger von Högersthal, A. J. D. Grundy, P. G. Lagoudakis, A. V. Kavokin, J. J. Baumberg, G. Christmann, R. Butté, E. Feltin, J.-F. Carlin, and N. Grandjean. Room-temperature polariton lasing in semiconductor microcavities. *Phys. Rev. Lett.*, 98:126405, 2007.

[65] G. Christmann, R. Butté, E. Feltin, J.-F. Carlin, and N. Grandjean. Room temperature polariton lasing in a GaN/AlGaN multiple quantum well microcavity. *Appl. Phys. Lett.*, 93:051102, 2008.

[66] S. Kéna-Cohen and S. R. Forrest. Room-temperature polariton lasing in an organic single-crystal microcavity. *Nature Phot.*, 4:371, 2010.

[67] K. G. Lagoudakis, M. Wouters, M. Richard, A. Baas, I. Carusotto, R. André, L. S. Dang, and B. Deveaud-Plédran. Quantized vortices in an exciton polariton condensate. *Nature Physics*, 4:706, 2008.

[68] A. V. Kavokin Y. G. Rubo R. André K. G. Lagoudakis, T. Ostatnický and B. Deveaud-Plédran. Observation of half-quantum vortices in an exciton-polariton condensate. *Science*, 326:974, 2009.

[69] A. Amo, D. Sanvitto, F. P. Laussy, D. Ballarini, E. del Valle, M. D. Martin, A. Lemaître, J. Bloch, D. N. Krizhanovskii, M. S. Skolnick, C. Tejedor, and L. Vi na. Collective fluid dynamics of a polariton condensate in a semiconductor microcavity. *Nature (London)*, 457:291, 2009.

[70] A. Amo, J. Lefrère, S. Pigeon, C. Adrados, C. Ciuti, I. Carusotto, R. Houdré, E. Giacobino, and A. Bramati. Superfluidity of polaritons in semiconductor microcavities. *Nature Physics*, 5:805, 2009.

[71] K.G. Lagoudakis, B. Pietka, M. Wouters, R. André, and B. Deveaud-Plédran. Coherent oscillations in an exciton-polariton Josephson junction. *Phys .Rev. Lett.*, 105:120403, 2010.

[72] A.A. Khalifa, A.P.D. Love, D.N. Krizhanovskii, M.S. Skolnick, and J.S. Roberts. Electroluminescence emission from polariton states in GaAs-based semiconductor microcavities. *Appl. Phys. Lett*, 92:061107, 2008.

[73] H. Mathieu, P. Lefebre, and P. Christol. Simple analytical method for calculating exciton binding energies in semiconductor quantum wells. *Phys. Rev. B*, 46:4092, 1992.

[74] J. Bloch V. Thierry-Mieg R. André Le Si Dang S. Kundermann A. Mura G. Bongiovanni J. L. Staehli M. Saba, C. Ciuti and B. Deveaud. High-temperature ultrafast polariton parametric amplification in semiconductor microcavities. *Nature (London)*, 414:731, 2001.

[75] R. Butté and N. Grandjean. A novel class of coherent light emitters: polariton lasers. *Semicond. Sci. Technol.*, 26:014030, 2011.

[76] D. Solnyshkov, E. Petrolati, A. Di Carlo, and G. Malpuech. Theory of an electrically injected bulk polariton laser. *Appl. Phys. Lett.*, 94:011110, 2009.

[77] G. Christmann, R. Butté, E. Feltin, A. Mouti, P. A. Stadelmann, A. Castiglia, J.-F. Carlin, and N. Grandjean. Large vacuum Rabi splitting in a multiple quantum well GaN-based microcavity in the strong-coupling regime. *Phys. Rev. B*, 77: 085310, 2008.

[78] G. Christmann, R. Butté, E. Feltin, J.-F. Carlin, and N. Grandjean. Impact of inhomogeneous excitonic broadening on the strong exciton-photon coupling in quantum well nitride microcavities. *Phys. Rev. B*, 73:153305, 2006.

[79] R. Butté, J. Levrat, G. Christmann, E. Feltin, J.-F. Carlin, and N. Grandjean. Phase diagram of a polariton laser from cryogenic to room temperature. *Phys. Rev. B*, 80:233301, 2009.

[80] M. Suzuki, J. Nishio, M. Onomura, and C. Hongo. GaN polariton LEDs. *J. Cryst. Growth*, 189/190:511, 1998.

[81] G. Cosendey, J.-F. Carlin, N.I.K Kaufmann, R. Butté, and N. Grandjean. Strain compensation in AlInN/GaN multilayers on GaN substrates: Application to the realization of defect-free Bragg reflectors. *Appl. Phys. Lett.*, 98(18):181111, 2011.

[82] G. Christmann, D. Simeonov, R. Butté, E. Feltin, J.-F. Carlin, and N. Grandjean. Impact of disorder on high quality factor III − V nitride microcavities. *Appl. Phys. Lett.*, 89(26):261101, 2006.

[83] A. David, M.J. Grundmann, J.F. Kaeding, N.F. Gardner, T.G. Mihopoulos, and M.R. Krames. Carrier distribution in (0001)InGaN/GaN multiple quantum well light-emitting diodes. *Appl. Phys. Lett.*, 92(5):053502, 2008.

[84] G. Malpuech, D. Solnyshkov, A. Di Carlo, and E. Petrolati. patent pending 2.938.384, bulletin officiel de la propriété industrielle. *Institut National de la Propriété Industrielle*, 10/19:132, 2010.

[85] R. Butté, G. Christmann, E. Feltin, A. Castiglia, J. Levrat, G. Cosendey, A. Altoukhov, J.-F. Carlin, and N. Grandjean. Room temperature polariton lasing in III-nitride microcavities: a comparison with blue GaN-based vertical cavity surface emitting lasers. *Proc. SPIE*, 7216:721619, 2009.

[86] A. Castiglia, D. Simeonov, H. J. Buehlmann, J.-F. Carlin, E. Feltin, J. Dorsaz, R. Butté, and N. Grandjean. Efficient current injection scheme for nitride vertical cavity surface emitting lasers. *Appl. Phys. Lett.*, 90(3):033514, 2007.

[87] T.-C. Lu, C.-C. Kao, H.-C. Kuo, G.-H. Huang, and S.-C. Wang. Cw lasing of current injection blue GaN-based vertical cavity surface emitting laser. *Appl. Phys. Lett.*, 92(14):141102, 2008.

[88] S. Nakamura, G. Fasol, and S. J. Pearton. *The Blue Laser Diode: The Complete Story.* Springer, Berlin, 2000.

[89] V. Savona, L. C. Andreani, P. Schwendimann, and A. Quattropani. Quantum well excitons in semiconductor microcavities: Unified treatment of weak and strong coupling regimes. *Solid State Comm.*, 93:733, 1995.

[90] H. A. McLeod. *Thin-Film Optical Filters, 2^{nd} ed.* Adam Hilger, Bristol, U.K., 1996.

[91] D. Brunner, H. Angerer, E. Bustarret, F. Freudenberg, R. Höpler, R. Dimitrov, O. Ambacher, and M. Stutzmann. Optical constants of epitaxial AlGaN films and their temperature dependence. *J. Appl. Phys*, 82:5090, 97.

[92] J.-F. Carlin and M. Ilegems. High-quality AlInN for high index contrast Bragg mirrors lattice matched to GaN. *Appl. Phys. Lett.*, 83(4):668–670, 2003.

[93] J.-F. Carlin, C. Zellweger, J. Dorsaz, S. Nicolay, G. Christmann, E. Feltin, R. Butt, and N. Grandjean. Progresses in III-nitride distributed Bragg reflectors and microcavities using AlInN/GaN materials. *physica status solidi B*, 242(11):2326–2344, 2005.

[94] M. J. Bergmann and H. C. Casey. Optical-field calculations for lossy multiple-layer $Al_xGa_{1x}N/In_xGa_{1x}N$ laser diodes. *Journal of Applied Physics*, 84:1196, 1998.

[95] R. Schmidt, B. Rheinländer, M. Schubert, D. Spemann, T. Butz, J. Lenzner, E. M. Kaidashev, M. Lorenz, A. Rahm, H. C. Semmelhack, and M. Grundmann. Dielectric functions (1 to 5 ev) of wurtzite $Mg_xZn_{1-x}O(x < 0.29)$ thin films. *Appl. Phys. Lett.*, 82(14):2260–2262, 2003.

[96] F. Tassone and Y. Yamamoto. Exciton-exciton scattering dynamics in a semiconductor microcavity and stimulated scattering into polaritons. *Phys. Rev. B*, 59: 10830–10842, 1999.

[97] A. Kavokin, J.J. Baumberg, G. Malpuech, and F.P. Laussy. *Microcavities*. Clarendon Press, Oxford, 2006.

[98] L. E. Golub, A. V. Scherbakov, and A. V. Akimov. Energy distributions of 2D excitons in the presence of nonequilibrium phonons. *J. Phys. : Condensed Matter*, 8:2163, 1996.

[99] J. Levrat, R. Butté, G. Christmann, E. Feltin, J.-F. Carlin, and N. Grandjean. Tailoring the strong coupling regime in III-nitride based microcavities for room temperature polariton laser applications. *Phys. Status Solidi (c)*, 6:2820, 2009.

[100] J. Levrat, R. Butté, E. Feltin, J.-F. Carlin, N. Grandjean, D. Solnyshkov, and G. Malpuech. Condensation phase diagram of cavity polaritons in GaN-based microcavities: Experiment and theory. *Phys. Rev. B*, 81:125305, 2010.

[101] G. Malpuech, A. Kavokin, A. Di Carlo, and J. J. Baumberg. Polariton lasing by exciton-electron scattering in semiconductor microcavities. *Phys. Rev. B*, 65: 153310, 2002.

[102] G. Ramon, A. Mann, and E. Cohen. Theory of neutral and charged exciton scattering with electrons in semiconductor quantum wells. *Phys. Rev. B*, 67:045323, 2003.

[103] W. G. Scheibenzuber, U. T. Schwarz, L. Sulmoni, J. Dorsaz, J.-F. Carlin, and N. Grandjean. Recombination coefficients of GaN-based laser diodes. *Journal of Applied Physics*, 109(9):093106, 2011.

[104] M. Suzuki, T. Uenoyama, and A. Yanase. First-principles calculations of effective-mass parameters of AlN and GaN. *Phys. Rev. B*, 52:8132–8139, 1995.

[105] R. Truell, C. Elbaum, and B. B. Chick. *Ultrasonic Methods in Solid State Physics*. Academic Press, New York, 1969.

[106] J. Kasprzak, D. D. Solnyshkov, R. André, Le Si Dang, and G. Malpuech. Formation of an exciton polariton condensate: Thermodynamic versus kinetic regimes. *Phys. Rev. Lett.*, 101:146404, 2008.

[107] L. A. Coldren and S. W. Corzine. *Diode Lasers and Photonic Integrated Circuits.* Wiley, New York, 1995.

[108] X. Fan, G.P. Wang, J.C.W. Lee, and C. T. Chan. All-angle broadband negative refraction of metal waveguide arrays in the visible range: Theoretical analysis and numerical demonstration. *Phys. Rev. Lett.*, 97:073901, 2006.

[109] R. Scholz M. Sudzius S. I. Hintschich H. Frob V. G. Lyssenko R. Bruckner, A. A. Zakhidov and K. Leo. Phase-locked coherent modes in a patterned metalorganic microcavity. *Nature Phot.*, 6:322, 2012.

[110] V. M. Agranovich and V. E. Kravtsov. Notes on crystal optics of superlattices. *Solid State Communications*, 55(1):85, 1985.

[111] D. R. Smith, P. Kolinko, and D. Schurig. Negative refraction in indefinite media. *J. Opt. Soc. Am. B*, 21(5):1032–1043, 2004.

[112] Z. Jacob, L.V. Alekseyev, and E. Narimanov. Optical hyperlens: Far-field imaging beyond the diffraction limit. *Opt. Express*, 14(18):8247–8256, 2006.

[113] Z. Jacob, I. Smolyaninov, and E. Narimanov. Broadband Purcell effect: Radiative decay engineering with metamaterials. *ArXiv e-prints*, page 0910.3981, October 2009.

[114] A. N. Poddubny, P. A. Belov, P. Ginzburg, A. V. Zayats, and Y. S. Kivshar. Microscopic model of Purcell enhancement in hyperbolic metamaterials. *Phys. Rev. B*, 86:035148, 2012.

[115] M. A. Noginov, H. Li, Yu. A. Barnakov, D. Dryden, G. Nataraj, G. Zhu, C. E. Bonner, M. Mayy, Z. Jacob, and E. E. Narimanov. Controlling spontaneous emission with metamaterials. *Opt. Letters*, 35(11):1863–1865, 2010.

[116] Volkhard Helms. *Principles of Computational Cell Biology.* Weinheim: Wiley-VCH, 2008.

[117] C. L. Cortes, W. Newman, S. Molesky, and Z. Jacob. Quantum nanophotonics using hyperbolic metamaterials. *Journal of Optics*, 14:063001, 2012.